Muon Ionisation Cooling Experiment

The design and implementation of the Geometry Handling System and characterising of the EMR's scintillating bars.

Matthew Dean Littlefield

Centre for Sensors
and Instrumentation
Brunel University

A thesis submitted for the degree of
Doctor of Philosophy

Wednesday 25th January, 2017

For my parents

Acknowledgements

Standing on the shoulders of giants.

This has been the biggest feat I have ever faced, it has challenged my intellectual capacity as well as my ability to organise and drive a large project. I would not have gotten to this point without the help of some giants upon whose shoulders I have stood. I would like to deeply thank the following people who have supported me throughout my thesis.

Malcolm Ellis, although you were not there for my entire PhD you have always given me support, even from another hemisphere, and without you I would not have understood some basic principles of physics.

Chris Rogers, you have been a great support to me throughout the implementation of the geometry software and were patient when I asked (and I asked many) trivial questions about programming. Your support enabled me to complete that system which I hope is helping with MAUS.

Ruslan Asfandiyarov, working with you on the EMR has been thrilling. I have not had much experience, before my PhD, of particle detectors particularly in building them! Your help throughout this stage of my work was fantastic and I'm pleased to have helped with the project.

Brunel HEP group, particularly David Smith, Jo Cole, Peter Hobson and Ivan Reid for being there for me to talk through

ideas and ask silly questions too. Although Brunel has a small HEP group I think it comprises of a great bunch of people of which I was proud to be apart of.

My friends at the university for making my time there a pleasurable one.

Everyone at MICE for making my time there educational and fun. The time I spent on the experiment has shaped my life and I will always look back upon my time there with fondness.

Finally and most importantly, I'd like to personally thank Paul Kyberd. You have been an ever present support to me throughout my PhD and a great friend. Whether talking physics or rugby you have always helped me greatly throughout.

To all of you, your support and friendship has been deeply valued. Thank you.

Abstract

This thesis describes the Muon Ionisation Cooling Experiment (MICE), an engineering demonstration of the technique of ionisation cooling. It provides a detailed description of the creation of a Geometry Handling System that has been written as part of the MICE Analysis User Software and its benefits in providing a flexible and accurate method to model the MICE experiment. Finally the results of the bench tests of the Electron Muon Ranger will be presented.

MICE is part of an international programme to provide the technology for the Neutrino Factory (NF). The NF requires the technology to; capture the muons from a pion beam; cool them to form a high intensity beam with a small emittance; and accelerate the resulting muons. The decay of the resulting monochromatic muon beam produces a neutrino beam with precisely defined flavour content and an accurately calculable energy spectrum. The μ beam's intensity and collimation is sufficiently high to allow experiments to be performed with a baseline of several thousand km.

Contents

List of Figures

Chapter 1

The Small Neutral Ones

1.1 Introduction

"Nature uses only the longest threads to weave her patterns, so that each small piece of her fabric reveals the organization of the entire tapestry"

Richard P. Feynman

Physics has always proved to be an exciting subject with many unknowns. Once a measurement is made and results obtained in answer to initial questions, more are raised. As more is discovered the extent of our remaining ignorance becomes clearer. Ever since the initial discovery of the *small, neutral one* [1, 2] or 'neutrino', experiments to study this fascinating and elusive particle have always raised more questions. Neutrinos are mysterious and have always challenged the boundaries of physics and the understanding of the standard model of particle physics. They are the "lightest" of all the known matter particles and were once thought to be massless.

Charged current neutrino interactions always occur in conjunction with a charged lepton. The lepton type that is involved with the interaction is used to label the 'flavour' of that neutrino. The three neutrino flavours are ν_e; ν_μ; ν_τ. To illustrate this one can consider β decay, the decay produces an electron and an anti-electron-neutrino, $\overline{\nu_e}$. Initially it was believed that neutrinos conserved flavour whereby a beam of neutrinos with a particular

flavour would only produce that associated lepton when detected. Neutrino-matter interactions can be described, using quantum mechanics, in terms of the neutrinos flavour 'eigenstates', however whilst a neutrino traverses space the appropriate description is in terms of its mass. For leptons the flavour and mass eigenstates are identical; an electron flavoured lepton has a mass of 511 keV/c^2. This is not the case for neutrinos, each neutrino flavour is a mixture of the three different masses. Neutrinos moving through free space are described in terms of their masses, m_1, m_2, m_3. The three masses are mixed with certain percentages in order to give each of the flavour states. For example, the electron neutrino could be 50% m_1, 40% m_2 and 10% m_3 and it is this superposition of masses that makes the electron flavour state. The reverse is also true in that each mass state is a mixture of the flavour states. If we suppose each mass to be zero, as initially thought, it is expected that an electron neutrino would produce an electron when observed at any point during its life. This is not the case; experimental results have shown that neutrinos oscillate between flavours [3]. This oscillation implies that the three masses are not equal to one another. An explanation of this purely quantum mechanical phenomena can be achieved by considering the particles DeBroglie wavelength. This wavelength is a function of the particle momentum. The particle's three states travel with the same velocity but have different masses giving different momenta, therefore the wavelengths are different. As a neutrino propagates the percentage of each mass state varies because of the different wavelengths. The flavour of the observed neutrino is determined by the dominant mass upon observation. A neutrino-matter interaction will observe the neutrino's flavour, the probability of which flavour is observed depends on the relative contribution of the masses at that point.

Figure 1.1 illustrates the mixture of the three flavours of neutrino with respect to each of the mass eigenstates. Highlighted in this Figure is a phenomenon that has yet to be fully understood, the hierarchy of the mass states. Determining this hierarchy will be the aim of future neutrino experiments along with placing values upon parameters that characterise the mass-flavour relationship.

The probability of a neutrino of one flavour appearing as another can be

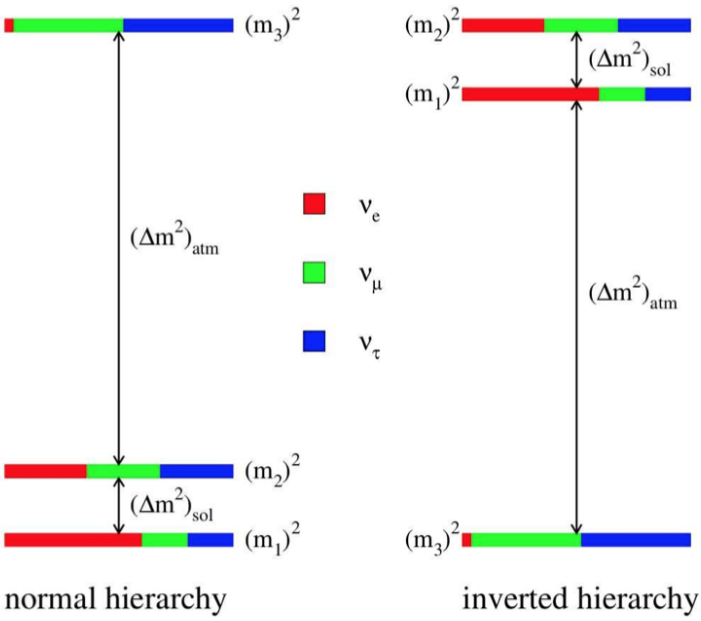

Figure 1.1: Illustration of the two proposed neutrino mass hierarchies. Colours indicate each neutrino flavour; electron in red, muon in green and tau in blue [4].

parameterised by a mixing angle. The new measurement has implications on proposed experiments that aim to measure other properties of the neutrino family. Understanding these particles fully will help to better explain the asymmetry of matter and anti-matter in the early stages of the universe and may shed light on other phenomena. A number of experiments have been proposed that will improve our knowledge of the neutrino, in particular mapping mass-flavour mixing and determining the mass hierarchy. Each has its own advantages and disadvantages and all of the proposals face huge technical challenges. The measurement of θ_{13} by Daya Bay [5] will undoubtedly influence the course of future studies but it also represents the progress being made in understanding the neutrino. The Daya Bay [6] experiment has made a precise measurement of one of these angles.

1.2 Neutrino History

In 1930 Wolfgang Pauli wrote a letter to a private meeting of experts on radioactivity held in Tübingen that proposed a neutral particle is emitted during nuclear beta decay that would account for the process's apparent violation of energy conservation. This was not publically presented until the Solvay congress of 1933. This neutral particle was called the neutron by Pauli and later named the 'neutrino' by Enrico Fermi when he postulated a theory where by an electron and a neutrino are both emitted during the decay process [1, 2]. Neutrinos rarely interact with matter and can travel many light years through matter before an interaction does take place. This is why direct observation of the neutrino did not happen until many years later.

In 1953 Clyde Cowen and Fred Reines began work on trying to detect the neutrino. They sought to do this by placing a detector near to a nuclear reactor in order to detect the neutrinos[1] being produced. This study was performed at Hanford but it only tentatively identified the neutrino because of limited statistics and high levels of background [7]. Three years later the duo designed a new detector and began work once again to confirm the neutrino's existence [8]. This new detector was placed at the Savannah River Plant facility of the U.S. Atomic Energy Commission. This was much more successful. The Hanford experiment had seen high levels of background that lead to the decision to place this new detector underground protecting it from cosmic rays. Cowen and Reines also placed this detector closer to the reactor than in the Hanford experiment, and improved the design of the detector. The new detector consisted of a 200 litre water tank with 40 kg of Cadmium Chloride dissolved in it, this was split between two tanks. The tanks were sandwiched between scintillators read out by photomultipliers. The location of the detector, which was both closer to the nuclear reactor and protected from cosmic rays, improved the signal to ratio background. These alterations lead to the confirmation of a neutrino flux via the inverse beta decay process

[1]They actually observed what are referred to as anti-neutrinos, but this is naming convention.

[8].

$$\bar{\nu} + p^{+} \rightarrow \beta^{+} + n^{0} \tag{1.1}$$

1962 saw the detection of a second neutrino type, the muon neutrino. The Stanford Linear Accelerator observed, in the mid 1970's, the tau lepton and it was hypothesized that the new lepton also had a neutrino much like its electron and muon siblings [9, 10, 11]. The tau neutrino was finally directly observed by the DONUT collaboration in 2000 [12].

1.3 Neutrino Oscillation

Many properties of the neutrino are purely quantum mechanical but can be explained through the use of partial analogies. These analogies compare the properties of neutrinos and will allow a classical rather than quantum mechanical understanding of their behaviours. To begin one must consider the facts that have been observed in the study of neutrinos. Firstly, a neutrino can be produced in association with a charged lepton or anti-lepton. The absorption of a neutrino during an interaction will result in the production of a charged lepton. The flavour of the outgoing lepton is then attributed to the flavour of the incoming neutrino. The lepton types of neutrino are referred to as the three flavours of neutrino. Observations show that a particle produced in association with an electron will be absorbed with an electron. From this one can infer that there is a conservation law associated with the production and absorption of neutrinos. If we consider a counter whereby 1 is added for every electron and electron neutrino, ν_e, and 1 is taken from the counter for every anti electron and anti-electron neutrino, then the counter for the universe will never alter. This explains why there must be a neutrino to accompany the electron produced in Beta Decay. Secondly the neutrinos with an electron flavour produced in the sun transform into muon neutrinos on their journey, although over 20 years of neutrino research was needed to firmly establish the truth of this transformation phenomenon [13].

The sun's nuclear processes are well understood; ν_e are produced as a result of these processes. Early detectors were designed to look for electron

neutrinos only. This was due to the expected flux of neutrinos from the sun which can be calculated using the standard solar model, see "How many sigmas is the solar neutrino effect" [14]. However, the measured ν_e flux on the surface of the Earth was less than the calculated total flux. This discrepancy produced two decades of debate that cast doubt upon the accuracy of the measurements. The low event rates, the difficulty to control background sources and the unfamiliar, to physicists, chemical techniques contributed to the doubt. The complex nature of the standard solar model where the initial assumptions affect the details of the calculations also increased the challenge of explaining the discrepancy. Early detectors were especially sensitive to these assumptions. This was the basis of the argument to dismiss this early discrepancy, however these arguments could not be held true after observations made by Kamiokande [15].

Kamiokande was measuring the natural flux of "atmospheric" neutrinos. Hadronic showers caused by incident cosmic rays upon the Earth's atmosphere are comprised mainly of pions. The pions will rapidly decay to produce muons of both flavours $\pi^+ \to \mu^+ + \nu_\mu$ and $\pi^- \to \mu^- + \bar{\nu_\mu}$. The muons with low energy will decay before reaching the ground producing neutrinos, $\mu^+ \to e^+ + \bar{\nu_\mu} + \nu_e$ and $\mu^- \to e^- + \nu_\mu + \bar{\nu_e}$. The processes of the hadronic shower are well known and understood, there are no other large sources of atmospheric neutrinos. According to the model there should be twice as many muon neutrinos as electron neutrinos. The total flux is difficult to calculate but the ratio of muon to electron neutrinos is easy to calculate and is difficult to vary. Energies of a few GeV will mean that some muons will reach the ground before decaying due to relativistic time dilation. This will increase the muon to electron ratio. Once again, this effect is well understood and easily calculated, meaning the muon to electron neutrino ratio from cosmic rays is well defined. The ratio that was measured by Kamiokande was far away from what was predicted. A totally unexpected dependence on the zenith angle of the neutrino was found. Even if the collaboration had made a mistake in the calculation of their sensitivity to the different neutrino flavours it was difficult to conceive an azimuthal dependence on its value. Kamiokande's observation of cosmic neutrinos yielded the same ν_e and ν_μ discrepancy [16].

The quantum mechanical nature of neutrinos means that it can be resolved into 3 components upon orthogonal axes within an abstract of space. The components can be described, to a degree, by an analogy with polarised light. If we consider a beam of light, this beam can be broken down into components along two orthogonal axes. The axes are arbitrary and have no bearing upon the light and don't have meaning unless the angle between them and the beam is known. If the orthogonal axes, x and y, are selected to lie along the planes of polarisation the beam's polarisation components can be described in relation to x and y with the angle θ between the beam and the axes. This is comparable to a neutrino except the neutrino has three components.

When a neutrino is created it will have a flavour eigenstate where the component along one flavour axis will equal 1 and along the others will be 0. The eigenstate is made of three axes; ν_e, ν_μ and ν_τ. This can be compared to producing light with a state of single polarisation, related to the production mechanism. The axes can be arbitrary and measurement can be taken along that axis or along an axis that is at right angles to the neutrino flavour eigenstate. The polarisation of light uses a 2D system which differs from a neutrino's where this is 3D. There are two ways to set our "resolving apparatus" for neutrinos. They can be detected through interactions, that is the axis set in the same way as production or they can be allowed to propagate through free space. Propagation chooses the mass eigenstates. Thus while interacting neutrinos have no well defined mass, whilst propagating they will have no defined flavour.

In the interest of the analogy with light we will only consider two components from the neutrino. Two different axes of polarised light can be related to one another if the angle of the beam of light and one of the axes is known. Consider two axes x_1, y_1 and x_2, y_2 that have an angle between them θ, their components can be related through the following:

$$x_2 = x_1 cos(\theta) + y_1 sin(\theta) \qquad y_2 = -x_1 sin(\theta) + y_1 cos(\theta) \tag{1.2}$$

Similarly a comparison can then be made between the neutrino mass and

flavour eigenstates. Where the expressions for the mas eigenstates are parameterised in terms of a single angle θ_{12} so that:

$$\nu_1 = \nu_e cos(\theta_{12}) + \nu_\mu sin(\theta_{12}) \qquad \nu_2 = -\nu_e sin(\theta_{12}) + \nu_\mu cos(\theta_{12}) \quad (1.3)$$

The vector or intensity of the light is not affected by the position of the axis and can be determined by the sum of the squares of it's components. The probability of finding a neutrino can be determined by the analogous sums of these components. The probability must sum to 1, $\alpha^2 + \beta^2 = 1$ and the mixing can be parameterised by the angle θ where $\alpha = cos\theta$ and $\beta = sin\theta$. Thus $\nu_2 = -\nu_e sin\theta + \nu_\mu cos\theta$.

When a neutrino is produced the axis of interest is the flavour axis. If we consider a neutrino is created with a ν_e flavour then there will be no ν_μ component. This can be compared to polarised light whereby a beam polarised in the x axis will have an x component of 1 and a y component of 0. When the light beam passes through an x polarisation plane one would observe the full intensity of light. In the case of the neutrino we would expect that as the neutrino travels it's components will not alter and when it is absorbed an electron will be produced because it was of ν_e flavour when it was produced. This is, however not the case, the flavour axes are important in the production and absorption of neutrinos and the mass axes become important as the neutrino moves through space. The flavours have different masses but they have the same energy. The difference in masses that have the same energy results in a different momentum for each mass. This in turn means that there is a difference in DeBroglie wavelength for each flavour. Another analogy can be drawn to describe this phenomena.

A birefringent crystal contains two axes in which light that passes through it are split into two beams. The beams, called ordinary and extraordinary rays, exit the crystal at the same time due to the way the crystal is cut. Inside the crystal the two rays have different velocities, v_o and v_e. Now if we consider the wavelength, λ, and frequency, f, of this beam we can equate these to the velocity, $v = \lambda f$. In this case the two rays will have the same frequency therefore their wavelengths must be different and the rays are out

of phase. Assigning ϕ to the phase, the wavelength can be defined as a function of distance giving the phase advance, $\delta(\phi) = (2\pi/\lambda)\delta x$. This shows that as distance increases the phase continuously alters. The continuous change in phase with distance will change the plane of polarisation.

Neutrinos behave in an analogous manner, whereby if an electron neutrino is created it will pass through space which can be considered a birefringent crystal. This neutrino comprises of two components that propagate with different wavelengths and that in turn means the "plane of polarisation" rotates with distance. The detection of a solar neutrino with a Charged Current (CC) interaction effectively resolves the propagating beam into the fixed flavour components. Matter acts as a polariser aligned along the electron axis which is only one component of the neutrino beam. A Neutral Current (NC) interaction measures the full intensity of the neutrino which is similar to measuring light intensity independent of beam polarisation. Early detectors only saw CC interactions. Solar neutrinos are a mixture of ν_e and ν_μ flavour eigenstates at the point where they reach Earth. Typical energies of solar neutrinos when they reach Earth are of the order of MeVs. CC interactions require sufficient energy to produce leptons during interaction. Muons have a mass of 105 MeV/c^2, much higher than the energies of solar produced neutrinos, therefore early detectors were blind to muon neutrinos. The SNO [17] experiment detected both CC and NC interactions. The CC measurements were consistent with other findings, the measurement of NC interactions implied that the total neutrino flux was greater than the flux of electron neutrinos and consistent with the standard solar model. The conclusion from this was that neutrinos were altering flavour between production and absorption.

1.4 Neutrino Measurement

A neutrino travels through space as a superposition of three mass eigenstates, $m_1,\ m_2,\ m_3$, there is therefore a relationship between these mass states and the flavour eigenstates, $\nu_1,\ \nu_2,\ \nu_3$. The relationship describes the rotations between the two sets of eigenstates and is characterised by a mixing matrix,

which is analogous to the CKM quark matrix and is known as the Pontecorvo-Maki-Nakagawa-Sakata (PMNS) mixing matrix [18, 19, 20].

The variables of interest that describe the flavour-mass eigenstate within the mixing matrix are $\theta_{12},\ \theta_{23},\ \theta_{13}$, which describe the three mixing angles, and δ. δ is the phase factor, the value of this along with θ_{31} will determine whether there is Charge-Parity (CP) violation in the neutrino sector. The mixing matrix can be seen in 1.4. Where $c_{ij} = cos\theta_{ij}$ and $s_{ij} = sin\theta_{ij}$ where i,j = 1,2,3. Values for θ_{12} and θ_{23} have long been known and in 2012 the Daya Bay Collaboration published a value for $Sin2(2\theta_{13})$ of $0.089 \pm 0.010(stat.) \pm 0.005(syst.)$. The value for the phase parameter δ is currently unknown.

$$U_{PMNS} = \begin{pmatrix} c_{12}c_{13} & s_{12}c_{13} & s_{13}e^{-i\delta} \\ -s_{12}c_{23} - c_{12}s_{23}s_{13}e^{i\delta} & c_{12}c_{23} - s_{12}s_{23}s_{13}e^{i\delta} & s_{23}c_{13} \\ s_{12}s_{23} - c_{12}c_{23}s_{13}e^{i\delta} & -c_{12}s_{23} - s_{12}c_{23}s_{13}e^{i\delta} & c_{23}c_{13} \end{pmatrix} \quad (1.4)$$

Other measurements can be used to determine the values of the absolute mass differences squared $\triangle m^2_{31} = |m^2_3 - m^2_1|$ and $\triangle m^2_{21} = |m^2_2 - m^2_1|$. Confirming the sign of $\triangle m^2_{31}$ will show the relationship between the masses or the mass hierarchy.

To investigate the parameters that are still unknown further experiments are needed. A facility that is capable of producing an intense neutrino beam where the flavour of neutrinos being created is well defined will greatly contribute to determining these unknowns.

1.5 Future Neutrino Experiments

The value that was recently measured by Daya Bay of around 0.089 is larger than had been expected [21]. The value of this angle will affect which of the three proposed future neutrino experiments will be best suited to studying this elusive particle further. The following section will describe the three proposed experiments giving a more detailed overview of the Neutrino Factory (NF).

1.5.1 Super-Beam

A Super-Beam produces neutrinos via a conventional method whereby protons interact with a target producing π^+ [2] which then decay into μ^+ and ν_μ. It is these neutrinos that will be used in the super-beam proposal. This can be seen in the OPERA experiment where the CNGS beam uses this method to create neutrinos. The advantage of this approach is that the technologies used are well developed and understood. This method of producing neutrinos means that the neutrinos have a wide spread of momenta. A number of muons within the neutrino beam will decay, producing $\bar{\nu_\mu}$ and ν_e. The decay will contaminate the original ν_μ beam which will cause serious background in the $\nu_\mu \rightarrow \nu_e$ oscillation measurements. The natural decay of pions inherently gives the neutrino a random momentum kick, coupled with the initial interaction of the protons with the target means that the beam will not be well focussed. The challenge with this facility will be in the production of pions; the design uses a 4 MW proton beam therefore a target and horn that is capable of handling a beam of this intensity is required [22].

1.5.2 Beta-Beam

The proposed Beta-Beam facility [23] is one that employs a beta decaying isotope to produce neutrinos. The isotope is accelerated in the facility where it will decay. The accelerator will be in the form of a ring that will be directed towards a detector facility capable of seeing the resultant neutrinos. Two different isotopes will be required, one to produce ν_e and the other $\bar{\nu_e}$. The limitation of the Beta-Beam is apparent in the decay processes, the facility will only be capable of ν_e and $\bar{\nu}_e$ production. This facility would be cost effective due to current facilities such as CERN already having some of the equipment needed to build such a facility. Control over the intensity of the resulting neutrino beam will be harder because of the decay process used for neutrino production.

[2] π^- beams produce the charge conjugate states.

1.5.3 The Neutrino Factory

The NF [24] is one of the proposals that will go some way to fully understanding neutrinos. The difference between the NF, Super-Beam and Beta-Beam neutrino production facilities are the properties of the final neutrino beams they produce. The NF will use a similar method to the Super-Beam to produce its beam. Instead of using a pion beam as the neutrino source, the NF will create a muon beam which will be much more focussed and controlled, in terms of flavour, energy and intensity, with respect to the Super-Beam. The front end for the NF produces a high intensity pion beam. The decay of this beam produces muons. The muons are accelerated to the requisite energy. The muon beam will have a single energy compared to the pion beam which has a spread of energy. The resulting neutrino beam will have better collimation. The oscillation signal will be clearer because the oscillation wavelength depends on energy. This method will ensure only νs from the muon decay will form the beam. Selecting μ^+s will produce $\bar{\nu_\mu}$ and ν_e particles and selecting μ^-s will produce ν_μ and $\bar{\nu_e}$. Background can therefore be removed from the observations of $\nu_\mu \rightarrow \nu_e$ and $\nu_e \rightarrow \nu_\mu$ experiments. The disadvantage of the NF is the technologies used to produce a beam of this nature are not well formed although there are experiments developing the required components. To produce such a high quality muon beam an extra section is required within the facility that is not seen in the other proposals. This section will house the ionisation cooling equipment that reduces the emittance of the muon beam. Emittance shall be described in Section 3.4.

Ionisation Cooling

A practical demonstration of ionisation cooling of a muon beam has not yet been undertaken, this is the purpose of the Muon Ionisation Cooling Experiment (MICE). Ionisation cooling is the process of passing a particle beam through a material where the ionisation that occurs in the material will reduce all components of particles momentum. When the beam is then accelerated momentum is returned to only one component and the overall emittance is reduced. This will result in an intense and highly focussed beam

suitable for acceleration and storage. The storage rings can then point in the direction of a neutrino detector and when the muons decay the resultant neutrinos can be detected.

1.6 Muon Ionisation Cooling Experiment

The following thesis will describe the role of MICE in preparing for the proposed NF. It will focus upon the work undertaken by the author. Namely, the software that is used within the experiment and the geometry handling system that has been developed over the last couple of years. The Electron Muon Ranger (EMR) detector used in MICE will be examined and the work carried out to fully characterise the scintillator used in this detector will be described.

Chapter 2

Neutrino Factory

2.1 Introduction

The Neutrino Factory (NF) is one of the next generation of facilities designed to further study the neutrino. The following chapter describes the design of the proposal and the technical challenges that need to be overcome before the facility can be constructed.

2.2 Neutrino Factory Design

The NF's components have been outlined in the International Design Study for the NF (IDS-NF) [25]. The aim of the NF is to create an intense, highly focussed beam of neutrinos. Figure 2.1 is an image that depicts the proposed facility. The storage ring is of a 'racetrack' shape where the muons are given more time to decay in the long straight. When muons decay in this long straight the resultant neutrinos will continue to travel in the direction in which the straight is pointing. The initial mono energetic muon beam decays, creating a neutrino beam that is uncontaminated with pion products, whose flavour composition is better defined when compared with other methods. In order to create such a beam a number of components are needed.

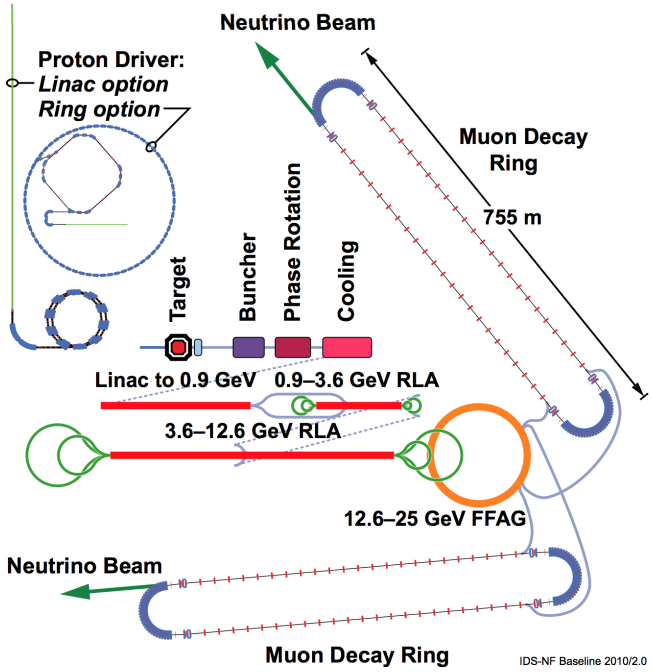

Figure 2.1: Schematic of Proposed NF [25].

2.3 Proton Driver

The proton driver will be the first stage of the NF and there are currently many sources and facilities available that produce protons. Current proton sources do not have high enough intensity to produce the muon flux required by the NF. A 4 MW proton beam is needed to meet NF designs, this exceeds current capabilities. A 4 MW beam will cause considerable thermal and mechanical shock to the targets which would rapidly lead to their failure. Next generation proton sources coupled with a number of proposed designs for the proton driver are being developed to provide this power.

The beam is being designed to be intense in order to maximise interactions with the target. The beam will also be comprised of short bunches. A bunch is a group of particles travelling together; most beams used in experiments are not a continuous beam of particles but rather a series of particle 'bunches'. A 1-3 ns RMS bunch is required for the NF to allow efficient muon capture. The proton beam can be accelerated up to 10-30 GeV.

2.4 Target

The proposed NF target will need to interact with a proton beam of 4 MW energy with a repetition rate of 50 Hz [25]. This represents an engineering challenge to create a target that can withstand this high power.

Many simulations have been carried out to determine the most effective design. One of the proposed solutions is to use a free-flowing moving target. The free flowing target will be a liquid mercury jet that will be injected into the proton beam. Solid targets that are conventionally used in experiments would eventually succumb to thermal shock and would melt, vaporise or disintegrate. Whilst interacting with the beam the target will become irradiated, the regular replacement of the damaged target would therefore be a risk. The proposal of using the free flowing target would overcome this challenge. Research and development for the mercury liquid jet has already been carried out at the MERIT experiment which ran at CERN [26, 27].

2.5 Muon Front End

This section of the factory will contain all of the elements required to capture the particles produced at the target and create a muon beam. Firstly there will be a pion capture and decay channel. This will consist of a solenoid that will send the particles into a helical motion. The helical motion allows particles with larger divergent angles from the central beam line to be captured. Following the decay channel will be a longitudinal drift channel where the pions and their daughter muons will be allowed to develop a position-energy relationship [25]. The beam will then pass through a buncher and phase-rotation system that collects the bunches and decelerates the highest energy particles and accelerates particles with lower energy. This will ensure that the energies of all the particles will be similar. The result is a series of muon bunches that have the same energy and a bunching to match the radio frequency of the ionisation cooling channel.

2.6 Ionisation Cooling

The ionisation cooling channel aims to reduce the emittance of the beam. To achieve this the beam will have to go through a number of Absorber Focus Coils (AFCs) and Radio Frequency Coupling Coils (RFCCs). The AFCs are designed to have interchangeable absorber materials; the absorbers will be of varying designs. A number of different shaped lithium hydride elements can be inserted into the beam line along with a hydrogen absorber. Passing the beam through these cooling materials will reduce momentum in all directions. To maintain the beams longitudinal momentum the beam will pass through an RFCC after the AFC. The RFCC will restore the beams longitudinal momentum and the overall result of the AFCs and RFCCs in the cooling channel will be a reduction in emittance. The engineering feasibility of this process is currently being studied by the MICE at the Rutherford Appleton Laboratory (RAL). MICE is constructing a single cooling channel that contains 3 AFCs and 2 RFCCs and aims to reduce the emittance by 10%. Emittance will be described in more detail in section 3.4.

2.7 Acceleration and Storage

Once the beam has passed through the Muon Front End and the Ionisation Cooling stages of the NF it will then move on to a set of accelerators. The beam at this stage requires fast acceleration and these accelerators need to have a high acceptance due to the beam's relatively high emittance. The design study shows that the best way to accelerate the beam is to use two 'dog-bone' recirculating linacs (RLA) that are linked to one another by chicanes. This can be seen in Figure 2.1. The final stage of acceleration will occur in a non-scaling Fixed Field Alternating Gradient (FFAG) accelerator. The use of the FFAG means that there is no need to alter the field and a high gradient field can be used for acceleration. The desired energy of the muons can therefore be reached within the muon lifetime.

After the acceleration process the beam will then be stored. The current proposal is to do this via racetrack storage rings. The rings will have short

radii at either end with long straight sections joining the turning circles together. The short radii arcs and long straights of this design increases the chance of decay in the straights rather than the arcs. The straight sections will be directed towards detectors through the earth where the resultant neutrino beam can be detected. Figure 2.2 depicts a racetrack ring.

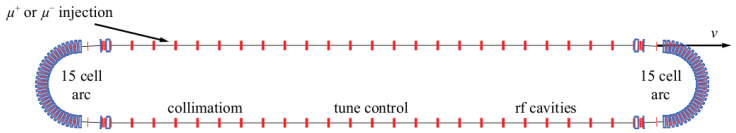

Figure 2.2: Illustration of proposed racetrack storage ring [25].

2.8 Detectors

In order to take an optimum measurement of θ_{13} and δ, two detectors will be needed. The near detector will be located close to the NF factory, its purpose is to characterise the beam. The far detector, placed around 7500 km away, will be used to measure any change in the flight between the two detectors. Creating identical detectors will limit the systematic uncertainties of the measurements. There is no final decision on a detector design but a proposal has been inspired by the detectors used in the MINOS experiment [28]. The proposed detectors are Magnetised Iron Neutrino Detectors (MIND) and are made up of layers of magnetised iron and scintillators [29]. They have an octagonal sectional area of 15 $\times$ 15 m^2 with a length of 63 m for the near detector and 125 m for the far. Each detector comprises of a 3 cm thick iron plane followed by two 1 cm thick planes of scintillating plastic. The plastic planes will be constructed of 15 m long 3.5 cm wide extruded scintillating bars. The two planes will be at right angles to one another and are read out by silicon Photo Multiplier Tubes (PMTs). The three layers are repeated along the length of the detector. The entire fiducial area will be housed in a toroidal field of the order of 1-2.2 Tesla. This design is likely to provide the basis for the NF detectors.

2.9 Summary

Future neutrino experiments will seek to fully characterise the unknown parameters that describe the neutrino oscillation phenomenon. The NF proposal describes the construction of a facility capable of producing a neutrino beam that is well understood and detectors capable of observing the particles which have passed through the earth. In order to construct a NF a number of principles need to be proven, foremost of which is the concept of ionisation cooling. A proof of concept experiment is needed that will demonstrate that the necessary amount of cooling is achievable.

Chapter 3

MICE

3.1 Introduction

To build a NF a number of technical challenges must be overcome, one of which is demonstrating that a muon beam can be cooled using ionisation cooling. The following chapter describes the MICE whose aim is to show a practical demonstration of ionisation cooling.

3.2 Aim

There are a number of problems in particle physics that results from the Large Hadron Collider will not address. The Muon Collider (MC) and the NF are two facilities that have been proposed to investigate a number of these problems [30, 31]. The NF will seek to further study neutrinos and aims to measure with high precision the parameters that describe the neutrino's behaviour. The MC will be used to further investigate and build on the Higgs Boson work currently being conducted at CERN. As these facilities are currently being designed, a number of technical challenges, which these facilities rely on, have to be explored and fully understood. One challenge is Ionisation Cooling. This process reduces the beam's emittance by passing the beam through a material where the particles lose momentum in three dimensions. The reduction in momentum results from energy loss as the

beam ionises the absorber material. After the beam has passed through the ionising material it is then re-accelerated in the longitudinal direction via a Radio Frequency (RF) cavity. The net result of this process is a reduction in emittance. A reduction in emittance means smaller beam line elements are needed resulting in less capital cost to build and a smaller field volume which in turn reduces running costs. A MC with low emittance beams will in result more collisions per muon. This event rate increase allows higher statistics to be gathered for the same run time and will increase the collider's efficiency.

A practical demonstration of Ionisation cooling is being carried out by the MICE based at the RAL in the UK, where achievable cooling is being measured. The aim of MICE is to measure a 10% reduction in transverse emittance of a beam of muons with 1% accuracy. Emittance shall be described in section 3.4. The required accuracy places stringent requirements on the control of systematic errors.

3.3 Future Experimental Requirements

Current colliders use protons or electrons as the beams in order to investigate the fundamental properties of matter. Protons are made up of many quarks; proton-proton collisions produce huge amounts of background and only a small fraction of the resultant particles are of interest. A way to reduce this background is to use an elementary particle such as a lepton. Cleaner events can be achieved through the use of electrons. However, the use of electrons produces a new challenge. Accelerated electrons emit synchrotron radiation, the energy lost must be replaced which limits the maximum energy achievable in circular colliders. Collider experiments seek to have the highest energies possible, and limiting the maximum energy would be undesirable. Using a linear collider would remove the effects of synchrotron radiation but would increase building costs substantially. Substantially increased cost is hard to justify therefore a more cost effective solution must be sought. Heavier particles lose less synchrotron radiation so using muons instead of electrons will significantly reduce the energy loss. Thus a muon collider is the ideal lepton collider, providing the other technical challenges can be overcome.

A muon beam suitable for a muon collider will provide an intense, well collimated beam of neutrinos suitable for use in a NF. Thus results from MICE could form the keystone of two future machines.

3.4 Emittance

Emittance can be described by considering a beam passing through a pinhole, Figure 3.1. Take point A, for a pinhole there is only one path that the particles can travel to get to this point. There is perfect correlation between the position and angle. Placing a quadrupole downstream will produce a parallel sided beam that has an emittance of zero[1].

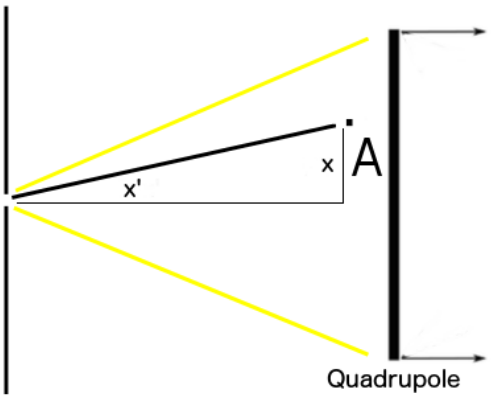

Figure 3.1: Diagram of a beam travelling through a pinhole. x equals distance and x' represents the angle.

The equation defining emittance is $\epsilon_x = \langle x^2 \rangle \langle x'^2 \rangle - \langle xx' \rangle^2$ [32]. If $x' = kx$ then $\epsilon_x = 0$, emittance is therefore a measure of correlation between beam position and angle.

If the beam was not passed through a pinhole but through a larger hole then the effect would be different. Figure 3.2 illustrates what would happen in this scenario. Let us consider A again, for this position there are multiple paths the beam can take to reach this point. In this scenario a particle

[1] A single quadrupole will focus in one transverse plane only. Using a set of quadrupoles will produce a parallel sided beam in both transverse planes.

arriving at a given transverse position may have a range of angles. This results in an emittance that is greater than zero. A quadrupole will bend particles by the same angle at the same x and because the particles moving through any axis at a given distance from the centre point will have varying angles, any attempt to produce a parallel beam via a quadrupole will result in the effect seen in Figure 3.2. Introducing more quadrupoles will never create a parallel beam. The angle that a particle trajectory makes with the beam axis is related to the fractional transverse momentum P_x/P_{total} and either can be used as x' although the actual value of ϵ_x depends on the choice.

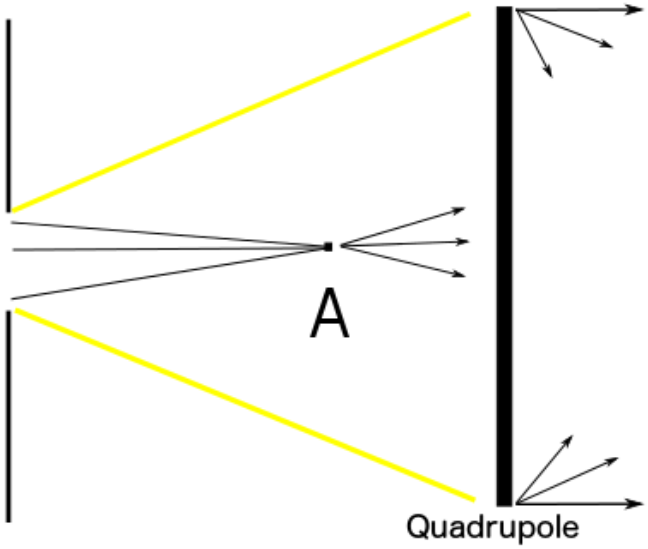

Figure 3.2: Diagram of beam travelling through a large hole and a lens.

A non-zero emittance is inherent in the mechanism by which muons are produced: as a particle decays it receives a random momentum of energy altering the direction of travel. Figure 3.3 illustrates this random kick. The pions produced from the proton beam have a range of production angles. Each of the resultant pions will then decay introducing a random momentum kick. The relationship between position and transverse momentum for the muons will become smeared, increasing the emittance of the beam. There is now a smaller correlation between position and transverse momentum for the muons. Figure 3.3 shows that although the beam will have a longitudinal

energy, in this example it is 200 MeV, there will also be random transverse momentum within the beam. Reducing the transverse momentum will decrease the beam's emittance and this is MICE's aim. The reduction of emittance must be as great as is possible because as the muons decay, again there will be a random kick of energy. The neutrinos produced from this decay will have a higher emittance than the muon beam due to this energy kick. Unfortunately, the emittance of the neutrino beam cannot be modified because neutrinos are uncharged and have only feeble interactions.

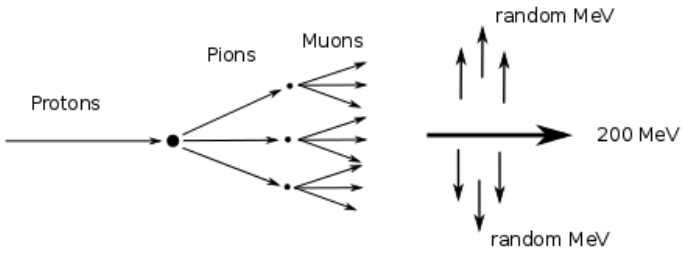

Figure 3.3: Diagram of how high emittance occurs with the creation of muons.

The short lifespan of muons increases the complexity of beam line technologies that can be used. A low emittance beam will reduce the cost of such technologies.

3.5 Ionisation Cooling

Ionisation cooling is the process of passing a beam through an ionising material in order to reduce the momentum of each particle in the beam. Once this reduction has taken place the beam can then be re-accelerated in the longitudinal direction resulting in a reduction in emittance. To describe the effects, consider a muon moving with momentum $\bar{p_1}$. After the beam is passed through ionisation cooling material the beam will be reduced in energy and the resulting momentum will be $\bar{p_2}$.

Once this stage is complete the muon is re-accelerated in the longitudinal direction adding momentum $\bar{k}$, resulting in a final momentum $\bar{p_3}$. Figure

3.4 shows the result of one stage and Figure 3.5 illustrates the process being repeated and the final vector coloured in green shows the muon with a much reduced transverse momentum.

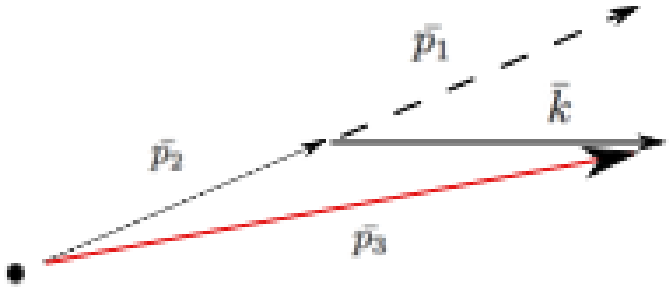

Figure 3.4: Diagram illustrating the reduction in transverse momentum of a particle.

The overall beam emittance is reduced because each individual particle's transverse momentum is reduced whilst maintaining its longitudinal momentum.

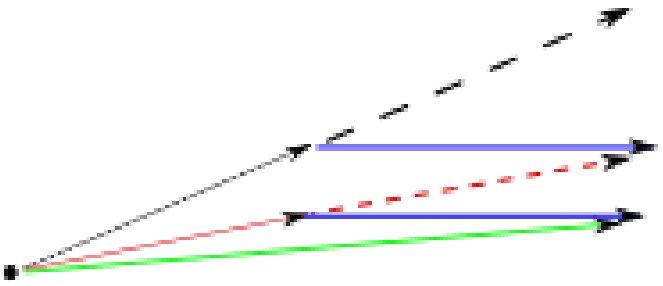

Figure 3.5: Diagram illustrating the effect of transverse momentum reduction on a particle that has been cooled twice.

Introducing material into the beam line will reduce the momentum of

each particle but does introduce the effect of multiple scattering. As particles traverse material they not only lose energy but are deflected from their trajectory which increases emittance. This is known as heating. The change in emittance with distance is given by;

$$\frac{d\epsilon_n}{ds} = -\frac{1}{\beta^2}\left\langle\frac{dE_\mu}{ds}\right\rangle\frac{\epsilon_n}{E_\mu} + \frac{(13.6\ MeV)^2\beta_\perp}{2m_\mu X_0\beta^3 E_\mu}$$

Where ϵ_n is the normalised emittance, E_μ is the Energy of the muon, m_μ is the muon mass, X_0 is the radiation length of the material and βc is the velocity of the muon. Emittance as previously defined is energy dependant. By defining the normalised emittance $\epsilon^* = \beta\gamma\epsilon$, beams of varying energy can be directly compared. This equation represents the change in emittance as a function of distance s. The first and second terms of the equation are the emittance reduction and heating term respectively. The emittance reduction term depends on the energy loss whereas the heating term depends on the radiation length. The radiation length decreases with the atomic number of a material. It must also be noted that $\beta_\perp$, the transverse β function[2] for the beam, must be as small as possible. The transverse beta function is related to the size of the beam at a point along its trajectory. Focussing the beam to a small area during the cooling process reduces the value of this function. To reduce the effect of heating upon emittance a material with the lowest atomic number must be selected; hydrogen. In order to use a material with a reasonable density liquid hydrogen must be used but this introduces significant engineering challenges. The walls of the vessel that will house the hydrogen must be as thin as possible in order to keep the heating effect to a minimum. The vessel must also be strong enough to mitigate the danger of housing an explosive material using cryogenic methods. Due to hydrogen's explosive nature solid Lithium Hydride absorbers, which have the lowest mean atomic number, of any solid, will also be used in the experiment. The absorber components of the beam will also make use of coupling coils in order to have a strong focus whilst cooling to reduce the heating effect to a minimum. There are other cooling techniques available such as stochastic

[2] β is used with two meanings in the emittance formula. This follows normal convention.

cooling [33] and electron cooling [34, 35], however the muon's short life span makes them inappropriate.

3.6 MICE Configuration

RAL based at Didcot, Oxfordshire has a synchrotron known as ISIS. ISIS is a neutron spallation source that uses a proton beam directed towards two targets in order to produce neutrons. The MICE hall is set off of the main synchrotron where it dips a titanium target into the ISIS proton beam to produce pions. Its configuration is as follows.

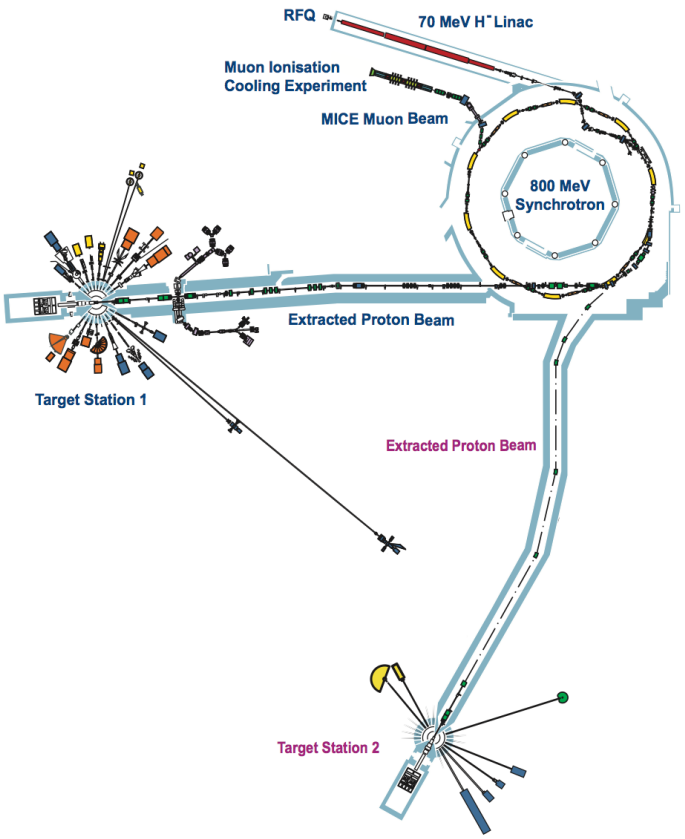

Figure 3.6: ISIS Schematic [36].

Figure 3.6 shows the layout of the ISIS synchrotron. The beam is initially

injected into a Linear Accelerator (LINAC) that accelerates it to 70 MeV before it enters the synchrotron. The synchrotron comprises of 10 sections, S0-S9, where the proton beam is accelerated to 800 MeV. This process is repeated 50 times per second. The beam can then be directed towards two target stations, Target Station 1 and Target Station 2 on the schematic, where the beam interacts with a tungsten target and neutrons are created via spallation.

MICE's target is located between sections 6 and 7 where a titanium target is dipped into the beam to produce pions. The pions are then directed, by quadrupole focussing (Q1-3) and dipole bending magnet (D1), towards a solenoid known as the Decay Solenoid (DS). The dipoles select particles with the correct momentum. Particles that are at an angle to the beam axis will be captured by the DS; these would be lost before reaching the experiment if not for the DS. Once in the DS they follow a helical path that increases the distance that the particles will travel, affording the pions time to decay to muons. Muons that exit the DS are momentum selected by the dipole magnet D2.

The cooling channel comprises of two AFCs and three RFCCs. The entire beam line also contains instruments which are used for particle identification and tracking.

Figure 3.7 shows the layout of the MICE experiment. The muons selected by D2 are focussed by a pair of quadrupole triplets, Q4-6 and Q7-9. The beam's shape and particle make up must be determined; this is done by a number of detectors. The muons must be distinguished from the pions and electrons that contaminate the beam. At the point when the beam leaves the Decay Solenoid Area (DSA) it will be mostly muons. The experiment is designed to produce three different levels of normalised transverse emittance which are 3, 6 and 10 mm for momenta between 140-240 MeV/c. The muon beam is then ready to enter the cooling channel which cannot be seen in Figure 3.7 but is located between TOF1 and TOF2 as seen in Figure 3.8.

As can be seen from Figure 3.8 there are a number of detectors that are used within the cooling channel. They fit into two categories; the first set of detectors are for particle identification, the second set are for particle track-

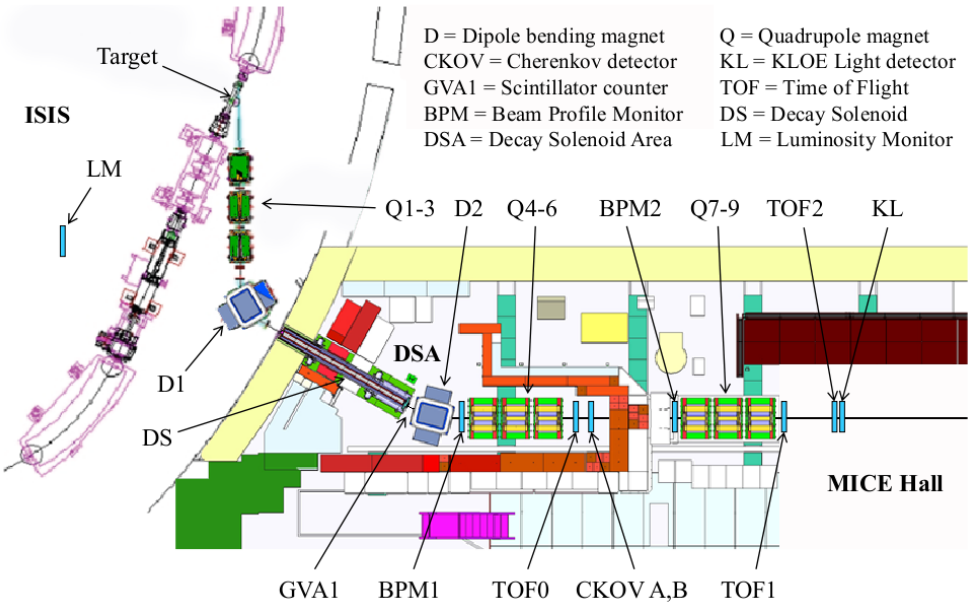

Figure 3.7: Schematic of MICE layout. This is as used in Step I in the experiment and depicts the experimental layout and positions of the detectors and magnets. The cooling channel will be installed after TOF2 and KL, everything before these detectors constitutes the μ beam line [37].

ing. A combination of these two types of detectors gives a measurement of the emittance of the beam. Muons that do not decay in the cooling channel are selected by the PID detectors. The scintillating fibres housed in spectrometer solenoids within the trackers measure the position and momentum of the selected muons. Combining the measurements for many muons the change in emittance, for an input beam of given emittance, can be measured. A single cooling channel section is considered to be an absorber and a set of cavities. A series of cooling channel sections would be required to cool a muon beam sufficiently for use in a NF.

The construction of MICE has not yet been completed and for the purpose of maximising data taking whilst construction of components is carried out the experiment was split into Steps.

Figure 3.9 shows the staged construction of the experiment. Each Step of the experiment is designed to fully test each component as it is installed. Steps I-III aim to fully test the Time of Flight (TOF) detectors and the

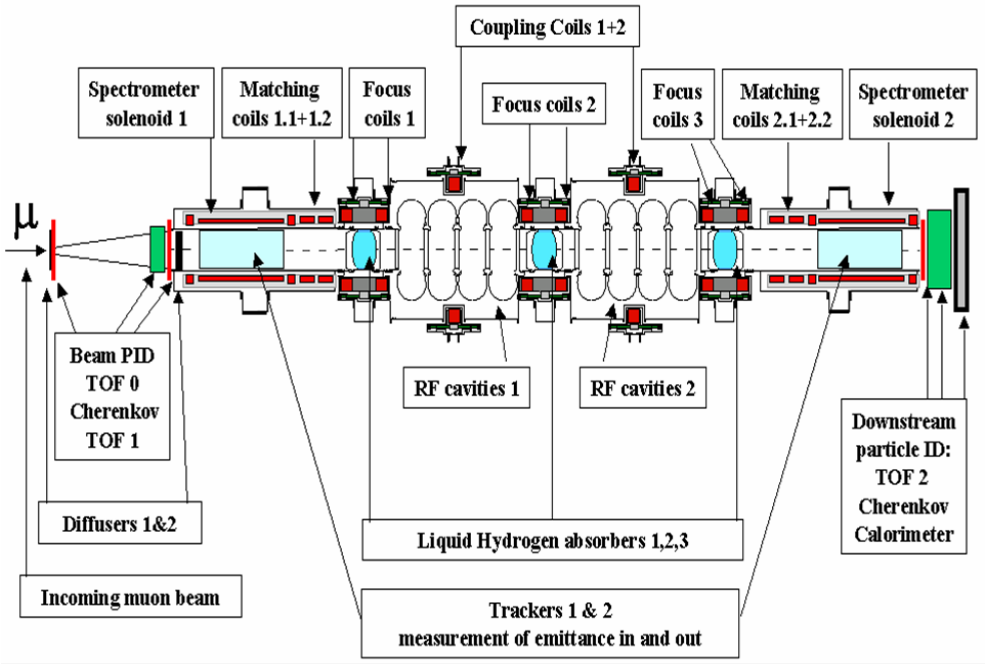

Figure 3.8: Schematic of cooling channel components [37].

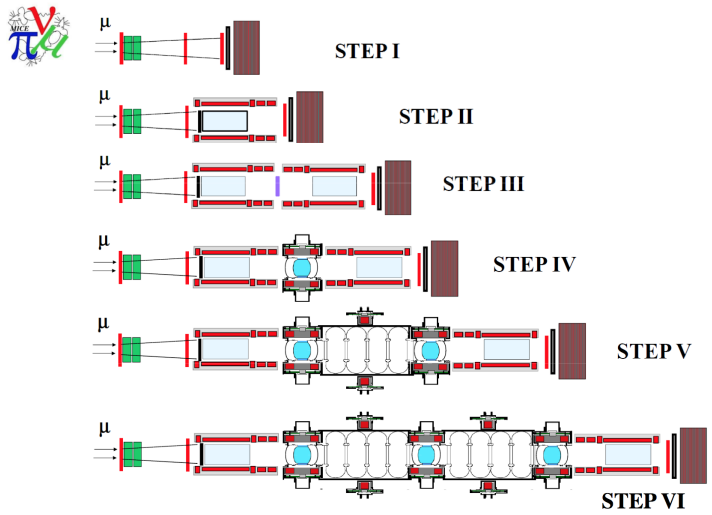

Figure 3.9: Illustration of proposed Steps of construction for MICE [37].

trackers. There will be no cooling conducted during these stages of the experiment, the aim is to ensure the detectors correctly identify the different particles. The latter steps of the experiment will implement the cooling com-

ponents. Step IV will install a single absorber and will investigate the effect of cooling upon the beam. The next step will then add a second absorber and an accelerating component. This represents a section of the entire cooling channel and will investigate the effect of cooling and re-acceleration upon the beam. The final step will house the entire cooling channel.

3.7 Beam Production

In order to produce the pions needed for the experiment, MICE uses a cylindrical titanium target. The target is located in sector 7 of the ISIS synchrotron where it is dipped into the ISIS proton beam. The interaction of the protons with the target produces the pions that are captured and directed down the beam line. The target is housed in a frame where it can be placed into two positions. The first is the raised position, this makes the target safe even if the target itself were pulsing there would be no interaction with the beam. The second position is where the frame is lowered. Pulsing of the target in this position moves it into the ISIS beam. To maximise pion production while minimising disruption to the beam, the target must interact with protons at their highest energy, this means the target must dip into the beam in the last 2 ms of the ISIS cycle before extraction [38]. Minimising beam loss is important as this will ensure the area around the target does not become active, allowing safe maintenance of ISIS. To avoid interference with the next ISIS cycle the target must be raised before the cycle begins and this means the target must accelerate at roughly 800 ms^{-2} [38]. To achieve this acceleration the target has been designed to be pulsed by magnets which are attached to the target shaft and are controlled by 24-coil stators. There are sets of bearings which keep the target in a vertical position. A schematic of the target can be seen in Figure 3.10.

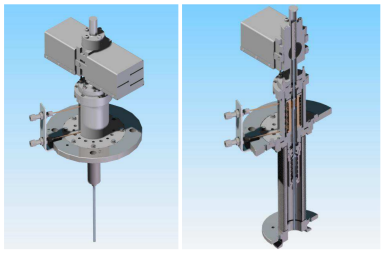

Figure 3.10: Schematic of MICE target, (left) illustrates the target without bellows, (right) is a cutaway view [38].

3.8 Detectors

The different types of detectors in the beam line have already been briefly mentioned. This section will describe each detector and its role in the cooling measurement.

3.8.1 Time of Flight

There are three TOF detectors within the MICE beam line. Their main purpose is particle identification, separating muons from electrons. The detectors are segmented and so some beam profile measurements may also be made by the TOFs. Each detector comprises two layers of scintillators that are made up of individual scintillating bars. Each bar has a PMT connected at each end and the two layers are orientated perpendicular to one another. Figure 3.11 shows the configuration of the TOF detectors. Although there are some minor variations between the three detectors, they all follow this design. The difference between each detector is in the number and width of the scintillating bars they contain. TOF0 and TOF2 both have 10 bars per layer, however the bars of TOF0 are 40 mm wide whereas TOF2's bars are 60 mm. TOF1 has 7, 60 mm wide, bars per layer. Each detector has a timing resolution of 50-60 ps [39].

The TOF counter provides a measurement of time as a charged particle passes through it. Placing a number of TOF detectors a known distance apart allows the velocity of a particle to be determined. Within MICE D2 selects particles within a range of momenta. Combining this with the velocity

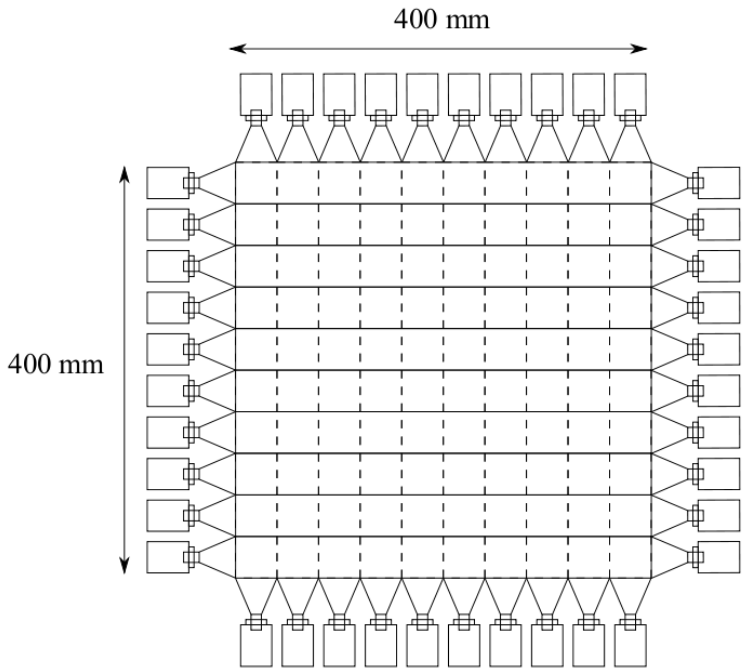

Figure 3.11: Schematic of TOF detectors.

allows the mass of the particle to be estimated and the particle type can be deduced.

3.8.2 Cherenkov and KLOE Light detectors

The Cherenkov (Ckov) and KLOE Light (KL) detectors will provide particle identification via the light given off by the particles as they traverse the detectors. The Ckov detector measures the Cherenkov radiation, which is produced when particles travel faster than the speed of light in the media. At this point in the beam line the beam has already been momentum selected by D2. Identifying particles that exceed the Cherenkov threshold of the medium allows a limit to be placed on velocity, from this a limit on the mass can be set. Combining this with the measured velocity taken from the TOFs allows MICE to define a very pure beam. The required accuracy for the experiment means that even the smallest amount of contamination could compromise the measurements.

3.8.3 Trackers

There will be two trackers in this experiment. One will be placed before and one after the cooling channel, an independent emittance measurement will be taken from both. Systematic errors will be reduced to a minimum by the similar construction of both detectors. Running a muon beam through the cooling channel without the absorber in place will produce an almost identical beam in both detectors. Comparing the measurements for each detector will help to set limits on systematic uncertainties.

The Trackers are placed in a solenoid and consist of five stations. The stations are not placed at equal intervals throughout the detector, this helps to resolve ambiguities during track finding. The configuration of the stations within the tracker itself can be seen in Figure 3.12. Each station consists of three layers of 350 μm scintillating fibre. These fibre planes are held in place by a carbon fibre station body which aligns each layer at 120° to the other layers [40]. This allows a determination of the two co-ordinates transverse to the beam with some redundancy in the measurement.

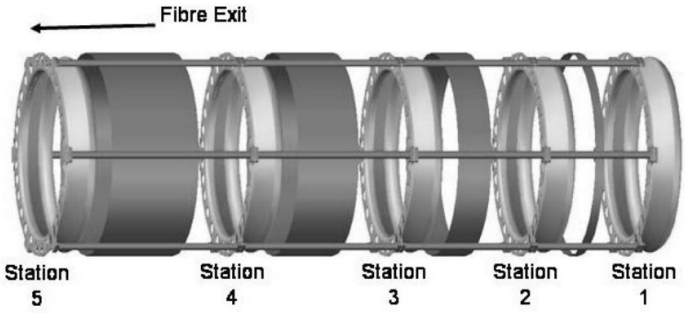

Figure 3.12: Schematic of tracker station positions. [40].

As particles pass through the detector they will cause the fibres they cross to fluoresce. A Visible Light Photon Counter (VLPC) is used to measure the light produced by the fibres. The effects of placing material into the beam line and heating the beam were carefully considered during the construction of the tracker. Combining thin fibres with highly efficient photon detectors reduces the amount of material in the beam line and avoids compromising

the emittance measurement. The construction of the detector can produce a space point reconstruction efficiency of 99.8% [40].

3.8.4 Electron-Muon Ranger

The Electron-Muon Ranger (EMR) is a 1 m^3 totally active detector. There are 48 planes such that each plane is at right angles to the planes either side of it. Each plane has 59 triangular scintillating bars with a Wavelength Shifting (WLS) fibre running through the centre. An illustration can be seen in Figure 3.13. This fibre transports the light collected in the bars to the PMTs at each end of the planes.

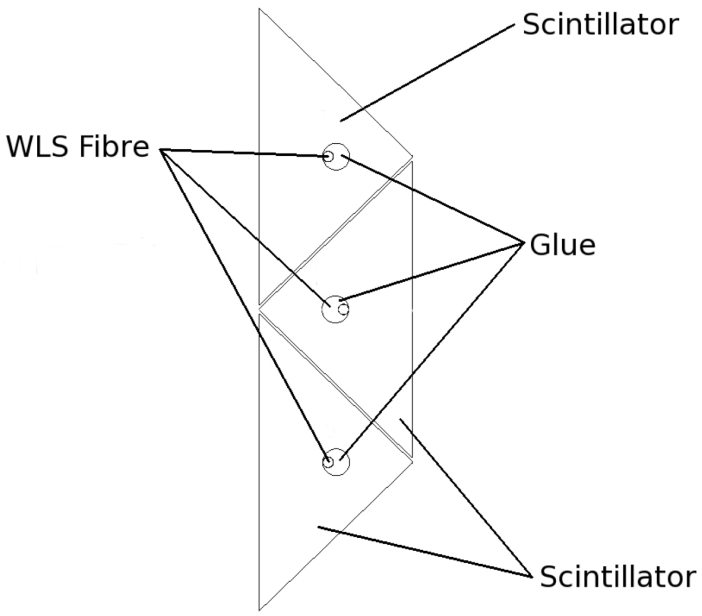

Figure 3.13: Schematic showing a cross section of the EMR scintillating bars. Adapted from source [41].

At one side of the plane there will be a single anode PMT that will collect all of the light from the entire plane giving the total energy of that plane. The other end of the plane will house PMTs connected to each individual bar giving the energy deposited per bar. The information gathered by the PMTs

will give positional data on the particle's trajectory. Figure 3.14 illustrates a single plane.

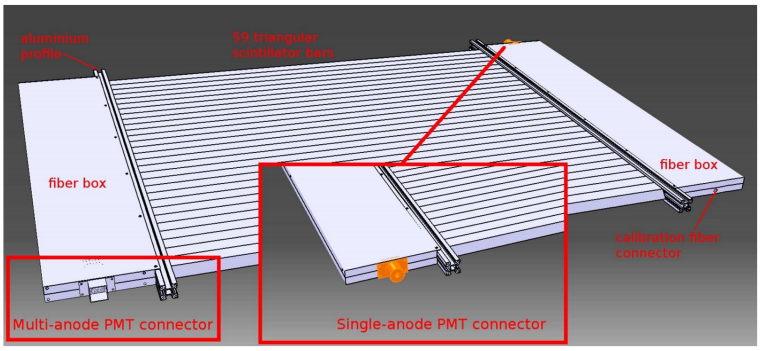

Figure 3.14: CAD drawing of a single EMR plane. The bars are connected to PMTs via clear fibres housed in fibre boxes at the ends of the bars [42].

The aim of the EMR is to absorb as much energy as possible from the beam in order to perform particle identification. The particles of interest are electrons, muons and pions. Each of these behave differently when interacting with the EMR. Electrons will deposit energy uniformly across each one of the bars as they pass through the detector. Muons and pions will exhibit an energy spike at the point where they stop and then decay. A particle shower is the result of the decay and it is this shower that causes the energy spike. The principle of detection is a simple and elegant solution to particle identification. The set up of the PMTs allows a full energy spectrum of the whole detector to be evaluated and the recognition software will be able to identify particles by the way they interact with the scintillating layers. Particle identification occurs by analysing the range into the detector a particle has travelled. Pions will decay causing a high energy peak close to the face of the detector that the beam enters. Muons will display a high energy peak further away from this face whereas electrons will not decay depositing lower amounts of energy on each plane. A simulation of the detector can be seen in Figure 3.16, the range at which the particles decay can be seen.

Identifying muons that have reached the end of the beam line with a high degree of certainty has already been stressed, placing the EMR at the

end of the beam line will ensure that only muons are included. There will be instances within the cooling channel where particles will have decayed. This decay, if left unidentified, will add to the uncertainties of calculating the cooling effect because this is based on the assumption that all particles within the calculation are muons. The EMR will help to confirm the information given by the TOFs, however, if a muon were to decay during the cooling channel the resultant electron may continue through the entire beam line with a time of flight indistinguishable from an undecayed muon. It is this contamination that needs to be removed from emittance calculations, because the decay of the muon will give the resultant electron a transverse momentum kick. This kick will affect the beam's emittance.

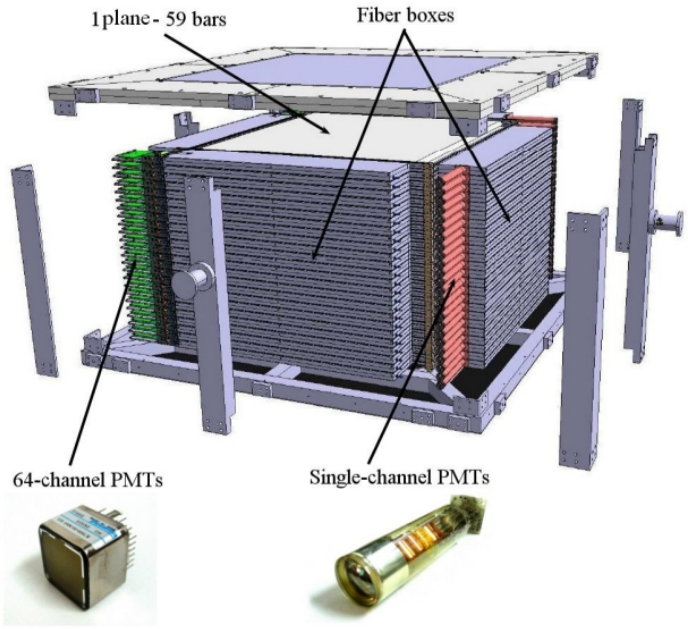

Figure 3.15: Illustration of EMR [43].

Figure 3.15 shows the assembly of the EMR, the beam will enter the detector from the top of the image where the particles will deposit energy on each of the layers.

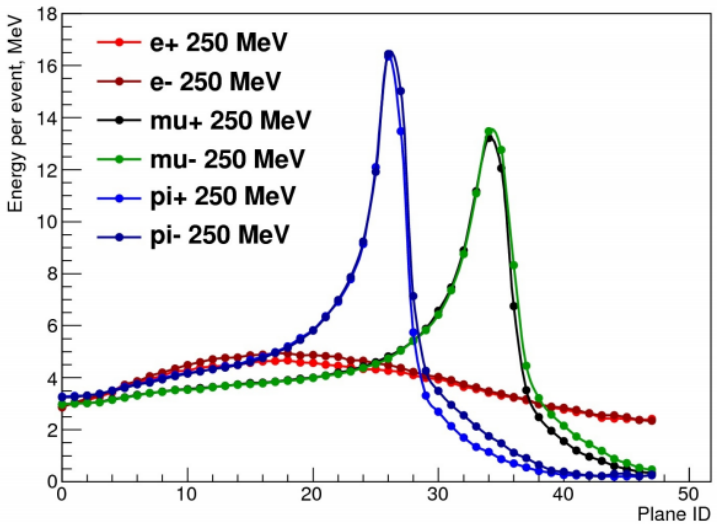

Figure 3.16: Energy distribution of particles within the EMR [41].

3.9 Cooling Channel

The ionisation cooling channel will consist of three AFCs and two RFCCs. The cooling channel will pass the muon beam through the absorbers that will reduce the beam's momentum in the x, y and z directions. The RFCCs will then re-accelerate the beam in the longitudinal direction only. The end result will be a reduction in emittance and the two trackers will be the main tools for detecting this reduction. This section of the beam will be enclosed in solenoids to provide focussing of the beam.

3.9.1 Absorber Focus Coils

Cooling will take place in the AFCs, this will be done via blocks of lithium hydride or liquid hydrogen, at a point where the beam is strongly focussed. The beam will interact with these blocks as it passes through the focus coil. The material selected for this cooling procedure has been carefully considered. Multiple scattering is an effect that increases beam emittance, therefore the absorber and it's container must have as little multiple scattering as possible, which means the lowest possible atomic number. The relative effect of multiple scattering can be further reduced by placing the absorber at the

strongest focus point.

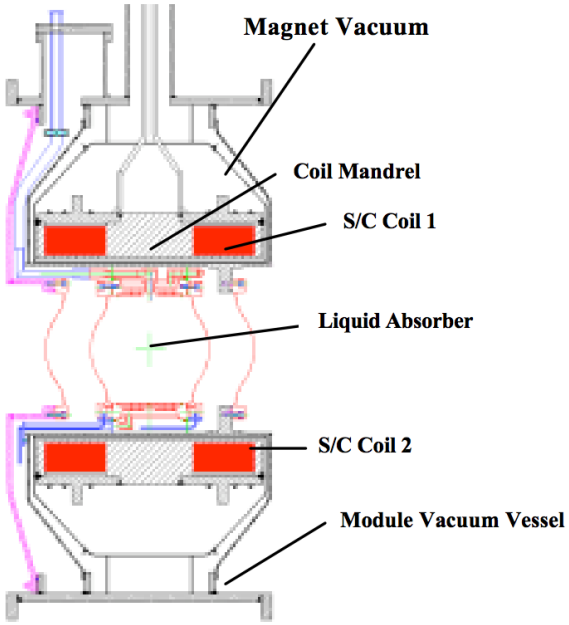

Figure 3.17: Schematic of AFC cross section [44].

Figure 3.17 is a schematic of the AFC. The AFC has been designed to be able to swap the absorbing element. The hydrogen can be changed for the lithium hydride blocks to evaluate the performance of both materials. The schematic displays the vessel in which the liquid absorber will be placed and the design is such that this vessel can be removed.

3.9.2 Radio Frequency Coupling Coils

The second process of reducing emittance is to re-accelerate the beam in the longitudinal direction only. The combination of these two processes is to reduce the momentum in the x and y direction of the beam whilst maintaining the z momentum. The RF cavities provide this re-acceleration.

3.10 Summary

This chapter describes the aim of MICE to reduce the emittance of a muon beam by 10%. In order to accurately predict the performance of a realistic cooling channel the emittance reduction must be measured to 1% accuracy, leading to the requirement for a one part per mill measurement of emittance. Protons interacting with the titanium target produces pions. The pions are captured and are allowed to decay to muons. The muons are then passed through a tracker that will be used to measure the beam's emittance. The beam is then passed through absorbers where the momentum is reduced in all three directions. After this the beam is re-accelerated in the longitudinal direction only. A second measurement is then taken after the cooling channel where the effect of cooling can be determined. The overall result being a reduction in transverse emittance, which is measured by the second tracker. The composition of the MICE beam line cooling channel represents a single cooling section to be used in future experiments.

Chapter 4

Geometry

4.1 Introduction

This chapter will describe the work that was carried out during the overhaul of the MICE software package; the need to move from the previous method of geometry modelling and the management thereof, to a new system and the inherent flaws of the previous software package, specifically the geometry management, that meant that improvements were urgently required. This chapter focuses on the work done to improve the geometry for the new software package.

The first section will give an overview of the underlying software physics engine GEANT4 (G4) [45], the legacy software package used by MICE G4MICE [46] and its replacement Modular Analysis User Software (MAUS) [47]. It will then go on to describe the motivation to move to a new software package, and the geometrical modelling challenges faced by G4MICE that brought about the implementation of the improved Geometry Handling System.

4.2 Simulation Software

There is a fundamental need for a physics simulation package when undertaking a large physics experiment. The software packages allows the results

taken from the experiment to be analysed and understood. The need for the package to be accurate is paramount when considering the accuracy required by MICE.

This software package comprises of a number of components which are; the analysis system, the Monte Carlo system, the physics engine and the geometry modelling system. The analysis system reads the results that can either come from the experiment itself or are generated by simulation and performs the analysis required: an example of this would be to analyse the results from one of the trackers to calculate emittance. One of the methods to produce results is by simulation, the Monte Carlo system provides the ability to simulate an entire physics run, which may contain thousands of particles starting from the target, and simulate these particles travelling through the beam line. The physics engine gives the package the information on how the particles behave as they propagate and finally the geometrical model defines the physical positions and structural make up of the beam line components within the experiment.

4.2.1 GEANT4

G4 is a physics simulation software that is widely used within the physics community. It provides the physics engine, some analysis tools and the ability to create geometrical models. The details of the physics engine and other tools that are provided with G4 are not relevant to the geometric modelling and will not be discussed. The method of constructing geometrical models is the focus of this chapter.

The creation of geometrical models by G4 is done in a modular manner. G4 provides the user a library of geometrical primitives, such as boxes and cylinders, whose size can be defined by the user. One or more of these primitives can be placed within a larger volume of space relative to one another to create more complex shapes. As with the base shapes, the complex shapes can then be placed in another volume of space relative to other complex shapes in order to create components. This hierarchical model can continue as far as the user requires. Typically a large world volume is created that

contains smaller volumes that describe complex components comprised of primitives. Each shape's material can also be defined in order to provide the physics engine the information required to accurately simulate or model a particle's behaviour within that volume. Shapes or components within the world volume may be defined independently and do not have to reflect the material of the parent volume or shape.

A simulated particle will traverse a number of materials as it moves through the geometrical model; understanding the energy loss due to scattering and the direction changes that a particle is subjected to is core to the software package. Different materials will give different levels of energy loss and directional change and must be defined for an accurate simulation. The information regarding the particles motion relating to this, position and momentum, are stored by G4 at all times. G4 materials may also be defined to be 'sensitive' which is used in modelling detectors, further details on sensitive detectors can be found in section 4.5.3. The geometrical model includes that which cannot be seen, such as electro-magnetic fields. The fields are those that are seen in quadrupoles and dipoles and are needed in order to bend or focus the particles. Defining the fields within the volume is similar to that of creating shapes. The centre point of the field within its parent volume must be specified. The field can then be input into the model by either a field map, where each x, y, z position is given a field strength or by using the G4 field engine that will generate the required field during simulation.

G4 as a package provides the basics needed to simulate experiments. The package includes the fundamental building blocks required for users to model their physical experiment and how the model affects particles as they move through it.

4.2.2 G4MICE

G4MICE is the legacy software package used by MICE. The base platform package for G4MICE is G4 which has had its functionality extended to satisfy MICE specific requirements. The requirements mainly relate to the analysis system and how this generates results for the detectors that have been built

for MICE but does include other experiment specifics. The method to create geometrical models is inherited from G4 in that it uses the base shape library and hierarchical construction. Specific examples of the construction of models will be detailed in section 4.3.1.

4.2.3 MAUS

G4MICE was the software package that had supported the experiment. Over time the experiment increased its complexity and it became clear that the methods used to create G4MICE were no longer viable in supporting the increasing complexity. At the time there were concerns that the existing software would prove inadequate to the task of analysing experimental data. The newly formed software group for MICE decided to create a new package, MAUS, for the experiment. One part of the improvement was to create a more reliable method of creating and managing geometrical models. I was responsible for this work.

G4MICE contained some core systems that were migrated from G4MICE as significant effort to re-write them would have been needed. The overhaul of the package included re-writing the custom analysis code specific to MICE, incorporating software engineering best practices for the software group such as continuous integration and creating a governance protocol over the code that was being written. This ensured that the code that was written was well documented, tested and owned by specific members of the software group. G4MICE did not have these procedures and as the experiment grew, management of the package had become unreliable.

MAUS has been developed using industry practices to support the MICE collaboration. It provides the experiment the ability to analyse data from either Monte Carlo simulation or from results taken from the experiment. G4 is a toolbox providing the users the building blocks; specific details of the experiment are provided by the user and coded on top of what G4 provides. The experiment specifics will take energy deposited within the modelled detectors and turn this into numbers that would emerge from the Data Acquisition (DAQ) system ready for analysis. The data output from the Monte Carlo

and the experiment are identical, ensuring results from both are directly comparable.

4.3 Geometry Improvements

Improvements to the geometry within MICE's software package were needed for a number of reasons. Creating models for G4MICE was done in an ad hoc way. Users could create a model to describe the experiment using MICE specific G4MICE data files as they saw fit. The data files were read in by G4 and converted to G4 primitives. The user would often use engineering drawings as the base for their models, but would rarely identify the drawing and revision number involved. Over time a variety of models were created and used by various parts of the MICE collaboration. Individuals would verify a model by hand but no system existed to document this process and it became difficult to determine which model was accurate or indeed worked. Each model that was produced was not checked for accuracy, validated as a viable model for simulation or audited for its initial purpose. The models that came with G4MICE could not simulate a particle beam, that started at the MICE target, past D2. At this point the beam would travel into the dipoles wall and go no further. The libraries of shapes provided for users to create the beam line elements make it extremely difficult to create the shapes seen within the experiment. The quadrupoles used contain x-shaped apertures which, without significant effort, cannot be accurately modelled by hand. A trustworthy model built using a well defined process was needed to solve these problems; the new geometry system needed to provide a method to create new models to reflect the ever changing experiment with the flexibility to include geometrical details as the simulation and experiment grew more complex.

Initial work on the geometry simulation began by looking to improve the hand written models in order to create a geometry model that was closer to reality than the legacy files. Altering the files by hand and comparing the alterations to engineering drawings was the first part of this project.

4.3.1 G4MICE, Legacy Code and Implementation

A geometry model for G4MICE was constructed using hand written data files; written with MICE specific syntax. These described base primitives, their location within their parent volumes and so on. The result was a series of hierarchical text files that described the global volume containing the experimental arrangement of beam line elements, detectors and their sub-components. An example of one of these files can be seen in Figure 4.1. This example is known as the configuration file; this file describes the world volume and places each beam line element within it. Each element has its own file that describes where each of its own components are placed relative to the beam line element's centre point. The configuration file can be considered the parent geometry file because it describes the overall volume and experiment. It must also be noted that child files, containing beam line elements, can also contain children as this structure is recursive.

A single slab of a TOF detector, which is one of its simplest components, can be described by a G4 primitive. This represents an element at the bottom of the geometry hierarchy. Figure 4.2 shows the description of a TOF scintillator slab; this example is a simple box made of polystyrene. A number of these slabs can be used to define one of the TOF's detector planes. This is done in the manner shown in Figure 4.1, replacing 'Module AFC/AbsorberFocusCoil.data' with 'Module TOF/TofSlab.dat' and would include this file, Figure 4.2, in the configuration file.

The method of creating geometrical models by hand introduces human error and does not provide a way to verify and validate the models created. Models created using the G4 primitives resulted in over-simplified geometries. G4MICE had no process to ensure the models were correct. A test driven approach to model creation that was well documented and managed was built for MAUS.

During the initial investigation into G4MICE's geometry it was found that some of the modelled beam line elements were not accurate and were constructed in a way that could have caused problems within the simulation. As an example, it was found that the quadrupole's aperture was modelled

```
// Stage 6 Floor Plan, z=0 at middle H absorber

Configuration Stage6
{
  Dimensions 6. 6. 31. m
  PropertyString Material AIR
  PropertyDouble G4StepMax 1.0 mm
  Module BeamLine/BeamLine.dat
  {
    Position 0. 0. -10.283 m
    Rotation 0. 0. 0. degree
  }
  Module Tracker/TrackerSolenoid0.dat
  {
    Position 0. 0. -4.783 m
    Rotation 0. 0. 0. degree
  }
  Module AFC/AbsorberFocusCoil.dat
  {
    Position 0. 0. -2.75 m
    Rotation 0. 0. 0. degree
  }
  Module RFCC/RFCouplingCoilUp.dat
  {
    Position 0. 0. -1.375 m
    Rotation 0. 0. 0. degree
    ScaleFactor -1
  }
  Module AFC/AbsorberFocusCoil.dat
  {
    Position 0. 0. 0. m
    Rotation 0. 0. 0. degree
    ScaleFactor -1
  }
```

Figure 4.1: Example of MICE module configuration file.

```
Module TOF1HorizontalSlab6Sci
{
  Volume Box
  Dimensions 42.0 6.0 2.5 cm
  PropertyString SensitiveDetector TOF
  PropertyString Material POLYSTYRENE
  PropertyDouble GreenColour 1.0
  PropertyDouble RedColour 1.0
}
```

Figure 4.2: Example of GEANT implementation of a TOF scintillator slab.

as a circle. In reality this is a cross shaped aperture. The particles following a trajectory which, in reality will see them scattered or even absorbed, in the simulation will pass unaffected. Figure 4.3 shows the cooling channel

from MICE that is made up of some very complex shapes. It can be seen in the Figure that there are only basic cylindrical shapes making up the cooling channel in this instance. The scattered yellow lines show the resultant particles that have interacted with material earlier in the simulation and have not been transmitted to the cooling channel.

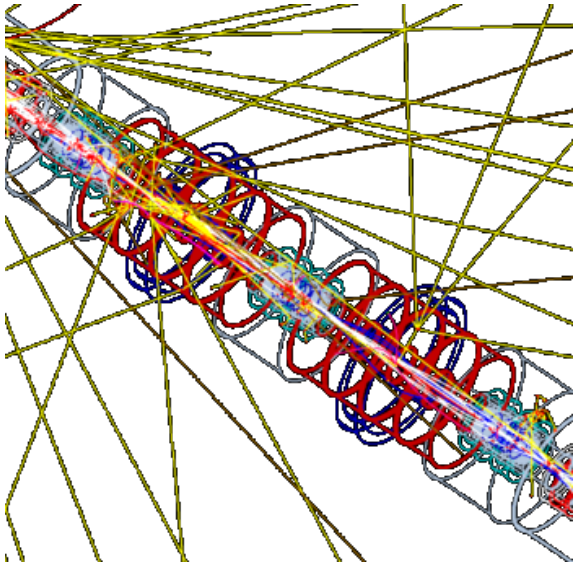

Figure 4.3: Simulation of the cooling channel taken from G4MICE legacy models.

The proposed Steps of the experiment increase in complexity where beam line elements will become more sophisticated; an effective management system of the geometry was clearly needed. A series of geometrical models was required, each model should have a version number that reflect either minor or major changes to reality. It was proposed that the Software Group would manage the models and perform well defined checks to confirm their validity. Balancing the detail of the models and the simulation's computing speed is a constraint considered during development. Extremely complex models impact on computing speed which would impact on MAUS's effectiveness. The geometry handling system was designed to provide the flexibility to alter the models when needed to seek the right compromise.

4.3.2 G4MICE Limitations

The initial investigation looked into the validity of the models that were packaged with G4MICE; these were assumed to be the official representation of the experiment. A requirement of the simulation is that particles can be simulated through the entire beam line. This was not a possibility in the official release of G4MICE, as a result groups were using other packages for their work. Cross checking their results across multiple packages became impractical.

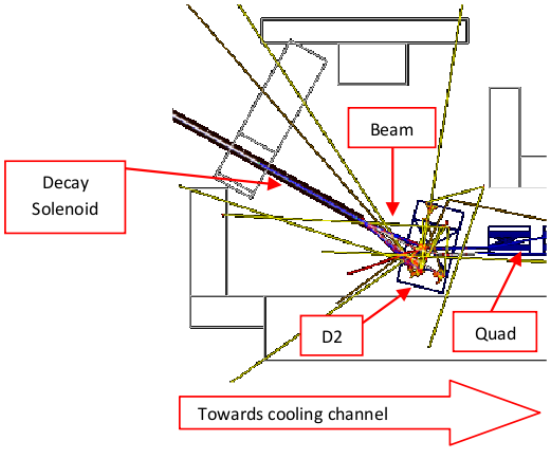

Figure 4.4: Plan View of beam simulated from the target and stopping at D2.

Figure 4.4 is a plan view image taken from G4MICE; this illustrates the simulated beam as it attempts to propagate past D2. It is clear that the particles (represented by the coloured lines that are mainly yellow going in all directions) interact with the wall of D2 and do not continue towards the cooling channel. It is expected that a collection of these lines would be directed from left to right through the labelled Quadrupole (Quad). Technical drawings were used in an attempt to produce a set of MICE modules that accurately reflected reality. It was thought that the recreation of the beam line elements from these drawings would result in the beam behaving as expected. This proved very difficult and was indicative of the underlying problems with the construction of the model. The geometry may not have been the

only contributing factor to this problem but it was the simplest to address. Other potential factors were: the physics model used to simulate the beam's propagation and errors in the simulated magnetic fields. The move to MAUS meant that improvement could be made in all areas. The new software package meant a new and effective management and control system could be put in place. Utilising new technologies and organising developers in a way based on industry practices formed the basis of MAUS. The new software and its management created an opportunity to design, develop and implement a new geometry handling system that would decouple developers from users and create a version controlled way of producing validated geometries.

4.4 Design of the MAUS Geometry Handling System

The design of the geometry handling system had to take into account a number of things. Firstly the software group had to find a method of increasing the accuracy and detail of the geometrical models. Secondly, it needed to integrate with the new structure of MAUS. Thirdly, the system had to be designed to allow the models to be versioned and validated. User interaction with the system had to be anticipated in order to build reasonable use cases to begin the design process. Considering these points a full design process was used to create the model for the system. This process began by investigating the possible use cases of the users of the software. The users of the software consist of physicists, software developers, and engineers. Each group have different requirements and will interact with the software in different manners. Discussions within the software group were then conducted that sought a way to incorporate the proposed geometry handling system into MAUS. A number of software packages were already in place and being used by MAUS; including these in the proposed geometry handling system seemed prudent. A set of use cases were then produced to illustrate how the system would operate and how users would interact with it. The use cases formed the basis of how the geometry handling system should be built and

integrated into MAUS.

4.4.1 Increasing Geometry Accuracy

The MICE project is in a constant state of change where new components are being installed in the experiment on a regular basis. MICE engineers are responsible for the installations and as such must produce Computer Aided Design (CAD) drawings of all beam line components that are collated into a single drawing. This represents the experiment in its entirety and provides a huge amount of detail. The drawing is also updated each time a new survey is taken. Surveys are conducted with every significant change made within the experiment hall. As these drawings are maintained and versioned by the MICE engineers it was sensible to find a solution that used the CAD drawings and the engineers' technical expertise for the modelling. CAD packages are easy to use and allow the creation of accurate models which can be altered quickly and efficiently.

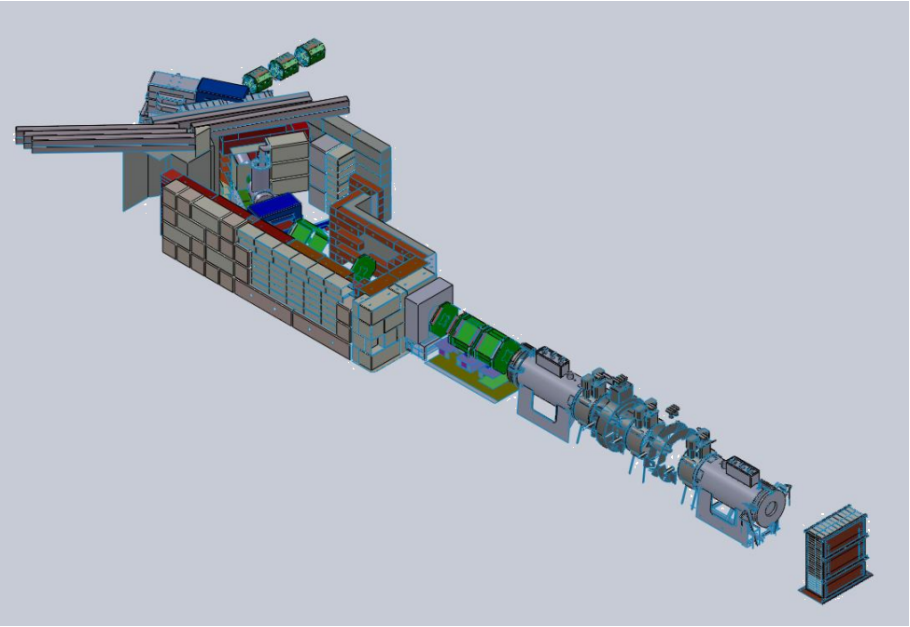

Figure 4.5: CAD Model of the entire MICE beam line.

One of the main advantages of using CAD is that the level of detail of

the model can be quickly and easily varied, without altering the underlying description. The level of detail in Figure 4.5 that the package outputs is far more than is needed for MAUS. Another advantage of using CAD modelling is the ability to produce simple technical drawings from the model. These drawings can show the dimensions of anything in the model and will prove to be very useful for the version control of the model and disseminating the information regarding component's position to the MICE collaboration.

The initial investigation found that G4, the base platform for MAUS, can build geometry models from a translated form of CAD. This translated form is known as Geometry Description Markup Language (GDML) [48]. G4 can import and model components from GDML files. Unfortunately the GDML files cannot be directly imported into MAUS for a number of reasons. Firstly, much of the core G4MICE code was transferred to MAUS. Rewriting the core code for MAUS to read GDML rather than MICE Modules was judged to require too much time, however this does remain a future possibility. The schema used to define GDML does not include all the information required by MAUS. A software called FastRad was found that could transform CAD models into GDML, and the decision to use this was taken. GDML being of eXtensible Markup Language (XML) form meant that eXtensible Stylesheet Language Translation (XSLT) files could be used to convert them into MICE Modules [49]. An extension of the GDML schema was created that allowed extra information specific to MAUS to be added during the conversion. Initial discussion with the engineers resulted in an agreement that when new CAD models are produced a new set of GDML files would also be produced; these would then be passed to the software group in order to process these into MICE Modules. Version control and making these models available to the collaboration was also to be included in this process.

By translating the CAD model into GDML form, the accuracy of the model improved. The level of detail in the model presented by the CAD package was chosen by the software group in order to find a compromise between model detail and simulation speed, this is stored by the engineering team in a CAD model that is specifically for MAUS. CAD packages are also much more user friendly than previous model creation methods used in

MICE. This allows new, accurate models to be created with a much higher standard, much more quickly than if they were created by hand.

4.4.2 Existing MAUS Components

As part of the re-structure of the MICE software an online database was created, known as the Configuration Database (CDB) [50]. The CDB serves the purpose of being a central online store of information. Initially this database stored run information gathered directly from the control room during running periods. Run information includes all magnet currents and settings, the aim of the run and its beam line settings. Calibration data and electronic cabling information is also stored in the CDB and can be accessed via an Application Program Interface (API) written in Python that is included in MAUS. The CDB stores its information in XML format, meaning that any geometrical information could be stored on the CDB along with the previous detailed information. MAUS, therefore, had a way to store CAD translated models in such a way that they could be date stamped. This provides the ability to version the geometries and to maintain a central store of models.

4.4.3 User Interaction

After the initial stage of design, which included speaking to all concerned parties and discovering their needs, a more formal implementation of the system requirements was produced. This involved creating use case scenarios that would help structure the code. The six use case scenarios that were developed were as follows:

First Use Case

The user would like to download the current valid version of the geometry.

Second Use Case

The user would like to download a version of the geometry that was valid for a specific period of time.

Third Use Case

The user would like to download all the information associated with a particular run number. The valid geometry for that period of time should be downloaded along with all the run configuration information.

For each of these use cases there are two different ways in which it was envisaged users would interact with the system. For design purposes these users were split into two groups: basic users and advanced users.

Basic User Interaction

A basic user will only need to run simulations, this means that they only need to select a *current, time or run number* geometry. The geometry handling system should therefore automatically download the correct version for use in the simulation. The user does not need to receive a local copy of the geometry.

Advanced User Interaction

An advanced user is someone who wants to make modifications to the beam line geometry. This requires access to the MICE Module files. For this use case the system will download a local copy of the geometry where the user can save and alter the geometry as they please. They will not, however, have access to the CDB to store their altered configuration as this only contains official geometries. The local copy can then be used for simulation instead of the official copy stored in the CDB.

There is potential for a seventh use case that is touched upon in the Advanced User Interaction case. This is when a user has created a specific geometry that they wish to keep. They may wish to store their local modified copy of the geometry for future reference or as evidence to support a publication. It had been decided that the CDB should only be a store of official geometries. As the local modified copy is not an official version of the geometry it should not be stored on the CDB. To create a separate store for these types of geometries would involve creating a separate CDB store. This use case was, after some discussion, dropped for the time being as it would

mean much more effort creating CDB compartments for different geometries and could prove to be unmanageable. It may be added at a later date if the need arises.

4.4.4 Final Design Choices

The final choices for the design of the system were based on the processes described up to this point. Firstly, the MICE engineers would create a CAD model for use in MAUS and translate this into GDML files. These files are then collated and stored on the CDB with a description of the geometry, a period of time for which the geometry is valid, and the time and date it was uploaded. An executable file enables users to download a geometry of their choice. The choices are either the current valid geometry, the geometry that was valid at a user defined time or the geometry that is valid for a particular run. If a particular run number was specified, the handling system downloads the specific run configuration parameters along with the geometry. This provides the magnet currents as they were during the run, as well as the geometry. This functionality is provided by a series of python modules that comprise the geometry handling system.

4.5 Implementation

The implementation of the geometry handling system required a number of different technologies. Python classes were created to handle the different aspects of uploading and downloading. This code made use of some non-standard Python libraries to interact with different parts of the overall proposed architecture. The GDML was customised to suit the system's needs, which proved to be easy to do because XML is designed to be extensible i.e. users can expand an XML schema to match their requirements. In the case of the geometry handling system it was extended to include run time information. Finally, XSLT were used to translate the GDML files into MICE Modules, the format required by MAUS.

4.5.1 GDML Schema

Part of the drive to design a new system was to decouple the geometry models from users. This means that the handling system needs to be stand alone; users can simply download a geometry model and all the information required to run the simulation. To do this, the GDML schema had to be extended to include MICE-specific information that does not exist in the original GDML schema. The schema of any set of XML or GDML files can be considered as the rules that the files format must adhere to. The rules govern how the information in the files is stored and managed. If data is added in a way that breaks the schema it is deemed to be an invalid XML form. The MICE specific information that extends the GDML schema is as follows:

Run Configuration Information
: This is the information gathered in the control room

G4 Field Information
: This is the information required by G4 to build magnetic fields.

Environment Variables
: These are the environment variables that direct MAUS code to local directories. This information cannot be gathered by GDML or XSLT as these languages have little functionality. The information is needed for the running of the simulation within MAUS because local path names are needed in the Python modules that handle the geometry downloads, the path names are specified in the GDML schema.

These points are currently the only schema extensions but future requirements can be incorporated with ease. The implementation of the extension involved creating a new schema called *GDML_MICE.xsd* that forms part of the geometry handling system.

The MICE schema is then included in the existing GDML schema, which then allows the MICE specific elements to be added to the CAD translated geometry without invalidating it. The two schemas are merged together during the download process. Figure 4.6 is an example of the definition of the parent elements within the GDML_MICE schema.

```
<!--++++++++++++++++++++++++++++++++++TOP TYPES++++++++++++++++++++++++++++++++++++++++++-->
    <xs:element name="MICE_Information">
        <xs:annotation>
            <xs:documentation>
                This Information is needed for the MICE experiment. It is
                translated through the CAD to Software translation system
                and is need for simulations. Some of this information comes
                direct from the control room and some is stored in MAUS
                and combined with geometrical information from CADs.
            </xs:documentation>
        </xs:annotation>
        <xs:complexType>
            <xs:sequence>
                <xs:element name="Configuration_Information" type="configurationType" minOccurs="0">
                </xs:element>
                <xs:element name="G4Field_Information" type="G4Field_InformationType" minOccurs="0"/>
                <xs:element name="Detector_Information" type="Detector_InformationType" minOccurs="0"/>
                <xs:element name="Other_Information" type="Other_InfromationType" minOccurs="0"/>
            </xs:sequence>
        </xs:complexType>
    </xs:element>
</xs:schema>
```

Figure 4.6: Parent elements from the MICE schema.

This schema allows MICE-specific GDML elements such as those in Figure 4.7 to be included in the geometry description. When the GDML is validated against the schema it will not throw an exception because the MICE extension has been designed to be optional. This allows the GDML files to describe either geometry only or geometry and MICE specific information together.

It must be noted that Figure 4.7 is only an example of the elements that can be incorporated into the existing GDML. The schema has been designed to allow multiple fields i.e. more than one set of quadrupole settings, as well as configuration settings direct from the control room and additional detector information. The extension of the GDML schema was defined and written by the author.

4.5.2 Module Transformations

After MICE specific data was merged within the GDML files a method of translating these files into MICE Modules was required. This was done using XSLT. XSLT is a stylesheet that searches the nodes and elements of XML and rearranges them in a layout that has been specified in the stylesheet. It can also include some logic to only write certain predefined terms for specific

```
<Configuration_Information>
</Configuration_Information>
<G4Field_Information>
    <Dipole>
        <FieldName name="D1"/>
        <Position x="0" y="0" z="0"/>
        <Rotation x="0" y="0" z="0"/>
        <Volume name="None"/>
        <FieldType name="MagneticFieldMap"/>
        <FieldMapMode name="Read"/>
        <FileType name="g4bl3dGrid"/>
        <FileName name="\${MAUS_ROOT_DIR}/src/legacy/FILES/Models/Modules/BeamLine/B1_6inch.table"/>
        <Symmetry name="Dipole"/>
    </Dipole>
    <Quadrupole>
        <FieldName name="Q1"/>
        <Position x="0" y="0" z="0"/>
        <Rotation x="0" y="0" z="0"/>
        <Volume name="None"/>
        <FieldType name="Multipole"/>
        <Dimensions height="0.5" width="0.5" length="2.0" units="m"/>
        <FieldStrength Value="1" units="T/M"/>
        <Pole Value="2"/>
        <MaxEndPole Value="4"/>
        <EndFieldType name="Tanh"/>
        <EndLength Value="0.12528" units="m"/>
        <CentreLength Value="0.330899" units="m"/>
    </Quadrupole>
    <G4Magnet_info File_Location="/home/QCFieldMap.txt" Name="Quad 1 to 3" Type="QC"/>
</G4Field_Information>
</MICE_Information>
```

Figure 4.7: Example of GDML field elements.

cases. To create MICE Modules two stylesheets were created: One translates the parent configuration file and the second translates its children. Figure 4.8 shows an example of the parent files stylesheet.

```
<xsl:output method="text"/>
<xsl:template match="gdml">
    <html>
        <head>
            <title>Configuration <xsl:value-of select="structure/volume/@name"/>
                {
                Dimensions <xsl:if test="solids/sphere/@name='WorldSphereRef'">15000.0 10000.0 50000.0 mm</xsl:if>
                PropertyString Material <xsl:if test="structure/volume/materialref/@ref = 'Vacuum'">AIR</xsl:if>
            </title>
        </head>
```

Figure 4.8: Example of parent stylesheet.

This stylesheet takes the GDML and translates it into a MICE Module. An example GDML file is shown in Figure 4.9. All stylesheets were built specifically for the Geometry Handling system. The resulting MICE Module text file produced by the XSLT can be seen in Figure 4.10.

```
<solids>
    <sphere name="WorldSphereRef" rmin="0." rmax="12413.3291" startphi="0.0000" deltaphi="6.2832" starttheta="0.0000" deltatheta="3.1416"/>
</solids>

<structure>

    <volume name="Structure_261049064">
        <materialref ref="Vacuum"/>
        <solidref ref="WorldSphereRef"/>

        <physvol>
            <file name="TDm1152m9348.gdml"/>
            <position name="posRef_1" x="114.2233" y="-174.5097" z="-426.2872"/>
            <rotationref ref="identity"/>
        </physvol>
```

Figure 4.9: Example of GDML.

```
Configuration Structure_261049064
                        {
                            Dimensions 15000.0 10000.0 50000.0 mm
                            PropertyString Material AIR
                            PropertyDouble G4StepMax 5.0 mm
```

Figure 4.10: Example of XSLT translated MICE module.

4.5.3 Detector Implementation

During the design process it was concluded that direct translation of the CAD models of the individual detector components would result in an unnecessarily high level of detail in the resulting geometry. If they were to be translated in this manner the responsibility to maintain these models would fall upon the software group. Each detector is unique and modelling them requires further interaction with G4 in terms of how particle hits are digitised and presented in the data. It was therefore decided that the CAD Models should only be used to provide detector position information within the world geometry. The model of each detector then remains the responsibility of the appropriate detector group. This works well because each group has the expertise to model the complex components of the detector and how they interact with G4 within MAUS. Initially, the legacy models taken from G4MICE are being placed in the correct positions in the CAD model. However, the intention is to update the models and re-write the GDML schema to include the individual detector components. The detector components include the positions of the 'sensitive volumes' of the detectors. What is

meant by 'sensitive volumes' is a volume created using G4 base volumes such as boxes and spheres that react to particles. When a particle travels through a sensitive volumes within the simulation, the energy deposited within the material is recorded. This recorded data is then digitised through a number of parameters to represent values that the real detector would produce in response to that event. The Tracker group produced the first schema out of the different detector groups; they produced a set of GDML files describing the Tracker. An XSLT script was produced that translated the GDML files into the MICE module files needed to model and simulate the Tracker. The GDML file was stored with the other CAD GDML files and the Tracker model will be placed in its correct location within the world volume upon download of the geometrical model.

4.5.4 Python Code

Python is the main language chosen to write the Geometry Handling System. This language was chosen by the software group for its strength in scripting. The core code used by the Geometry Handling System is for uploading and downloading the geometries. The core code contains functionality, in the form of executable files, that enables the user to query the CDB. More information on how to use these files and also technical information about the Python classes can be found in the MAUS user guide [51]. The three programs that constitute the core code are summarised below:

upload_geometry.py

This program collates all the GDML files produced by the engineers into a single file. This is then zipped and uploaded to the CDB. The information required for the separation of the GDML files once they are downloaded is included as part of the collation process. The compressed file is uploaded along with a note explaining what the geometry represents, the time period in which it was valid and also the date and time of the upload.

download_geometry.py

This program downloads the compressed file and separates it into the individual GDML files; these are then placed into the location specified by the user. Local directory paths and information required for simulation are then added to the files. This includes the location of the GDML schema and the material files that are associated with the GDML files. The materials file is produced with the GDML files by the engineers; this specifies all of the materials that are used within the models. After the GDML files have been formatted correctly they are then translated, using the XSLT sheets, into the MICE modules necessary for simulation. The user will be able to download a geometry that is either: a current valid model of a certain time period, or a model of a specific run.

get_geometry_ids.py

This program queries the CDB about the geometries stored there. It prints the information associated with each geometry to screen or to file, allowing users to identify the geometrical models that they require.

These programs are designed to be used by MAUS users, with the exception of the upload program which is for developers only. This is to ensure only official geometries are uploaded to the CDB. The main store for geometries on the CDB only has write access from one machine based in the MICE control room, this adds more security and control for the MAUS development team.

The programs have been designed to behave in this manner to accommodate the requirements that were produced during the design process. They also account for the existing technologies of the MAUS framework and other external tools used for MICE.

4.6 Geometry Handling System

The new handling system provides greater control over the geometry models that are used in MAUS. The overall system has been designed to follow a simple flow from CAD drawings to users. The responsibility of each detector

model will be that of the corresponding detector group. Once the model is complete and the detector group have modelled the necessary sensitive volumes, volumes that interact with particles and provide particle data as hits, the model will be passed to the software group. The software group will then place the detector model in the correct position relative to the MICE beam line. A geometry release system has been created that incorporates a pre-release that allows detector groups time to de-bug their models. After this period is over, the geometry is officially released to all MAUS users. Figure 4.11 depicts an information flow diagram for the geometry handling system.

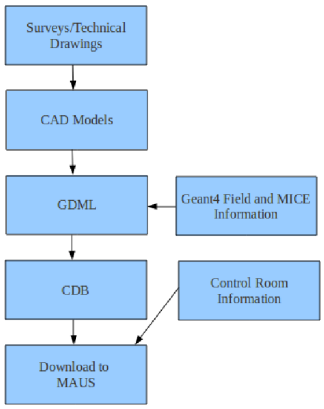

Figure 4.11: Flow diagram of information within the Geometry Handling System.

4.6.1 Component Improvement

One of the advantages of the new system is the greater level of detail of each component. CAD models can produce a geometry that could not be created by hand using MICE Modules.

Figure 4.12 is a technical drawing of a quadrupole and it can be seen that the drawing contains a vast amount of detail. This is, in fact, too much detail for the simulation as only large metallic components close to the beam line will have any significant effect on the beam. To begin with only material

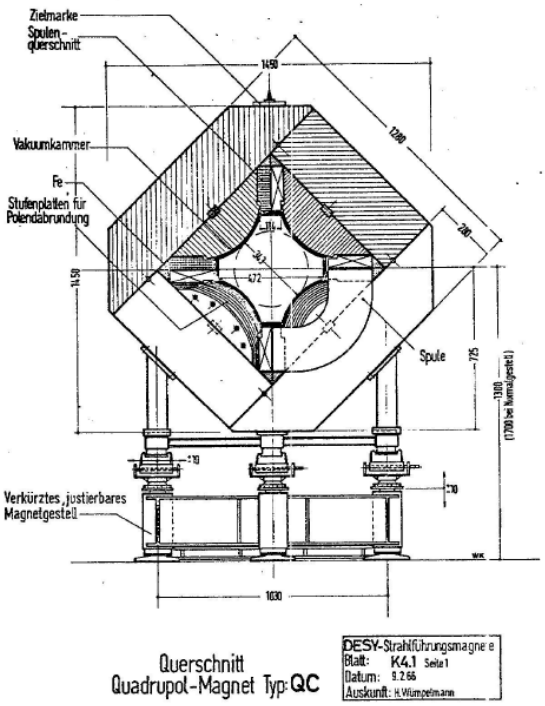

Figure 4.12: Technical drawing detailing the dimensions of a MICE quadrupole.

within a 1 m radius of the beam was included in the MAUS CAD model. An investigation into what level of detail is sufficient to yield accurate results is required. The investigation must find a balance between computational cost and model accuracy in order to determine the best compromise for MAUS.

For comparison Figure 4.13 is an image taken from G4MICE showing a quadrupole that was written by hand. It is clear from the figure that this method of modelling does not contain very much detail compared to the technical drawing in Figure 4.12. It must be noted that the technical drawing represents the real quadrupole as this was one of the drawings used during the quadrupole's refurbishment and has been verified by the engineering team. A simple box volume to represent such a complicated component does not reflect reality. The original model has missing material. Particles in the experiment would interact with this material; not modelling this will alter

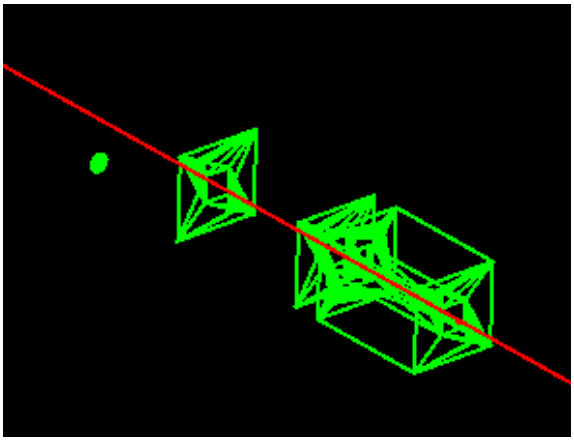

Figure 4.13: G4MICE quadrupole model.

the characteristics of the beam and conclusions drawn from the Monte Carlo simulation will not represent reality. Comparisons between the experiment and the Monte Carlo simulation will be suspect. Considering the tolerances required for the emittance measurement, which is the primary focus of MICE, this problem must be addressed. The CAD transferred model yields much a more realistic representation of the quadrupole, seen in Figure 4.14.

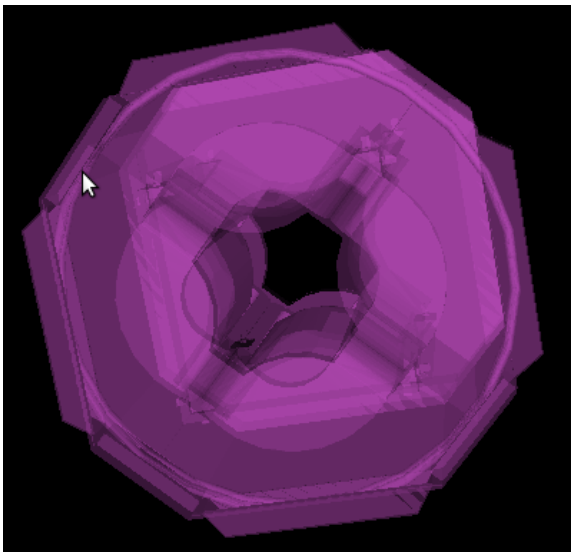

Figure 4.14: CAD transferred MAUS quadrupole model.

As CAD is much more user friendly, in terms of physically representing and actively modifying the models, the level of detail can be altered according to user and developer requirements. The new system is currently live and users are allowed to download the first geometry model. This model has been transferred from a CAD model that has been tailored to include information specified by the MAUS development team.

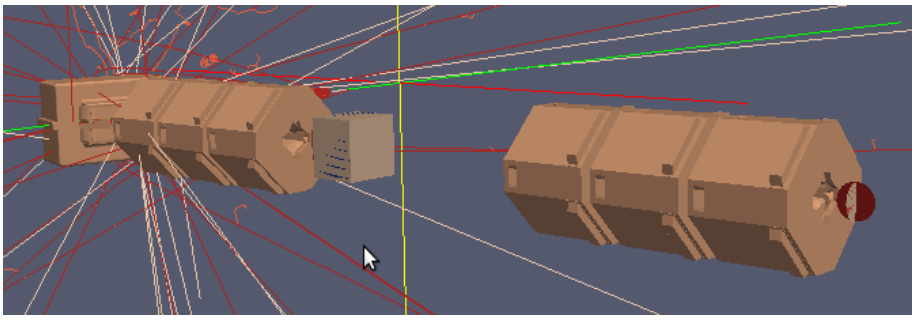

Figure 4.15: Simulation of MICE hall that has been downloaded from the CDB.

Figure 4.15 shows this first geometry model of the current MICE hall. As the work to model each of the detectors is still to be carried out, this model does not contain these yet. The purpose of showing the Figure is to illustrate a simulated model that has gone through the process of uploading to the CDB and then download and finally simulation. This represents the initial version of the handling software. Figure 4.15 has within the model various magnets and the coloured lines that can be seen are particles. Currently MAUS simulates the path of every particle regardless of its direction.

The functionality to stop tracking a particle, when its trajectory takes it beyond a certain distance away from the beam centre, has not yet been implemented. The particles seen in the Figure are moving away from the beam line because they have interacted with a solid material. It is expected that as the experiment grows this model will change. The geometry handling system will continue to improve. The initial proof of feasibility that a system of this design can work, and be integrated with the other systems and technologies already in use, is complete.

4.7 Geometry Validation

In order to validate the geometry handling system within MAUS the new system must be compared with the old system. To do this comparisons were made between the models created by hand, used in G4MICE, and those created by CAD. The MAUS model, when compared to the engineering drawing of the quadrupole, is a better representation than its predecessor. The method used to create this model took less time than creating the model by hand.

The geometry handling system has been designed to enable flexibility and greater accuracy of the models being created for simulation. It has also been designed to properly manage the geometries produced. The geometrical models used in the construction of the system are by no means final but have been used in order to investigate the systems performance so that it can be compared to its predecessor. The investigation conducted by the author included:

- A simulation of the magnetic fields that are initially to be used within MAUS. This is to ensure that the field maps model theory. Further investigation is needed to determine if the fields represent the fields seen in reality.

- Simulating a beam that starts before D2 and travels through the magnet, which was not possible in G4MICE.

- Determining whether simulated particles reach the cooling channel and interact with the sensitive volumes to produce hits.

- Producing emittance vs beam axis plots to examine whether emittance is being reduced as expected, giving insight into the overall geometrical model and where future improvements can be made.

- Evaluating the speed of simulation of the model as the beam moves through the geometry; this also gives an insight into the model and where improvements can be made, as well as the overall geometry handling system.

The investigation that has been outlined was performed during the development of the Geometry Handling System. The purpose was to ensure that the work presented has improved the way geometry is modelled with respect to G4MICE. Further work will be needed to move the Geometry Handling System to improve areas of management and control for the users of MAUS. This will be outlined in the conclusion of this chapter.

4.7.1 Magnetic Field Validation

The magnetic fields of the beam line are not included in the CAD models as these only deal with the physical objects in the experiment. The magnetic fields therefore need to be placed in the correct position in the world volume. The fields can either be generated by G4 or read in via a 3D field map. In order to generate a field using G4 the user must specify the position of the centre of the field, the field type i.e. quadrupole/dipole and the field's strength in tesla. G4 will produce an idealised magnetic field for that region. Other parameters are available to tailor the field to the users needs. A 3D field map measured from the real experiment is the desired approach to field simulation as this will be a real representation, but not all magnets have been mapped as of yet. MAUS uses a 3D field map to create the dipole fields; all other fields are generated by G4. It must be noted that similar to G4 generated fields, mapped fields can also have their absolute strength altered to represent magnets with different currents in the simulation. MAUS has a utility that allows the user to print the magnetic field strength at specific positions. The utility was used to investigate the magnetic fields within the model. The planes cut through the field at certain positions along the magnets in the direction of particle motion. Figure 4.16 shows the field map, inside the magnet, at $z = 600$ mm from the face of the dipole. The z position, 600 mm, was selected because it is the approximate centre line of the dipole. The plane represents the view into the aperture of the dipole. Figure 4.16 is the field map of a simulated dipole with an arbitrary field strength taken from MAUS. Although there is work to do in order to improve the fields within the magnets, this initial simulation shows large discrepancies in the

structure of the field.

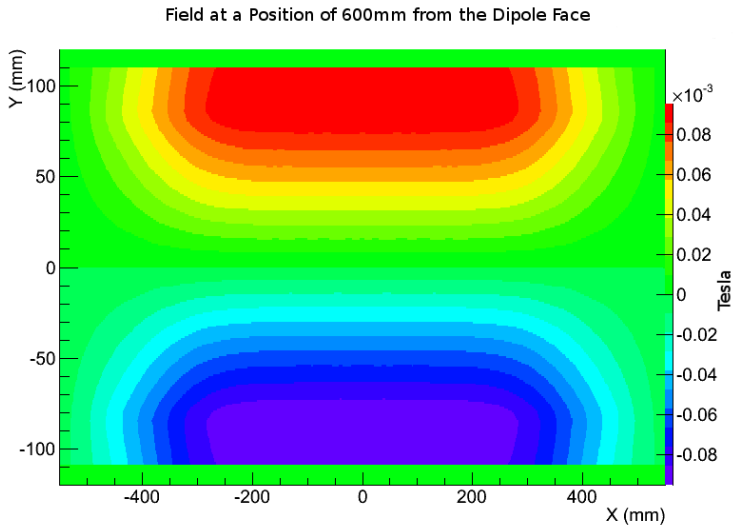

Figure 4.16: Simulated field map of dipole at 600 mm from the dipole's face. This represents the field B_z which is expected to be 0 in the centre of the magnet.

The same procedure was conducted with the quadrupole magnet. Figure 4.17 shows the field produced by MAUS which again shows the expected structure.

The fields simulated within MAUS are positioned with their centre points upon the geometrical centre points of the magnets in the experiment. The positions of the magnets, relative to the overall experiment, were taken from surveys provided by the engineering team. Once complete the model of MICE will have all the magnets, with their respective fields, in the correct positions.

4.7.2 Model Validation

Validation of the model can be done in two ways. The first is by comparing the technical drawings, such as that in Figure 4.12 with the corresponding model produced by MAUS Figure 4.14. Some images have already been shown that illustrate the accuracy of the MAUS models. The second way is to validate the overall model of the experiment via producing data. G4MICE

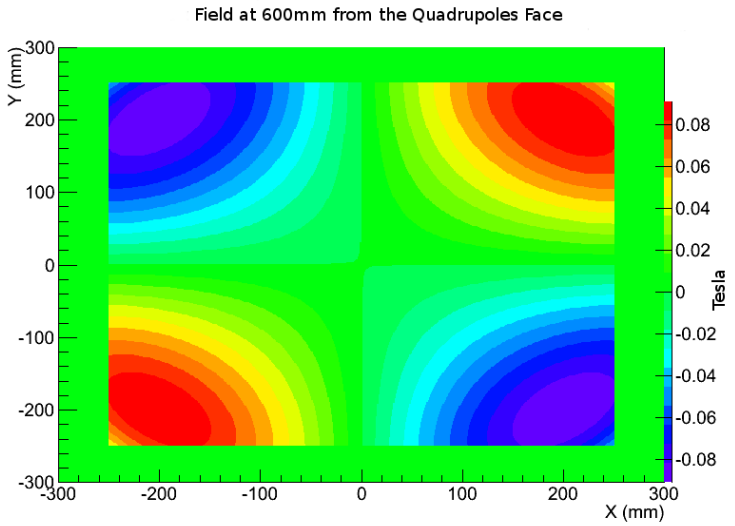

Figure 4.17: Simulated field map of quadrupole at 600 mm from the face. This represents the field B_z which is expected to be 0 in the centre of the magnet.

could not simulate a beam, the particles would strike the wall of D2 and the beam would be scattered at this point. To validate the model two simulations were carried out with MAUS. First, a seeded beam whose profile has been provided by another package was positioned just before D2 as if the beam has come from the Decay Solenoid. A seeded beam is used instead of a MAUS simulated beam starting from the target because the seeded beam gives a more accurate profile. MAUS cannot yet produce a beam with a realistic profile at the exit to the decay solenoid. The purpose of this simulation is to examine whether the beam moves through D2 and propagates through the next quadrupole triplet and towards the cooling channel. The second simulation will use a greater number of seeded particles and will investigate the initial transmission ratio of particles starting before D2 and reaching the positions where the trackers will be placed within an area of a quadruple aperture. The combination of these simulations will show that MAUS can simulate past D2 where G4MICE could not and that particles reach the cooling channel.

The initial simulation consisted of only the magnets and their fields, no

detector elements were included. The simulation used to seed the beam into this model of MAUS simulated particles generated at the target and propagating through the initial magnets. Care was taken to place the beam's starting position in such a place as not to have the fringe fields of the decay solenoid and D2 affect the particles. If the starting position were to be placed in the fringe area of either of the beam line elements this may have undesired effects upon the beam. The desire is to have as many particles as possible enter D2 in order to observe how many will travel through D2 and the following quadrupoles. 4000 particles were seeded and a transmission ratio of those that reached the end of the model was determined. Three virtual planes were placed in the model which gave the number of particles passing through them. Virtual planes are not physical objects within the model and do not interact with particles; they are used purely for analysis. They were placed as follows: one before each quadruple triplet and a third at the end of the model. For this simulation the x and y positions of all particles crossing the virtual planes in an area of 500×500 mm centred on the beam axis was recorded. This area is the size of the magnets' aperture and therefore allows the number of particles within the beam to be determined. The currents of the magnets will also have an affect on the number of particles that are directed down the beam line and tuning the currents for maximum transmission can be done. For this simulation the magnet currents have not been tuned. The number of particles is not a priority as long as particles do reach the end of the model; if this is the case then this model will have surpassed G4MICE's model where particles did not travel past D2. Figure 4.18, 4.19 and 4.20 show the positions of particles crossing each of the virtual planes.

This simulation provides information relating to the transmission of particles but can also give an indication of the simulation speed of a model with this level of detail.

Figure 4.20 shows that 151 particles from the initial 4000 lie within the approximate aperture's area after the beam has passed through the series of magnets. This equates to a transmission rate of 3.8%. This demonstrates that the new model will allow particles to be transported past D2 and into

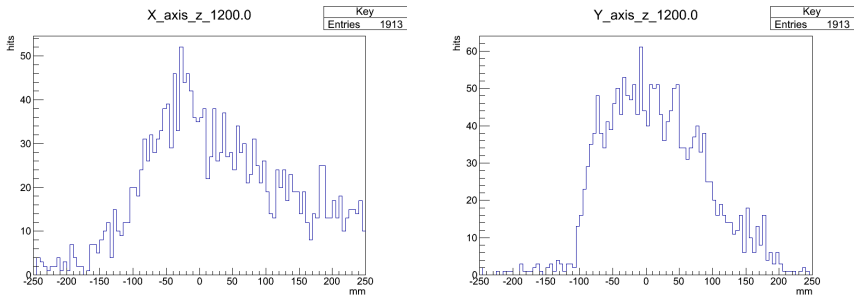

Figure 4.18: XY plots of particles before first triplet.

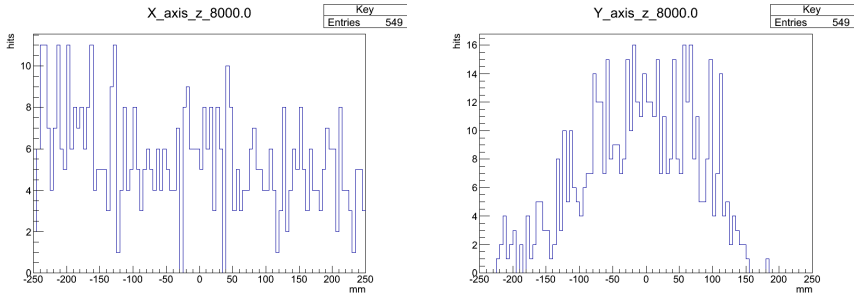

Figure 4.19: XY plots of particles before second triplet.

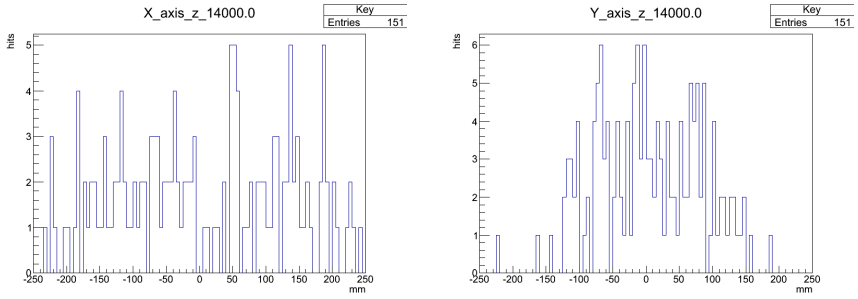

Figure 4.20: XY plots of particles after second triplet.

the cooling channel. This concludes the first simulation.

Step IV is the next stage of construction for MICE and will see the installation of two trackers and an AFC. Placing a virtual plane at the beginning of the cooling channel will give the number of particles that reach this point. Increasing the number of particles will test the speed of the simulation as well. 10,000 particles were simulated using the hybrid Step IV configuration. What is meant by a hybrid Step IV configuration is that the magnets are taken from CAD models and the cooling channel components are taken from legacy detector models. Placing the detector models into the simulation will allow data to be produced by the sensitive volumes within them. Unfortunately, at present, the detector models are still in development and do not produce hit data;, so virtual planes were used to show particles entering the cooling channel. The detector models will be removed from this simulation and the virtual planes will be used to detect the particles.

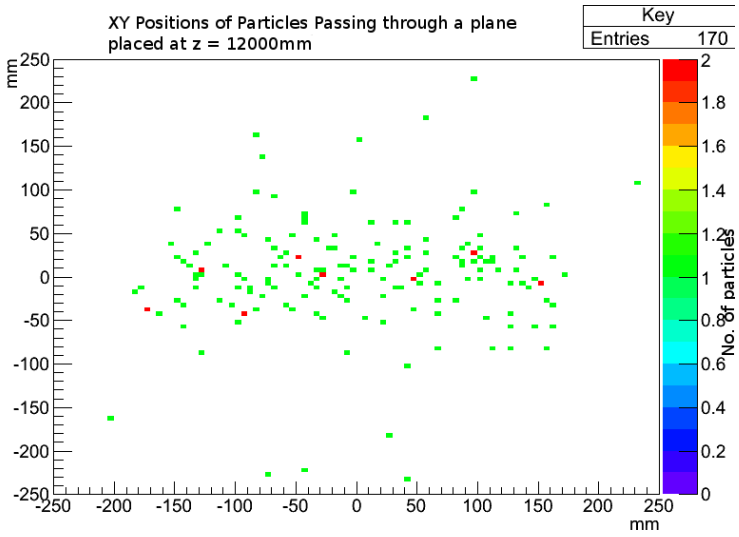

Figure 4.21: XY particle hit positions of the simulated beam of 10,000 particles at position $z = 12000$ mm; the z position is the beginning of the cooling channel.

Figure 4.21 shows the positions of the particles that enter the cooling channel. Using the 10,000 particle sample it can be seen that 170 particles reached the beginning of the cooling channel, $z = 12000$ mm, and that they

focus around the centre point of the beam axis. The z axis in this simulation was aligned with the beam line axis. The particles reaching the beginning of the cooling channel focussed upon the beam line axis is what was expected. As the model is refined and improved, along with improvements to MAUS as a whole, it is expected that the number of particles reaching this point will increase to match the real experiment. This is a good test that shows the model is behaving as expected in the transportation of particles along the beam line. This was not achieved with G4MICE.

The purpose of the simulations undertaken in this section were to provide a comparison between MAUS and G4MICE. The simulations have proven the ease of creating new geometrical models and also tested the new handling system by uploading the initial model and then downloading it. The simulation used the downloaded model and showed that the model does not have the same problems that the previous G4MICE model had. The simulations performed here show the first stage of an iterative process. These are by no means the finished article and improvements will be made in the future. A future study is needed to make a more detailed study of transmission rates and beam profiles at different momenta and emittances.

4.7.3 Speed Evaluation

One of the disadvantages of increasing the accuracy of the model used for simulation is the impact on computational speed. G4 operates by producing values for a number of parameters for every particle, such as position, velocity, direction and momentum, every time the particle in question moves to its next step which is a length that can be defined. The step size changes dependant of the particle's position in space, and when close to a boundary this step size decreases. The CAD model translation increases the complexity of the models, resulting in an increase in the number of calculations that are carried out. The speed of the simulation is quantified by the computational time taken for the overall simulation divided by the number of particles it is simulating, giving the time taken per particle. The goal for simulation time is 0.1 sec/particle which has been specified by the software group. This is

an initial target and may be reviewed at a later date. The expected speed of this model is 1 sec/particle. Improvements to both the physics engine used by MAUS and the geometrical models can be made in the future to decrease simulation times. The MAUS simulation of the hybrid Step IV configuration gave the first indication of the speed. The linux 'time' function recorded the time taken by the simulation. It was carried out on a Samsung R540 laptop which has a 2.4 GHz Intel Core i3 processor and 4 GB of RAM. The first time is a simulation of 10,000 particles simulated all at once and the second is 10 separate instances of 1,000 particles simulated one instance after another. No other background programs were running during these simulations. The CPU time taken to simulate the single simulation of 10,000 particles was 2.8 seconds/particle whilst the 10 instances of 1,000 particles yielded a time of 2.8 seconds/particle as well. For the purpose of acquiring a time per particle value the 'user' and 'sys' values from the 'time' command were used, as they represent the time taken from the beginning of the function call to the end of computation. The measured time exceeds the initial expectations of the system which was a simulation speed of 1 second/particle. What can be taken from this simulation is that a large number of particles can be simulated with CAD models that have been acquired from the CDB.

There are a number of improvements that can be made in order to increase the simulation speed. Internal computational mechanisms can be optimised, such as stopping the simulation of particles that fall outside the beam line or particles that strike walls that are not of interest. There is another potential way to speed up the simulation related to the internal working of G4. The CAD models are constructed using a number of tessellated triangular facets in G4. A warning has been observed when the MAUS simulation is running; it is that a particular particle is unsure whether it is inside or outside of a volume. Initial investigations show that this is due to the tessellated make up of volumes within MAUS and that this is a problem with G4 and not MAUS. The observation of this error indicates that this particular function is being called iteratively during the simulation and yields a considerable number of warnings to be printed in the simulation's logs. This problem is being investigated, but so far a solution has not been found. Another way

to improve the speed is to reduce the level of detail that is included in each beam line component. A balance must be found between the level of detail in the simulation and it's speed and this will be done in a future study.

4.7.4 Monte Carlo Simulations

The final set of investigations into the new system that were conducted aimed to prove that the simulation can be used for analysis. To prove this a simulation of the hybrid Step IV geometry was used to produce hits made by particles in the cooling channel, that were then used to calculate the emittance of the beam. The purpose of this study was to show that particles can be simulated from the beginning of the current CAD model through to the detectors and cooling elements of the beam line. The cooling elements and detectors have been taken from the legacy models and have not been translated from CAD; these models are still being constructed by the engineers.

Figure 4.22 shows the emittance vs z for the cooling channel. The figure has been produced by MAUS and shows that an emittance measurement can be made using the current geometry model. This shows that the models being used by MAUS can be used to produce emittance plots. This does show that the new system can be used in the manner it is intended.

Figure 4.22 shows the MAUS calculated emittance along the z axis or beam line of the cooling channel. The cooling channel spans the region of approx 16000 mm to 28000 mm on the z axis from the MICE centre point which is 0 mm on this axis. At position 20000 in the Figure the emittance gradually decreases; as this is where the cooling channel elements are it is reasonable to suggest that the momentum of the particles is being reduced here as they pass through the elements. The Figure displays a large peak at approx 19000 mm; within the model this is the gap between two of the beam line elements. I was unable to establish a reason for this effect. The cooling channel models being used within this simulation have been taken from legacy G4MICE models and are suspect until validated. Three promising features should be taken from this simulation; first is that the CAD translated model can be used to yield data, second is that the emittance

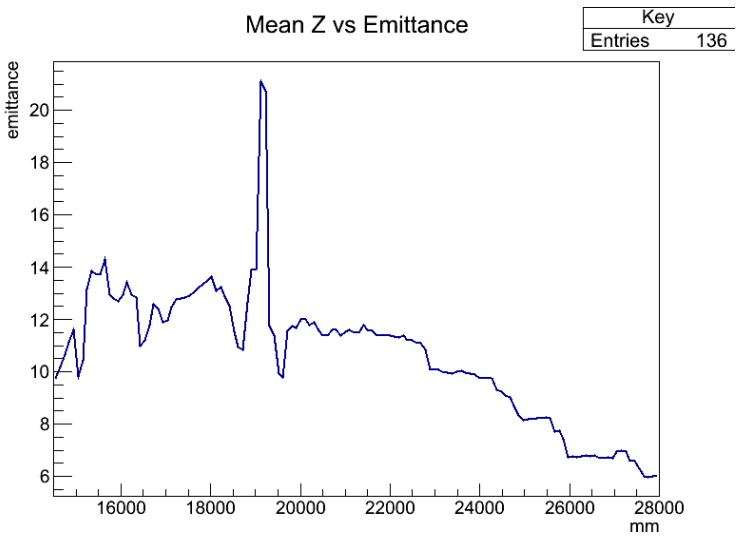

Figure 4.22: Emittance vs z for simulated Step IV.

appears to be decreasing within the cooling channel models, and third that a framework now exists to perform reliable studies. The purpose of this simulation is to show that an emittance measurement can be produced by MAUS using a model from the Geometry Handling System. This plot does have positive features but cannot be considered correct in comparison to any real measurements as there is much more work needed within the geometry and other areas of MAUS.

4.8 Conclusion

G4MICE had a system that involved including geometry models that represented the complete MICE experiment. Creating these models by hand left out a lot of detail that may or may not be important to the results produced by the simulation. It allowed anybody who used the software to create and alter the models themselves resulting in the models becoming inaccurate and uncontrolled. With the move to the new software, MAUS, the opportunity to address the accuracy and management of the models presented itself. The design of the new management system resulted in using CAD models

that were created specifically for the software group and to the group's requirements. These models are then stored in a database where users can use the models but not alter them. The system has been launched and is currently in use as part of the MAUS package. The design of the geometry handling system looked to cater for the needs of the different stake holders in the system; the software group, the engineering team and the end users of MAUS. The design aimed to make use of current systems that are in place such as the CDB and the versioned CAD drawings that are maintained by the engineering team.

The current MAUS user guide highlights the system and the various improvements made upon the work presented in this chapter. The Geometry Handling System was incorporated into MAUS and available for use during summer 2012 [52]. The overview of the Geometry Handling System, taken from the MAUS user guide, can be seen in Figure 4.23.

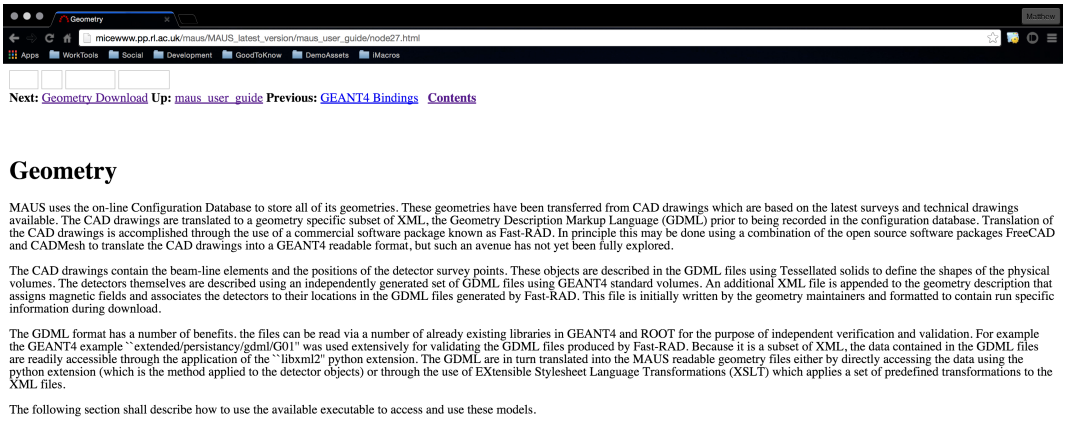

Figure 4.23: MAUS User Guide - geometry overview [51].

The overview highlights that the geometry handling system is in use within MAUS and the designed structure and flow of the models has been maintained. The models continue to be modelled using the tessellated shapes and information is added using an XML that describes MICE specific information.

Figure 4.24 displays the MAUS User Guide description of the available

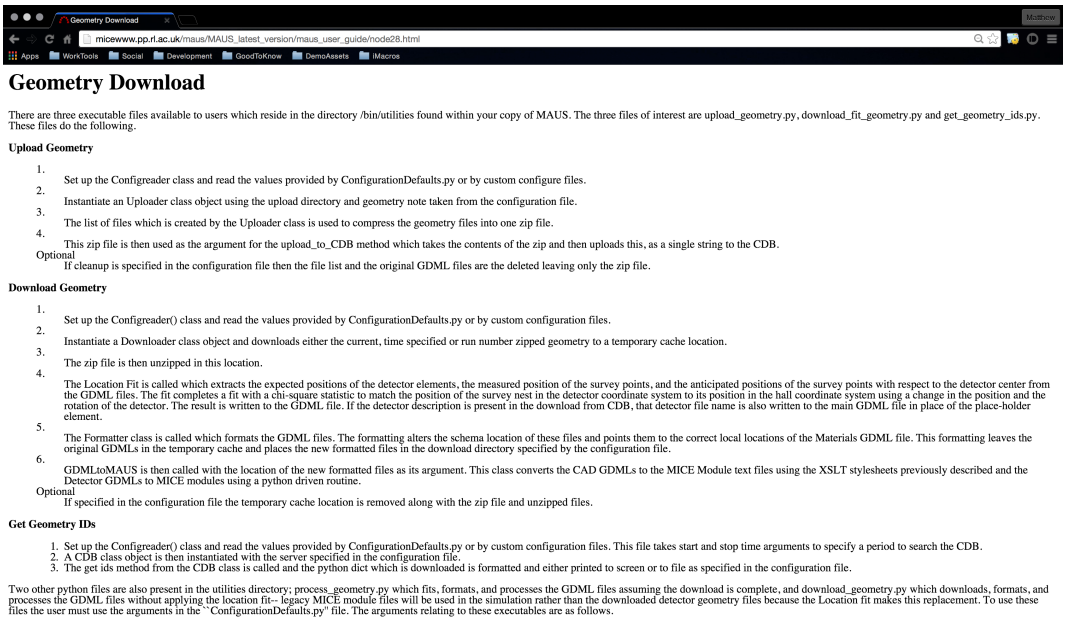

Geometry Download

micewww.pp.rl.ac.uk/maus/MAUS_latest_version/maus_user_guide/node28.html

Apps WorkTools Social Development GoodToKnow DemoAssets iMacros

Geometry Download

There are three executable files available to users which reside in the directory /bin/utilities found within your copy of MAUS. The three files of interest are upload_geometry.py, download_fit_geometry.py and get_geometry_ids.py. These files do the following.

Upload Geometry

1. Set up the Configreader class and read the values provided by ConfigurationDefaults.py or by custom configure files.
2. Instantiate an Uploader class object using the upload directory and geometry note taken from the configuration file.
3. The list of files which is created by the Uploader class is used to compress the geometry files into one zip file.
4. This zip file is then used as the argument for the upload_to_CDB method which takes the contents of the zip and then uploads this, as a single string to the CDB.

Optional
If cleanup is specified in the configuration file then the file list and the original GDML files are the deleted leaving only the zip file.

Download Geometry

1. Set up the Configreader() class and read the values provided by ConfigurationDefaults.py or by custom configuration files.
2. Instantiate a Downloader class object and downloads either the current, time specified or run number zipped geometry to a temporary cache location.
3. The zip file is then unzipped in this location.
4. The Location Fit is called which extracts the expected positions of the detector elements, the measured position of the survey points, and the anticipated positions of the survey points with respect to the detector center from the GDML files. The fit completes a fit with a chi-square statistic to match the position of the survey nest in the detector coordinate system to its position in the hall coordinate system using a change in the position and the rotation of the detector. The result is written to the GDML file. If the detector description is present in the download from CDB, that detector file name is also written to the main GDML file in place of the place-holder element.
5. The Formatter class is called which formats the GDML files. The formatting alters the schema location of these files and points them to the correct local locations of the Materials GDML file. This formatting leaves the original GDMLs in the temporary cache and places the new formatted files in the download directory specified by the configuration file.
6. GDMLtoMAUS is then called with the location of the new formatted files as its argument. This class converts the CAD GDMLs to the MICE Module text files using the XSLT stylesheets previously described and the Detector GDMLs to MICE modules using a python driven routine.

Optional
If specified in the configuration file the temporary cache location is removed along with the zip file and unzipped files.

Get Geometry IDs

1. Set up the Configreader() class and read the values provided by ConfigurationDefaults.py or by custom configuration files. This file takes start and stop time arguments to specify a period to search the CDB.
2. A CDB class object is then instantiated with the server specified in the configuration file.
3. The get ids method from the CDB class is called and the python dict which is downloaded is formatted and either printed to screen or to file as specified in the configuration file.

Two other python files are also present in the utilities directory; process_geometry.py which fits, formats, and processes the GDML files assuming the download is complete, and download_geometry.py which downloads, formats, and processes the GDML files without applying the location fit-- legacy MICE module files will be used in the simulation rather than the downloaded detector geometry files because the Location fit makes this replacement. To use these files the user must use the arguments in the ``ConfigurationDefaults.py'' file. The arguments relating to these executables are as follows.

Figure 4.24: MAUS User Guide - geometry download [51].

executables that interact with the system. These have been previously described in this chapter and enable the user to Upload, Download and query models from the CDB. The User Guide does display work that has been done upon the system since the work done in this chapter. Figure 4.25 displays the control parameters that have been exposed for use by the user. Some of the parameters, such as G4_step_max, have been included to allow simulation directly from download. Improvements to the system in integrating it more fully with MAUS have been undertaken to provide this functionality. The downloading and construction of the model and legacy detector models remains the same as described here.

The final image taken from the MAUS User Guide describes how to use the download executable and can be seen in Figure 4.26. This give an example of the geometries that are available from the CDB and also describes the use of the download executable.

My contribution to this work was to write the code that handles the CAD model translation and the interaction with the CDB that stores the models.

Table 5.1: Geometry control parameters.

Geometry controls.	
`cdb_upload_url`	Sets the upload url relating the the Configuration Database.
`cdb_download_url`	Sets the download url relating the the Configuration Database.
`geometry_download_wsdl`	Name of the web service used for downloads.
`geometry_download_directory`	Set the directory where you wish the geometry to be downloaded to.
`geometry_download_by`	This can be set to either *current*, *id* or *run_number*. Current will download the current valid geometry stored on the CDB. ID will download the geometry for the ID specified N.B ID numbers can be found using the get geometry ids executable. Run_number will download the geometry along with control room information for specified run including the beam-line currents.
`geometry_download_run_number`	Set the number of the run to be downloaded.
`geometry_download_id`	Set the number of the geometry ID to be downloaded.
`geometry_download_cleanup`	Set to True in order to cleanup the temporary files created during the download process. These are the zip file downloaded and the original GDML files from this zip file.
`g4_step_max`	Set the G4 step max number which will be set in the ParentGeometryFile. This relates to the size of steps carried out during the simulation.
`geometry_upload_wsdl`	Name of the web service used for uploads. For developers use only.
`geometry_upload_directory`	Set the the directory which stores the Fast-RAD produced GDML files which will be stored on the CDB. For Developers use only.
`geometry_upload_note`	Write the description of the geometry which is going to be uploaded. This should describe what is in the beam line specifically what is new to the model. It should also include any other information the developer wishes the user to know. For developers use only.
`geometry_upload_valid_from`	Set the date-time format of the date when this geometry about to be uploaded is valid from. For developers use only.
`geometry_upload_cleanup`	Set to True in order to cleanup the temporary files created during the upload process. These are the file containing the list of GDMLs to be uploaded and also the original GDML files. For developers use only.
`get_ids_start_time`	Set the start time of the period which you would like to get the ids from the configuration database. Must be in date-time format.
`get_ids_stop_time`	Set the stop time of the period which you would like to get the ids from the configuration database. Must be in date-time format.
`get_ids_create_file`	Set to True in order to create a file which lists the geometries available within the time period specified. If set to False the geometry information will be printed to screen.

Figure 4.25: MAUS User Guide - geometry controls [51].

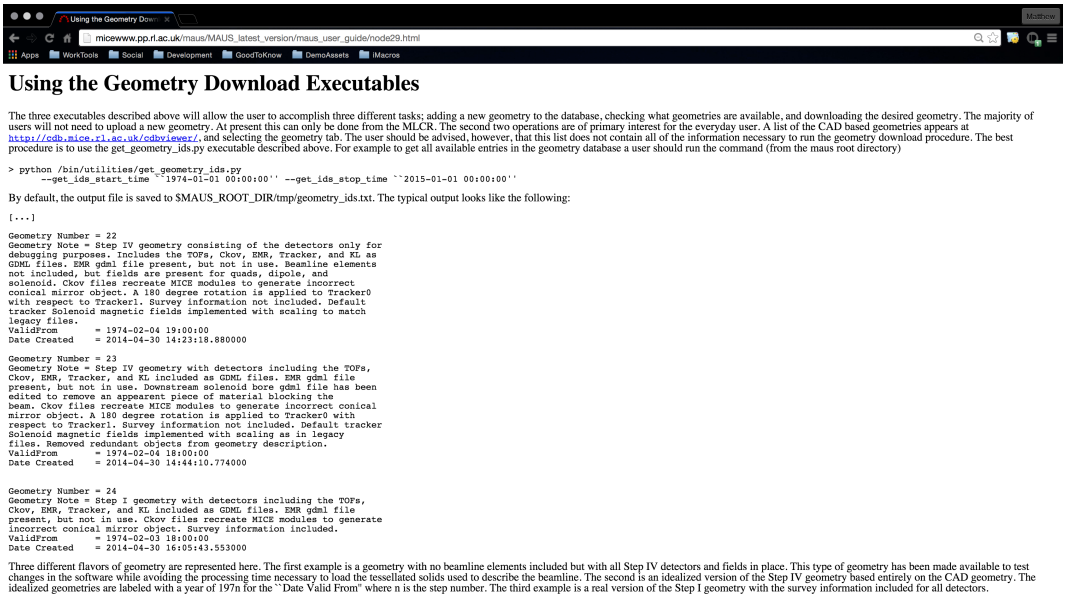

micewww.pp.rl.ac.uk/maus/MAUS_latest_version/maus_user_guide/node29.html

Apps WorkTools Social Development GoodToKnow DemoAssets iMacros

Using the Geometry Download Executables

The three executables described above will allow the user to accomplish three different tasks; adding a new geometry to the database, checking what geometries are available, and downloading the desired geometry. The majority of users will not need to upload a new geometry. At present this can only be done from the MLCR. The second two operations are of primary interest for the everyday user. A list of the CAD based geometries appears at http://cdb.mice.rl.ac.uk/cdbviewer/, and selecting the geometry tab. The user should be advised, however, that this list does not contain all of the information necessary to run the geometry download procedure. The best procedure is to use the get_geometry_ids.py executable described above. For example to get all available entries in the geometry database a user should run the command (from the maus root directory)

```
> python /bin/utilities/get_geometry_ids.py
      --get_ids_start_time ``1974-01-01 00:00:00'' --get_ids_stop_time ``2015-01-01 00:00:00''
```

By default, the output file is saved to $MAUS_ROOT_DIR/tmp/geometry_ids.txt. The typical output looks like the following:

```
[...]

Geometry Number = 22
Geometry Note = Step IV geometry consisting of the detectors only for
debugging purposes. Includes the TOFs, Ckov, EMR, Tracker, and KL as
GDML files. EMR gdml file present, but not in use. Beamline elements
not included, but fields are present for quads, dipole, and
solenoid. Ckov files recreate MICE modules to generate incorrect
conical mirror object. A 180 degree rotation is applied to Tracker0
with respect to Tracker1. Survey information not included. Default
tracker Solenoid magnetic fields implemented with scaling to match
legacy files.
ValidFrom      = 1974-02-04 19:00:00
Date Created   = 2014-04-30 14:23:18.880000

Geometry Number = 23
Geometry Note = Step IV geometry with detectors including the TOFs,
Ckov, EMR, Tracker, and KL included as GDML files. EMR gdml file
present, but not in use. Downstream solenoid bore gdml file has been
edited to remove an eppearent piece of material blocking the
beam. Ckov files recreate MICE modules to generate incorrect conical
mirror object. A 180 degree rotation is applied to Tracker0 with
respect to Tracker1. Survey information not included. Default tracker
Solenoid magnetic fields implemented with scaling as in legacy
files. Removed redundant objects from geometry description.
ValidFrom      = 1974-02-04 18:00:00
Date Created   = 2014-04-30 14:44:10.774000


Geometry Number = 24
Geometry Note = Step I geometry with detectors including the TOFs,
Ckov, EMR, Tracker, and KL included as GDML files. EMR gdml file
present, but not in use. Ckov files recreate MICE modules to generate
incorrect conical mirror object. Survey information included.
ValidFrom      = 1974-02-03 18:00:00
Date Created   = 2014-04-30 16:05:43.553000
```

Three different flavors of geometry are represented here. The first example is a geometry with no beamline elements included but with all Step IV detectors and fields in place. This type of geometry has been made available to test changes in the software while avoiding the processing time necessary to load the tessellated solids used to describe the beamline. The second is an idealized version of the Step IV geometry based entirely on the CAD geometry. The idealized geometries are labeled with a year of 197n for the ``Date Valid From'' where n is the step number. The third example is a real version of the Step I geometry with the survey information included for all detectors.

Figure 4.26: MAUS User Guide - geometry download use [51].

This work included the integration with MAUS in order to use the translated models for use by the overall software package. I also collaborated with the engineering team to produce the initial CAD models that were the starting point for the model used in MAUS. The work formed the basis of geometrical model handling and version control within MAUS and is still in use today.

Chapter 5

SLitrani Photon Simulation

5.1 Introduction

This chapter presents the work that was carried out on modelling the scintillating bars used in the EMR detector. This work used a photon simulation package to understand the behaviour of photons within the bar. Further studies were carried out upon the physical bar to validate the model. The model can be used to inform the analysis of data from the EMR and provides valuable input into the EMR's digitisation code within MAUS.

5.2 Monte Carlo Simulations

In order to support the simulation of the EMR in MAUS a photon simulation package is used to create a model of the individual scintillating bars. Modelling the behaviour includes understanding the number of photons generated in the scintillator and the transmission efficiency of the photons as they pass through the different materials of the detector. The program used is SLitrani [53], this is a photon simulation program based upon ROOT. The results show yield efficiencies of photon capture and give an insight into the number of photons generated at different points within a bar. The purpose of the simulation is to model the bar and the behaviour of light in the bar in order to provide a suitable parametrisation for MAUS to transform the

GEANT sensitive volume data into MICE DAQ data. This process is known as digitisation within MAUS.

5.2.1 Monte Carlo Set Up and Material Modelling

The first step was to measure the emission spectrum of the bar. A sample bar was cut down to a small piece measuring roughly a 1 cm cross section and 4 cm long. This was placed in a fluorescent measurement device, the Horiba Scientific FlouroLog -3 [54] coupled with a R298P Photomultiplier detector. The test material is then irradiated with a β source and the resultant emission spectrum was recorded. The emission spectrum was then modelled within SLitrani in order to provide data to model the bar's behaviour. Figure 5.1 is the spectrum that was modelled. What is not entirely clear is that there are two curves within the plot, a red dotted curve and a blue one. The red line depicts the emission spectrum that was produced by the FlouroLog device, the blue line is the modelled emission spectrum used in the simulation. The peak emission is roughly at 420 nm.

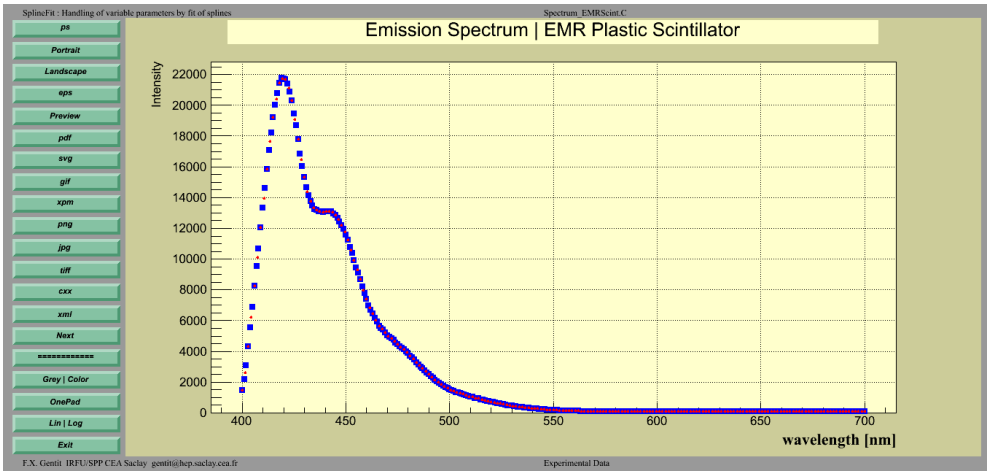

Figure 5.1: Emission spectrum of EMR plastic scintillator.

SLitrani makes use of two databases to define spectra to be used within the modelling of materials. The first database, known as the TSplineFit database, contains real, measured spectra, these are purely for reference and

the data within them cannot be assigned to a volume within the model to define its behaviour. An example of data that can be stored is the red line in Figure 5.1.

The second database, known as the TLitSpectrum database can be used to assign spectra to materials within the model. In order to input a spectrum taken from real data into this database one must use a spectra from the first TSplineFit database. SLitrani provides a function whereby the user can input a spectra from the first database and the function will break the data into a number of Gaussian fits. The equation defining the Gaussian fits can be altered by the user to produce a better fit. Once complete this new Gaussian fit of the spectra from the first database can be stored in the second database. This can then be assigned to a material.

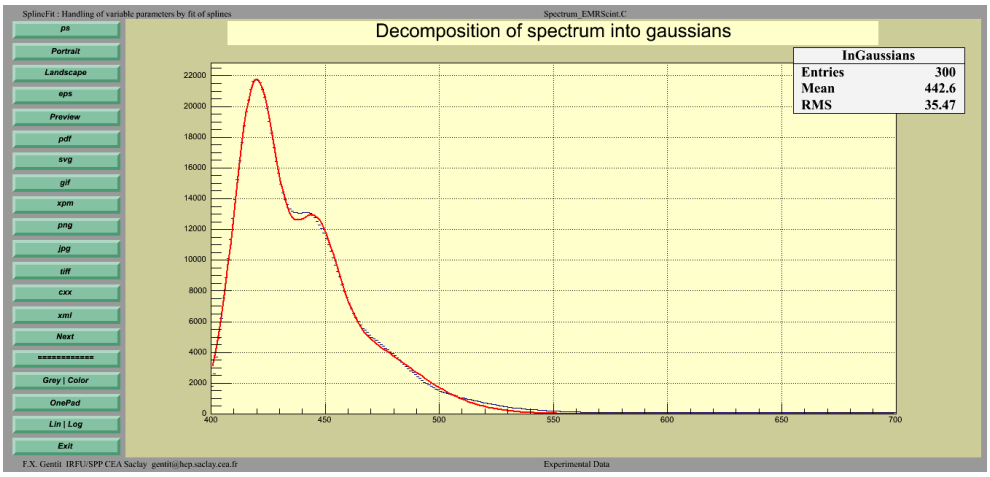

Figure 5.2: Fitting of a curve to the scintillator emission spectrum.

Figure 5.2 is the result of the TLitSpectrum fit of data taken from the first database. The red curve is the fitted curve that is calculated by the fitting method provided by SLitrani. The blue curve is entered into the TSplineFit database. It is clear that the fitted curve is very close to the data and provides a satisfactory model for behaviour of the plastic scintillator.

The second component of the EMR bar is the WLS fibre that runs through the centre of the bar. In order to model this the data of the absorption and emission is required. Figure 5.3 is the absorption and emission spectrum for

the fibre used in the EMR bar. This fibre is BCF 92 and is manufactured by Saint-Gobain Crystals. In figure 5.3 the absorption spectrum's amplitude is not given in cm and needs to be converted into a distance in order for the information to be input into SLitrani. This data has been taken from the Saint-Gobain fibre brochure [55].

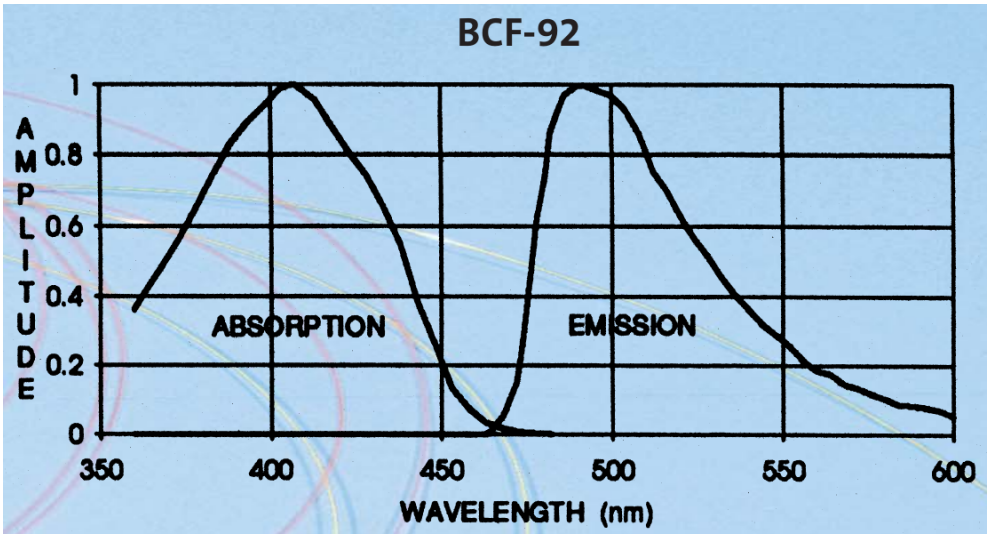

Figure 5.3: Manufacturers absorption and emission spectrum for BCF 92 WLS fibre. [55]

Research into the subject found that group A within the CMS have modelled the fibre BCF 91A produced by Saint-Gobain. Although this is a different fibre the manufacturers brochure shows that the fibres are similar except 92 has a different time decay and absorption spectrum. Nonetheless the process required to convert the amplitude given in the brochure to cm is the same for each fibre. The CMS team converted to cm with the following equation [56]. Amplitude = 0.3 cm - f(λ) $\times$ 0.28 cm where f(λ) represents the absorption curve from Saint-Gobain. Applying this equation to the values seen in the absorption spectrum yields absorption lengths for the range of wavelengths seen in the Saint-Gobain brochure and the absorption curve produced can be seen in Figure 5.4. The peak absorption is 0.02 cm at around 405 nm.

The WLS operates by absorbing photons at a wavelength of around 400

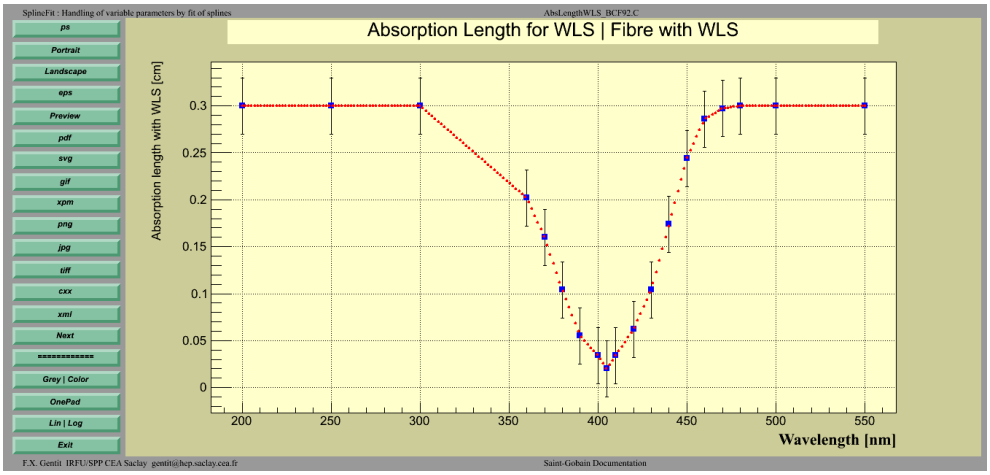

Figure 5.4: Absorption length spectrum for BCF 92 WLS fibre.

nm and re-emitting them at around 500 nm; it is important this region is accurately modelled. Modelling the fibre's absorption uses the data provided in Figure 5.3; this only provides information for a particular wavelength range. Wavelengths outside this range are assumed by SLitrani to have an absorption length of 0 cm if no length is defined. This causes photons to stop being simulated resulting in the loss of data. An approximate absorption length of 0.3 is provided for below 300 and above 480 nm. This is an initial approximation that can be verified and altered later if necessary.

Figure 5.5 is the emission spectrum input into SLitrani. It peaks at just under 500 nm; the time decay graph is the default time decay produced by SLitrani. This is sufficient for the initial simulations but can be refined later if required.

To verify the WLS fibre behaves in the manner required a simple simulation was conducted. The simulation modelled the fibre, with dimensions that reflect reality, with a light source at one end and a general detector at the other end. The default physics settings of SLitrani were used. The fibre itself was also made into a detector in order to see the wavelengths of the photons within the fibre. 10,000 photons were simulated at a wavelength of 400 nm entering the fibre. SLitrani provided the details of the photons moving through the fibre, this information verified that photons were reaching

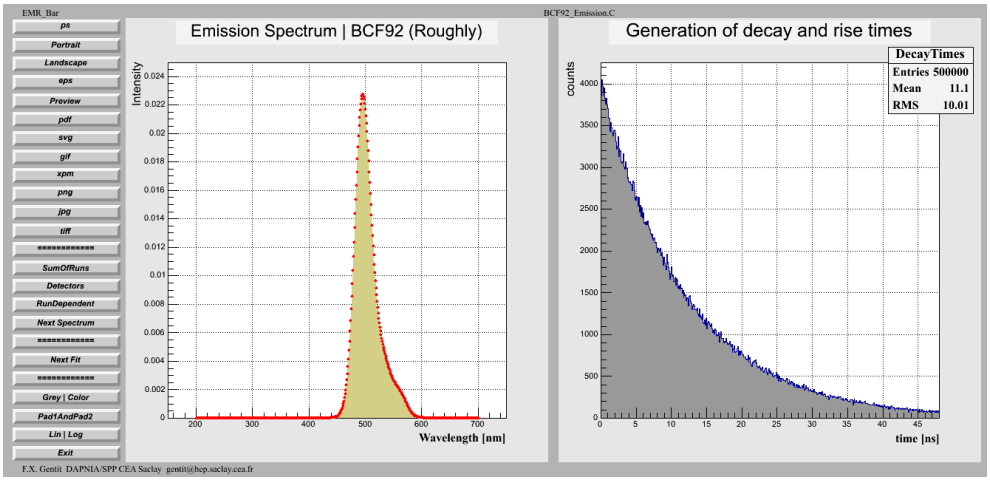

Figure 5.5: Emission spectrum for BCF 92 WLS fibre.

the detector as required. This was a rudimentary test to ensure that photons were being transported.

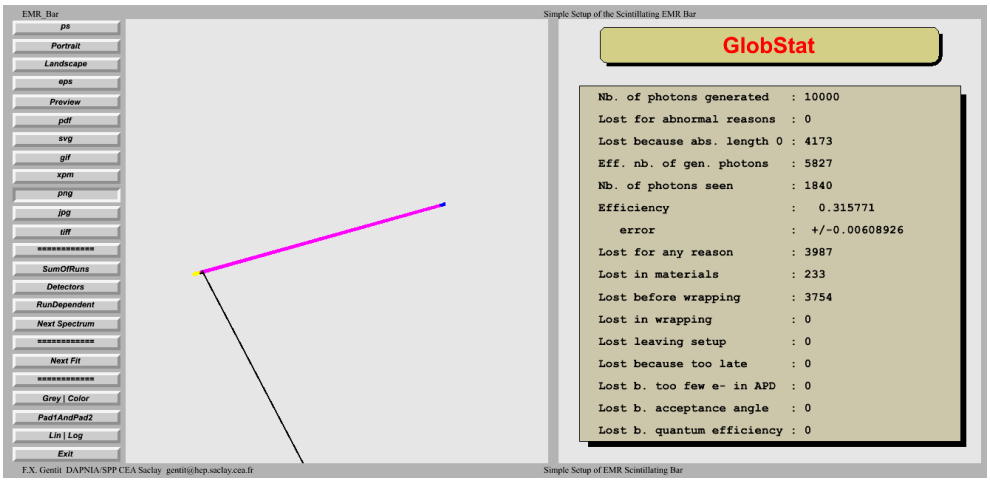

Figure 5.6: SLitrani output for WLS verification simulation.

Figure 5.6 shows the simulation undertaken to verify the fibre was transporting photons. The image shows the simulation's model; the pink cylinder is the fibre, the photon source is positioned at the left most face of the pink cylinder and at the right most face the general detector is placed. The black lines seen are the tracks of some photons as they leave the source and are

reflected by the surface of the fibre. It shows an efficiency of around 30%, this relates to photons seen by both the fibre and the detector. Assuming that the fibre has no scratches or cracks within it and that the ends of the fibre have a mirror finish, this is a good representation of the fibre. The real fibre will have scratches and imperfect ends which will contribute to lowering the fibre's efficiency. This efficiency seen in the simulation is a ratio of the number of photons produced to the number seen by the detectors. The fact that the fibre itself is being modelled as a detector, means all of the photons within the fibre and detector are recorded in order to understand transmission between them. The photons seen in the detector will be the shifted photons and therefore will match the emission spectrum.

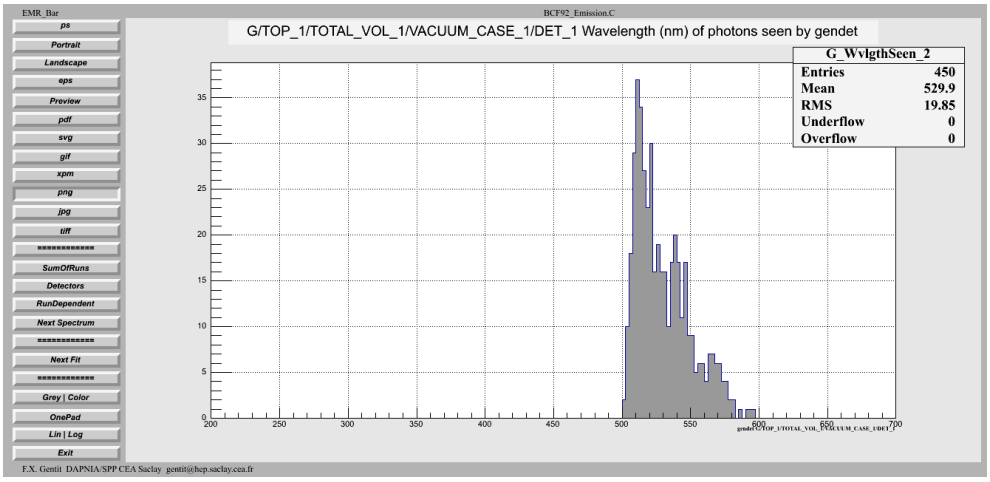

Figure 5.7: Wavelengths of photons seen by the general detector.

Figure 5.7 shows that 450 photons have reached the general detector at the end of the fibre. The photons have a wavelength range that centers on 530 nm. The simulation generated photons with a range centred on 400 nm. This shows that these photon's wavelengths have been shifted. It can also be seen that the wavelength distribution is that of the emission spectrum, Figure 5.5, which was assigned to the fibre. Secondly there is a sharp cut off of photons around 500 nm and this is due to the fibre being a "fast shifter" where shorter wavelength photons are lost during transit.

Figure 5.8 shows the photons in the WLS fibre. It shows that the spread

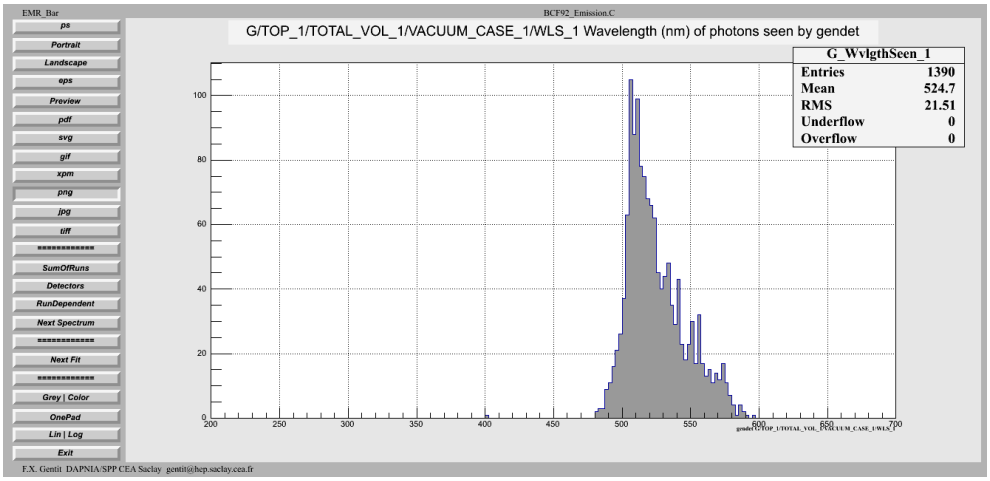

Figure 5.8: Wavelengths of photons seen by the WLS fibre detector.

of the shifted photons is greater in the fibre than the detector. The sharp cut off of photons at 500 nm cannot be seen in this plot. The number of photons seen by the WLS is nearly three times larger than those seen in the detector meaning that nearly two thirds of the photons are lost or are captured within the fibre during transit. Finally, there is a small peak of photons at 400 nm that shows that the photons produced by the source are seen by the WLS and are indeed shifted to the greater wavelengths as expected. One might expect to see a larger peak at the 400 nm point, it is unknown at this time why this peak is not larger. Further investigation into the reason for this was not pursued due to time constraints.

The spectra that were added to the different materials within the EMR bar means that the bar can be modelled and investigations into the behaviour of the full bar can be conducted. The assembly of the full bar included adding three thin slices of material to the WLS fibre. The slices cover the fibre's surface and have been introduced in order to model the fibre's cladding. The fibre's cladding consists of two layers with the same material as the bar. The first and second slices are the two cladding layers, adding the slices in the simulation will ensure that reflection of light at these boundaries is modelled. The cladding is there to protect the fibre and also to aid photon capture. The third slice represents the epoxy resin that the fibre is enclosed in, in order to

secure it within the plastic bar. The bar itself also has a thin slice added to its surface which will represent the plastic coating which the bar is coated in. This coating is added to the bar to protect the scintillator and aid photon capture.

The simulation that was conducted are described below:

Z Position Simulation

Particles and point light sources were used to produce light within the bar at different positions along the bar's length. The efficiencies for each position were observed.

The data produced from this simulation was compared to the experiments involving the real bar.

5.3 Simulations

We require the simulation of the scintillating bar to represent reality. The EMR bars are designed to be excited by the passage of charged particles within the MICE beam. A well collimated source of particles with sufficient intensity is unavailable for use in the laboratory as there is no access to such sources. Laboratory experiments use a laser to excite the bar, although this is a different method of excitation the subsequent propagation of light will be the same. SLitrani models this system with a source of muons that pass through the plastic at the desired locations.

Figure 5.9 shows the set up of the simulation, the pink object is the scintillating bar that houses the modelled WLS fibre. The blue object at the far right end of the bar is the general detector that will record data about any particles that pass through it. The yellow object beneath the bar is the source, which can be set to simulate a number of different types of source. This image depicts a source that is simulating a laser but the Z position simulations will use muons. The black lines represent photons that are captured by the bar and the WLS fibre. This image has been taken from the initial simulations which were conducted and the dimensions of the bar

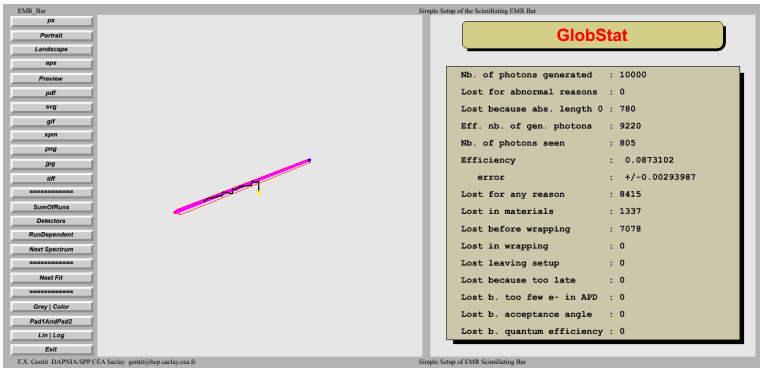

Figure 5.9: Example of SLitrani model.

has been refined since this stage of the investigation. This image has been shown to give an idea of the set up of the overall simulation.

5.3.1 Z Position Simulation

The Z position simulations model the experiments that moved the source along the length of the bar. The efficiency of the photon collection can then be shown as the particle hit moves towards the PMT. Firstly, a simulation was run with the source in the centre of the bar. For this simulation the WLS fibre has been set to be a sensitive detector. The detector at the end of the fibre is the only other detector. The purpose of this simulation is to determine the number of photons generated in the plastic and the subsequent number that were captured in the fibre and then transported to the detector. This will determine the efficiencies.

Figure 5.11 shows the wavelengths and the number of photons that are seen by the WLS fibre. For this simulation 816 photons were collected by the fibre, Figure 5.10 shows the number of photons that were generated in the overall simulation. This represents the photons generated in the plastic; for this simulation 10 muons at an energy of 240 MeV were generated in the source and directed towards the bar. Roughly 67,000 photons were generated in the plastic seen in Figure 5.10, this gives a WLS fibre collection efficiency of 1.2%. Figure 5.11 does not show many photons with a 400 nm wavelength

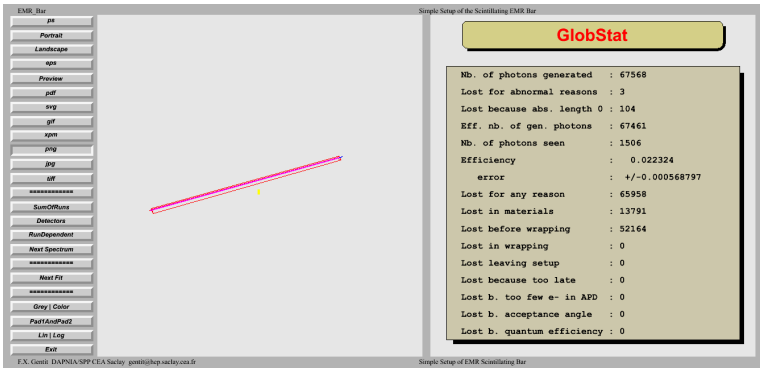

Figure 5.10: Photon numbers seen.

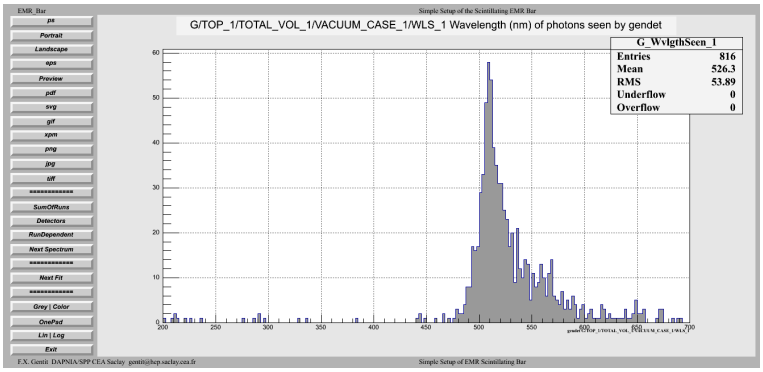

Figure 5.11: Photon numbers seen by the WLS fibre.

but a scatter of them down to 200 nm. The reason for this is unknown and further investigation is required, this cannot be understood in this body of work due to time constraints.

Figure 5.12 shows the wavelengths of the 690 photons seen by the detector at the end of the fibre. This equates to 85% efficiency for photons produced entering at the interaction point and reaching the end of the fibre. This efficiency does appear to be high, the reason for this is unknown and further investigation is needed to determine its accuracy. Due to time constraints understanding this efficiency could not be carried out in this body of work. The efficiency of photons generated in the plastic and then collected in the detector is 1%.

The next simulation that was carried out is that of moving the source

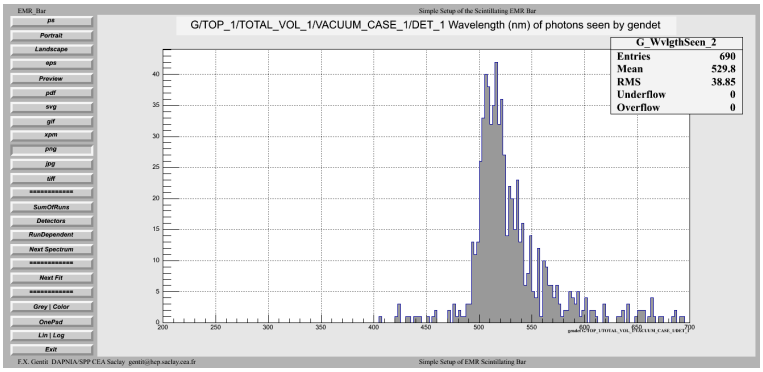

Figure 5.12: Photon numbers seen by the detector.

along the length of the bar and measuring the efficiency for each point and comparing this to the position of the hit.

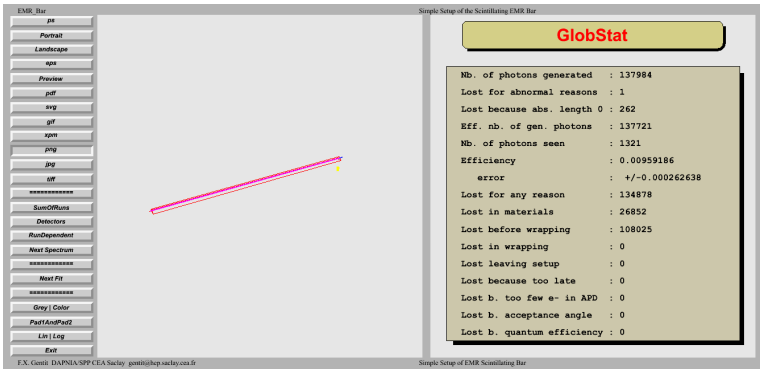

Figure 5.13: Main simulation results for z position efficiency simulation with muons.

Figure 5.13 shows the main results of the simulation where the source has been moved along the bar. For this simulation a single muon was fired into the bar at each position and the source was moved in 10 cm intervals. The initial position of the source was at the opposite end of the PMT. Again, the energy for the muons remained at 240 MeV. The WLS fibre was not set to be a sensitive detector for the simulation, only the detector itself. The right hand panel in Figure 5.13 gives an efficiency of roughly 1% which is that seen in the previous simulations.

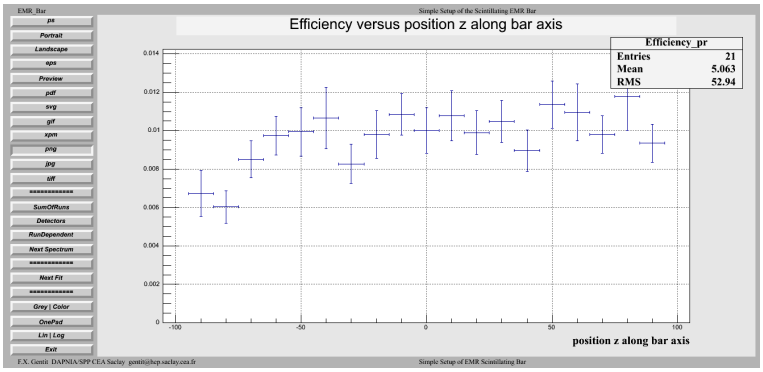

Figure 5.14: Main simulation results for z position efficiency simulation.

Figure 5.14 is the plot of the efficiency of photon collection for each point along the bar. The plot suggests that the efficiency is flat along the bar except for a tapering off of efficiency at the opposite end to the detector.

5.4 Conclusion

The purpose of the simulations carried out in this chapter were to support the studies being conducted upon the scintillating bars. The study also gave an insight into the efficiencies of the photons as they move between the different components of the bars. These could be used in the MAUS program in order to improve the accuracies of the model.

The simulations carried out will be compared to the experiments that will be carried out and relationships between hit position and light yield can be determined at that point.

Chapter 6

EMR Scintillator Characterisation

6.1 Introduction

Detectors can be divided into two categories based on their purpose. Detectors such as trackers and cloud chambers measure the particle's position in space allowing their trajectory to be reconstructed. This is important to MICE because the aim is to measure the beam's emittance. Emittance is a function of momentum and position therefore knowing a particles trajectory is vital.

Other detectors such as TOF and the EMR provide particle identification. Distinguishing between particle types within a beam is important. MICE must identify muons in a beam that contains electrons and pions as well. The emittance measurement must be to within one part in a thousand, and too much contamination will render this unobtainable. The TOF detectors do not allow the beam purity to be determined reliably enough and so a second, independent measurement is required. This is provided by the EMR which uses a different method to identify the particles and allows the target accuracy for the measurement to be reached. This chapter will focus upon the EMR. The work presented here was done in order to understand the optical behaviour of the scintillating bars used in the EMR. The information

could then be used to validate the physics simulation model presented in Chapter 5. That model will be a reliable base and can be used to write the MICE specific code that models the EMR.

6.2 EMR

The EMR resides at the end of the beam line acting as a beam stop. All of the beam enters the detector which comprises of a 1 m^3 block of scintillator. The block is made up of scintillator planes perpendicular to the beam's travel. The EMR is used in conjunction with the TOF detectors in order to identify muons that have decayed within the cooling channel. The particles that have decayed while traversing the cooling channel can then be distinguished between those that have successfully traversed the cooling channel and this reduces the uncertainty on the emittance measurement. The EMR consists of layers of triangular scintillating bars which are arranged in planes that are at right angles to the beam direction. The construction allows a number of discriminators to be used to identify particles. The first studies the uniformity of deposited energy by a particle as it moves through the detector. Uniformly deposited energy is typical of a muon whereas an electron's deposited energy, which causes an electromagnetic shower, will fluctuate from plane to plane. The second discriminator is related to the width of the deposited energy. A muon's energy will be collimated around the particle's trajectory where an electrons electromagnetic shower will spread sideways as it penetrates the detector.

The scintillating bars used in the EMR have been modified from those used in the Main Injector Experiment for ν -A (MINERvA) experiment [57]. The bars will be used in a stand alone detector rather that being part of a larger device, as seen in MINERvA. Being used in a different manner to the MINERvA detector, it is prudent to fully understand the detector. In particular we need to validate the detector model to allow us to accurately estimate the efficiency and purity of the muon signal that can be extracted from the data. The full design of the EMR has been described in section 3.8.4.

The light generated by a particle interaction is subject to a number of losses. Firstly, the particle excites the scintillator; this excitation produces light. The generated light will move around the bar in the local vicinity of the interaction point and will be captured by the WLS fibre. The WLS absorbs light at one wavelength and re-emits it at a longer one. The longer wavelength is not absorbed by the scintillator so light is transferred down the fibre to the ends. The scintillator specifically produces blue light when excited and the WLS shifts blue light to green. During these processes some light will escape and is lost. Attenuation of the light will also cause losses. The ends of the WLS fibre are set flush against clear fibre. The clear fibre's role is to transport the light to the PMT detectors. Light will also be lost at the point where the WLS meets the clear fibre. Each bar is at a different position in the detector so to keep the length that the light travels equal, all the clear fibres are the same length. Clear fibres closer to the PMT must be bent in order to reach the PMT. All the charge recorded by each bar is collected at one end by a single anode PMT, this measures the charge for the entire plane. Individual PMTs record the charge for each bar at the opposite side of the plane. The clear fibre configuration is more important for the single anode PMT. The bending of the clear fibre also induces losses of light. Losses are again incurred where the face of the clear fibre meets the PMT. The photons that reach this stage of the process are then converted to photoelectrons which then produce the signal. It is this signal that is recorded and analysed.

6.2.1 Scintillating Bars

The scintillating bars used in the EMR were taken from a design developed by MINERvA. The extruded scintillator was also used in the MINOS [58] and Tevatron's D0 Detector. MINOS used 8 m long scintillators sandwiched between steel plates. The extruded scintillators were read out using WLS fibres that were incorporated into the plastic. Their decision to use this set up was mainly based on the cost advantage of this system. MINERvA sought to use a totally active detector to cope with the high intensity NuMI

neutrino beam. The high statistics require a detector which can read out the data quickly and efficiently. The EMR will have to deal with a similar rate and utilising the technology produced by other experiments is prudent.

MINERvA conducted a study into the performance of the scintillators [59]. The study aimed to investigate the attenuation length and light yield of the bars. It particularly focussed on the effects different diameter WLS fibres would have on the overall performance. Tests were also conducted on the effects the glue used to secure the WLS fibre had on the performance. The glue filled the space between the outside of the WLS fibre and the diameter of the hole through the extruded bar. The test bench for the experiment was simple; the selected bars were housed in a dark box with a PMT at one end of the bar and a reflective surface at the other. A Cs^{137} gamma source was used to excite the bar at four different positions along the bar. The attenuation length that was determined for both diameters of the proposed hole to house the WLS fibre was in the range of 42-44 cm for the long component and approx 30 cm for the short. The study that aimed to determine the light yield for the different configurations of hole diameter to WLS diameter ratio found that there was no correlation with the different ratios. A. Pla-Dalmau shows there is a slight increase of light yielded when the source is closer to the PMT [59].

Scintillation is the main process which the EMR employs to detect ionising particles from the beam. Curran describes the fundamental process of scintillation [60]. Firstly, the atoms and molecules of the luminescent material, the scintillating plastic, receive energy from the incident radiation of the interacting particle. This energy excites and ionises the particles of the scintillator. The atoms and molecules will then de-excite and de-ionise returning to a stable state. This process releases fluorescent radiation, light, which is of a desired emission spectrum. The resultant fluorescence is then captured and transported to the PMT where the signal is read out and recorded.

The extruded scintillating bars used in the EMR have been manufactured using polystyrene (PS) pellets. A dopant mixture of 1% PPO (2,5-diphenyloxazole) and 0.03% POPOP (1,4-bis(5-phenyloxazol-2-yl) benzene) was added to the PS to allow the plastic to scintillate. The final bar emits

blue light and has been designed to have an absorption cut-off wavelength of approximately 400 nm and a maximum emission wavelength of 420 nm. To verify these properties and obtain an emission spectrum to be used in simulation, a sample piece of the plastic cut from an EMR bar was illuminated using the FlouroLog -3 [54]. The FlouroLog excites the source using a 450 W xenon lamp, the detector used in determining the emission spectrum is a R928P photomultiplier. The FlourLog excites the source across a range of wavelengths and records the corresponding emission using the detector. Figure 6.1 shows the emission spectrum that was obtained from the sample.

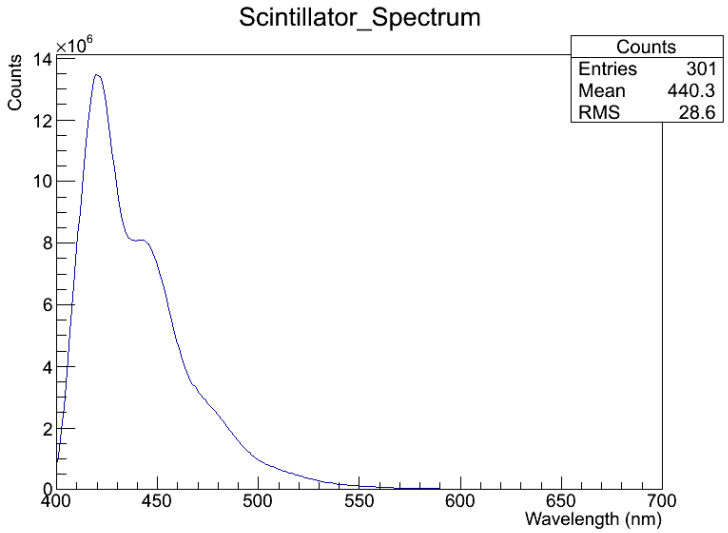

Figure 6.1: Emission spectrum of EMR scintillating bar.

To capture the yielded light a WLS fibre will run through the center of each bar. The fibre is a fast blue to green shifter with an emission peak of 492 nm and a decay time of 2.7 ns. The configuration of the bar aims to ensure that as much fluorescent light produced reaches the detecting equipment as possible.

6.3 Method

Experiments were carried out on a bar taken from the EMR. The data collected from these experiments were then used to support and validate simulations that model the light's behaviour within the bar. The light modelling simulation is SLitrani [53]. The MAUS simulation uses sensitive volumes to provide data to the user. This data does not come in the form that is produced by the DAQ for this detector. Meaning that the analysis code, designed to consume DAQ output, cannot be used unless the sensitive volume data is transformed to resemble DAQ output. In order to perform this transformation within MAUS the inner workings of the detector, such as the light's behaviour within the scintillators, must be known. The experiments measure the optical properties of the bars and are used to support the SLitrani model and simulation. This can then be used to create a parameterisation for MAUS.

The experiment was designed to determine a relationship between the light generated as a function of the particle's interaction position in the bar. The bar is an extruded triangular prism meaning the particle interaction point will determine the amount of light generated and thus the signal produced by the detecting PMTs. Particle hits that fall closer to one of the PMTs will also produce a larger signal. This experiment uses an LED to illuminate the bar at increments along the bar's length. Blue and white lasers are then scanned across the bar's length and width. Both response time and PMT output charge are be recorded for the LED and laser. The EMR bar includes a scintillating bar and a WLS Fibre, which is glued in the centre of the bar. Testing the fibre on its own and the full bar aids in separating the behaviours of the two elements of the complex system that is the full bar.

The following experiments were conducted to fully understand the bar's behaviour. Figure 6.2 depicts the set up used.

Charge Experiment

This experiment measures the PMT charge of both the fibre on its own and a complete bar across its length and width where possible. An LED, laser and radioactive source will be used to illuminate the fibre

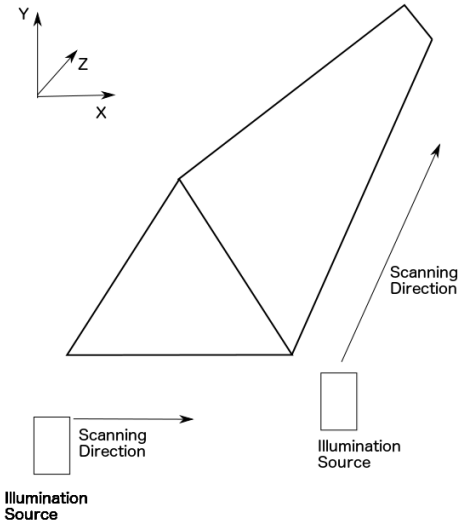

Figure 6.2: Schematic of the experiments to be undertaken upon the bar. A source, LED, laser or radioactive source, scans along the X and Z direction.

and bar.

Response Time Experiment

This experiment will measure the PMT charge of both the fibre on its own and a complete bar across their length and width where possible. An LED and laser are used to illuminate the fibre and bar.

Photon Simulation - SLitrani

A simulation of a single bar is carried out. Its aim is to determine the photon capture efficiency of the bar (Chapter 5).

Plane Efficiency Experiment

This experiment uses a single layer of the EMR itself to determine its efficiency over a range of different voltages with two different types of PMT. This is to determine the most efficient set up for the detector and the measured efficiencies will be used in the software.

6.3.1 Experimental Set Up

The entire experiment is housed in a large, light tight, dark box. The test bar is supported by two shoulders that were manufactured in house to suit the dimensions of the bars. These shoulders ensured the bar was located in the exact same position for every data run.

A translation deck, located underneath the bar, provides the ability to move the source or laser in both the x and z directions along the bar. It is controlled via a dedicated PC which provides the calibrated location of the source or laser. The z direction is controlled by an Anorad [61] translation deck. This locates the excitation source along the length of the bar. Due to the size of the overall housing this stage cannot move the entire length of the bar but can move the majority of the bar. It can move up to approximately the last 8 cm of the bar so this last 8 cm is not measured. This will be adequate for taking data. The translation stage is only capable of moving the deck in one direction, therefore a novel solution was sought to allow a second degree of freedom.

A Lego Mindstorms [62] kit was used to create a deck that could provide controlled movement in the x direction, across the width of the bar. It comprises of a motor and a small stage that is set upon a rack and pinion. The motor can drive the stage in a forward/backward direction across the bar's width and can be controlled with good accuracy. The Lego set up allows the laser or source to be positioned to within a millimetre. As with the main translation stage the motor of the Lego translation stage is controlled via a dedicated PC. The PC in question has access to both translation devices which gives simultaneous control over both directions. Lego was selected for its ease of construction and its precision engineering. The combined stages are both controlled with user programs that enable full automation of the illumination source positioning. I designed and implemented this code.

Figure 6.3 shows the LED support that was built for the LED experiments. The Figure displays the housing for the LED illumination source, illuminating the WLS fibre in a tubular housing.

A PMT is then placed flush to the WLS fibre at each end of the bar.

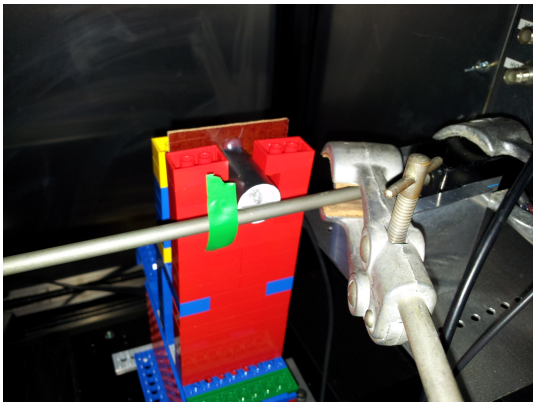

Figure 6.3: Image of the Lego Mindstorms LED support. The image displays an LED (black and white tube) being held by the Lego constructed translation stage (red bricks in image). The stage has been designed so that it can be reconfigured to suit the needs of the bar; what is seen in the image is the WLS fibre in a metal tubular housing held by the clamp.

This, in turn, is connected to an amplifier, a discriminator and finally to either the flash Analogue to Digital Converter (fADC) board or the PicoHarp. Both readout devices are connected to PCs that collect the data and provide analysis of the results.

6.3.2 Readout Equipment

Two measurements were performed during the experiments. The first measurement was of the charge that was output by the PMT and the second recorded the response time.

The PMT charge was measured by an Analogue to Digital Converter (ADC) used with the EMR; the CAEN V1731 board [63]. This is an 8 channel waveform digitiser with a programmable Digital to Analogue Converter (DAC) and 200 to 500 MS/s 8 bit sampling rate. The DAC allows adjustments to be made in order to change the DC offset that is used to reduce noise. This is used to digitise the signal produced by the detecting PMTs. Data collected provides information on the amount of charge that is being collected from the light produced in the scintillator.

The response time was measured by the PicoHarp 300 [64] which is a time-correlated single photon counting instrument. The system can have an input from an electrical output and record the time it takes to receive a trigger. In the case of the experiment being described here the trigger will be the output received from a PMT. The input trigger will be taken from the waveform generator which also triggers the laser or LED. It can be used to determine scintillator response times and has a timing resolution of 4 ps. It has a range of 260 ns to 33 μs and a count rate of up to 10 million counts/sec. This device is ideal to measure the time response of fast scintillators such as those used in the EMR.

6.4 Charge Experiments

This experiments uses a blue LED to illuminate the bar. The LED does excite the scintillator but its light will be captured by the WLS fibre within the bar and measured by the PMT. The LED is then replaced by a laser that gives greater control over the position of the hit and also increases the intensity of the light being captured by the bar. Two different lasers are used: the first is a blue laser whose light is captured by the WLS fibre only, the second is a white laser whose light is captured by the bar. Measurements were made on the WLS fibre on its own as well as the complete bar. This helps to separate the behaviour of the fibre from that of the overall bar. The results seen in this section show the data and effects of the position of the hit on the amount of light collected. The board was calibrated before each of these experiments.

6.4.1 Uncertainties

The experiments that are described have two areas where uncertainties must be taken into account. The first is when measuring the position of the illuminating device, be that the laser or source, and the second is the uncertainties in the ADC measurement. These refer to the uncertainties within the ADC board.

The position of the illumination source is measured using a ruler that is accurate to 1 mm which gives an uncertainty of 0.5 mm. The calculation for the ADC board is undertaken in the analysis script that analyses the output from the board. Firstly, each signal is converted into a charge histogram, each histogram is added together to create a histogram for each data run. Each experiment consists of 10 runs each containing 5000 events (signals). The mean charge measured is calculated for each run and the error on this mean is derived from the RMS width of the distribution divided by the square root of the number of events.

6.4.2 ADC Board Calibration

Before testing can begin the ADC board has to be calibrated. This involves taking a controlled data run and calculating the optimum DC offset value for the board. The optimum value reduces the pedestal noise to a minimum. The calibration is required because of the internal currents of the board itself. This fluctuating current can exceed the trigger level and create a false ADC count.

Obtaining an optimum DC_OFFSET value uses a program that was designed to take a data set across a range of DC_OFFSET voltages. Each data run contains 5000 events and the calibration run requires 100 data runs to scan around the DC_OFFSET voltage range. Each run records the charge that is produced by the PMT. The baseline level of the charge is not stable when the DC_OFFSET value is not at an optimum. Figure 6.4 shows the accumulated charge curves for the first run of the calibration data set.

One can see that the baseline of the curve is between 201 and 202 ADC counts. The oscillation seen is due to noise in the circuit. The level of noise varies with the DC_OFFSET. Custom software analyses a calibration run and determines the optimum voltage to be set for the board in order to reduce the noise to a minimum. This is calculated by integrating across the baseline, where there is no signal, for a window width that matches the signal window.

Figure 6.5 depicts the charge curve with the optimum value of the DC_OFFSET.

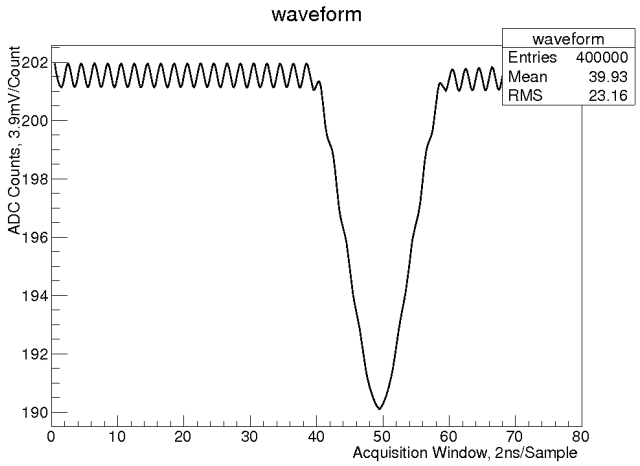

Figure 6.4: Charge curve without optimum DC offset.

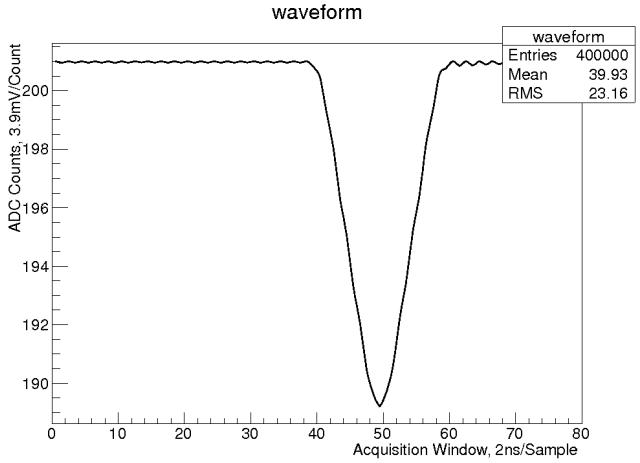

Figure 6.5: Charge curve with optimum DC offset.

The baseline of the curve, 201 counts, shows a marked improvement on the fluctuations compared to Figure 6.4.

Figure 6.6 shows the histogram of the charge before calibration. The right hand peak, approx 900 events, is the accumulated charge integrated during

the signal's acquisition window. The red curve is the charge integrated across the baseline of the curve, which does not include the signal itself, with the same window width as the integration across the signal.

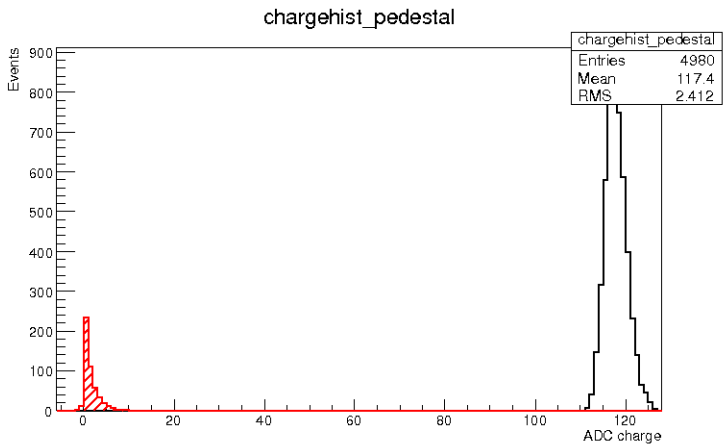

Figure 6.6: Pre calibration charge histogram. ADC charge is in mV.

Figure 6.7 shows the same histogram after the calibration has taken place and the optimum DC_OFFSET voltage has been set. The pedestal charge is clearly narrower and the high tail is reduced.

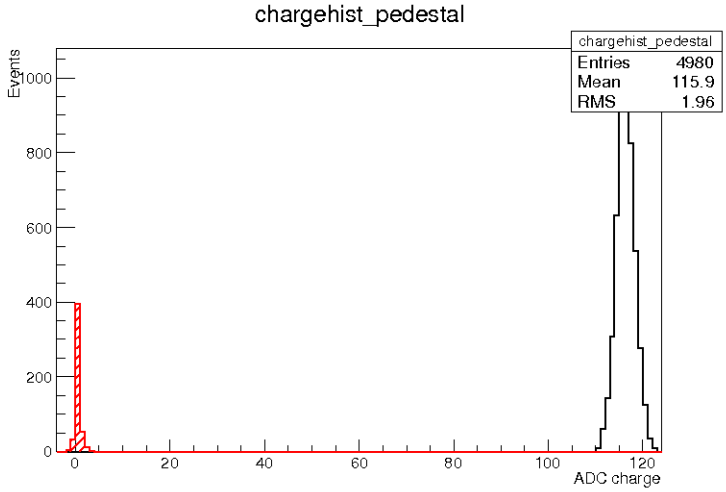

Figure 6.7: Post calibration charge histogram. ADC charge is in mV.

6.4.3 LED Experiments

A blue LED is used to illuminate both the WLS fibre on its own and the complete bar. The light emitted from the LED is captured by the WLS fibre, and the wavelength shifted light carried to the PMT. Blue light produced by the LED favours being captured by the WLS only. When working with the complete bar a white laser will be used because this will favour the light being captured by the scintillator.

WLS Fibre: LED

After the LED is placed in the correct position the ADC board records the output from the PMT. Figure 6.8 shows the recorded waveform seen by the PMT, this is an average of a number of signals.

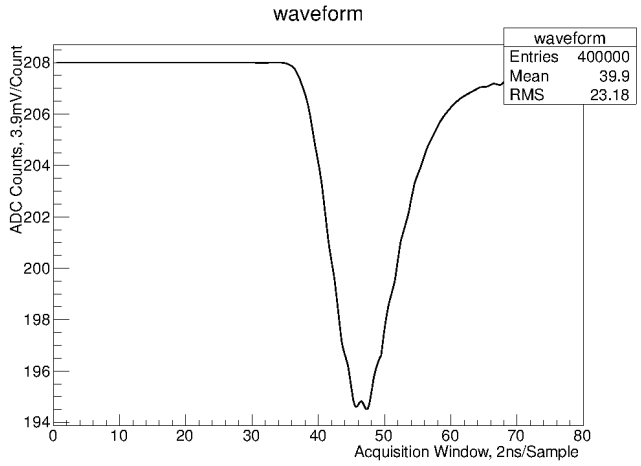

Figure 6.8: Average waveform signal recorded with the LED 5 cm from the PMT.

The actual charge recorded by the signal is taken from integrating a window that covers the signal itself, and subtracting the pedestal value derived by integrating the charge window from 0 to 27 ns.

Figure 6.9 is the charge histogram that is created from nearly 5000 such measurements. The red curve seen in the Figure is the pedestal charge seen

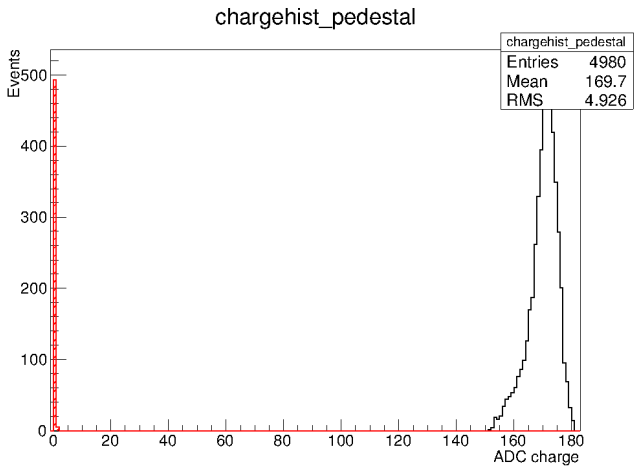

Figure 6.9: Charge histogram recorded with the LED 5 cm from the PMT. ADC charge is in mV.

on the baseline of the signal. The pedestal is narrow showing that the correct DC offset value is present. The black curve shows the charge histogram of the signal itself. The mean value measures the amount of charge collected by the PMT when the bar is excited at the position where the LED has been placed. This process is repeated for a number of different positions and the average charge for each position can then be plotted against the position on the bar.

Figure 6.10 shows that the charge declines as the distance from the PMT is increased. When the light source is closer to the PMT one would expect that the light within the WLS will be recorded by the PMT. As the distance increases, less light reaches the PMT.

For this experiment the WLS fibre was contained within a metal tube. The tube has a larger inner diameter than the diameter of the fibre which left space within the tube. Figure 6.10 shows a linear relationship between charge and distance; this is not as expected. An exponential fall of charge as distance increases is expected. The gap between the fibre and the wall of the tube in which it was housed could explain the linear relationship seen. The relationship of charge yield against distance in air is linear and it appears

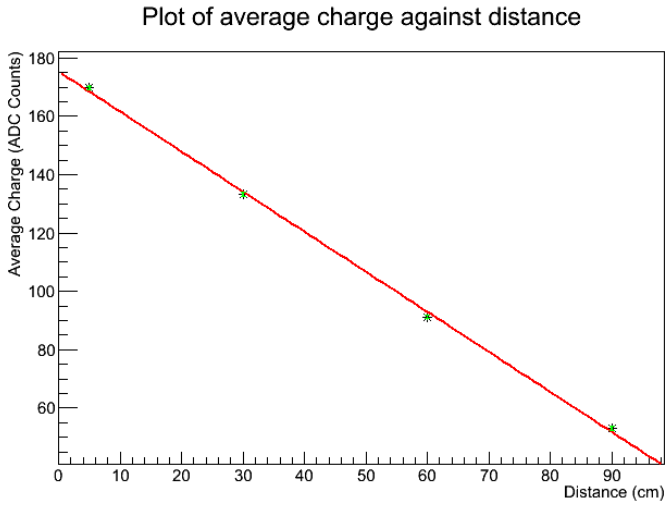

Figure 6.10: Plot of average charge against position recorded in the WLS fibre alone with the LED.

that the light being projected into the tube is not being captured fully by the fibre but is being transported to the PMT in the gap that is left. Although this plot cannot be considered to be wholly representative of the behaviour of the WLS fibre; it does demonstrate the need for greater control over the light source. This will be achieved using the laser.

Full bar: LED

Figure 6.11 shows the data collected from the complete bar.

The purpose of beginning the experiments with the LED was to set up the experiment and ensure the method of data taking works well. What is expected to be seen is a decrease in charge as distance increases. Figure 6.11 suggests that this relationship is exponential. The closer the light source is to the PMT the greater the amount of charge there will be. The light from the source may be travelling directly into the PMT as well as being captured by the WLS which may have an effect on the amount of charge recorded. As distance increases one would expect there to be some degradation in the light's strength resulting in a lower recorded charge in the PMT. The 8, 38 and 68 cm points are consistent with an attenuation length of 115 cm. This

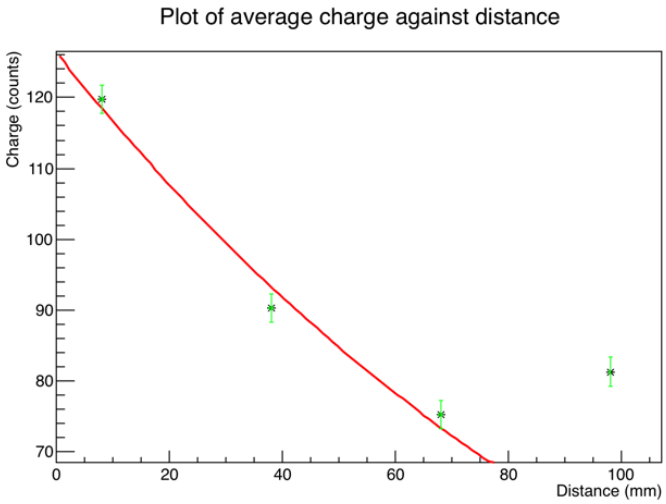

Figure 6.11: Plot of average charge against position recorded in the complete bar.

is comparable to the attenuation length presented in R. Asfandirayov's thesis [42] of just over 1 m.

The total signal is comprised of all of the light within the bar reaching this PMT, this includes; the light travelling directly to the PMT from the excitation point; and the light that has been reflected by the end face of the bar. As the excitation point moves towards the end of the bar a greater proportion of light is reflected. The reflected light leads and light that travels directly to the PMT causes an increase in signal seen by the PMT. This is exhibited in Figure 6.11 which shows a rise near the end of the bar. The rise seen at 98 cm is likely to be due to the combination of direct light and the reflected light at the end of the bar. This reflection effect can be duplicated by assuming a perfect reflecting surface of radius 3.5 mm at this end. This surface is smaller than the end of the bar but is consistent with an imperfect reflection.

For the next experiments greater control over the light source and more hit positions on the bar and fibre will aid in removing any unknown factors.

6.4.4 Laser Experiments

The laser experiments use the same set up as the LED experiments but with a laser to illuminate the fibre or bar. The laser is positioned along the z axis or length of the bar/fibre using the Anorad movement stage. This ensures the x position, across the bar's width, will not be altered between data points. For the x direction measurements the laser was moved using a fixed ruler and the position of the laser's stand was measured by the ruler. Initially the point of light is fixed at the edge of the bar which is at the bar's thinnest point. The z position is fixed for this experiment.

Wavelength Shifting Fibre: Blue Laser

Collecting data relative to position against charge proved difficult for the WLS fibre. This is due to the width of the fibre being small and its sensitivity towards the entry position of light. Like the LED experiments the light entering the fibre must enter at exactly the same point across the width of the fibre at each data point. The fibre had been housed in a metal tube in an attempt to aid this. The fibre is a blue to green light shifter therefore the blue laser was used for this experiment.

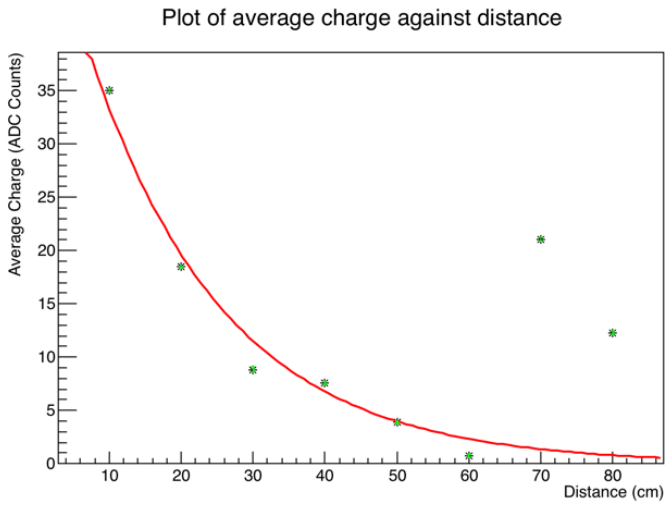

Figure 6.12: Plot of average charge against position along fibre length.

Figure 6.12 shows the results of the experiment. The plot suggests that there is a decline in charge collected by the PMT as distance increases. The LED experiments have fewer data points along the length so it was difficult to see a definite relationship between charge and position. One would expect that charge would decrease exponentially and Figure 6.12 seems to suggest this is the case. The last two data points, 70 cm and 80 cm, do not follow the trend; this could be due to the position of the laser with respect to the fibre's width. It was observed whilst conducting the experiment that very slight movements in the z direction would alter the signal seen significantly.

A possible way to overcome this would be to use a diffusion mechanism to disperse the laser's light over an area that covers the entire fibre's width. This may help with the sensitivity to position. This was not done however, because the detector will not be using the fibres on their own but as part of the full bar. Therefore the bar's experiment will be more important to understanding he relationship between position and charge.

Full Bar: White Laser

The construction of the bar means that the WLS fibre is house in a transparent scintillating plastic. This plastic, in turn, is coated in an opaque white plastic that provides protection as well as stopping the light generated in the scintillator from escaping. A white laser was used in order to be captured in the scintillating plastic and then the WLS fibre. In order to maximise the light entering the bar 1 cm strips of the protective outer coating were removed from the base of the bar. These strips are aligned across the width of the bar and are at 10 cm intervals along the bar's length. This meant the protective outer coating did not affect light entering the bar. It does mean, however, that light may escape from these strips. Due to this being a constant between all the data points this should not affect the results. Although the mechanism for producing scintillation light with a laser beam is different from a charged particle, still the light is produced the same. For this experiment the white laser was used as the source to enable maximum light to be captured by the plastic.

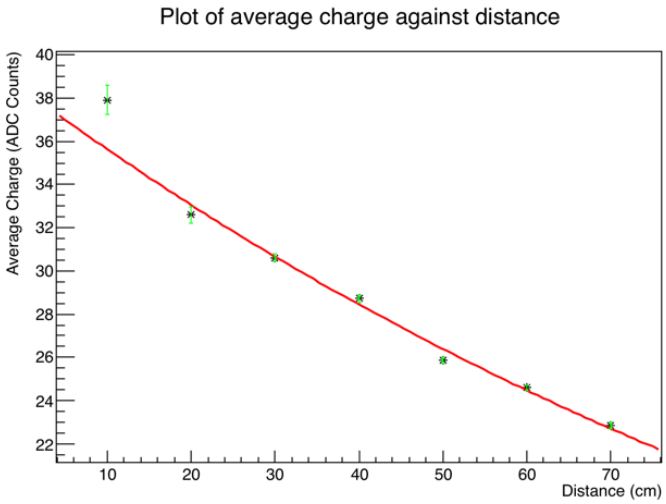

Figure 6.13: Plot of average charge against position along bars length.

Figure 6.13 shows that there is a decrease of charge with distance from the PMT. Close to the PMT at the 10 cm data point shows an increase in charge. This increase could be an effect seen by light captured in the bar and not the fibre travelling directly into the PMT. Light this close to the PMT will also not be shifted as it has not had the distance in order to shift along the WLS fibre.

Like that seen in the WLS experiment very slight variations of z position of the laser can result in a higher or lower charge yield. This is not so pronounced as that seen in the WLS fibre but is still present. In order to improve the experiment the laser could be passed through an optical sphere that would illuminate the section of the bar that has the protective coating removed. This would mean that uniform light illuminates this section and should normalise the amount of light entering the bar at each point. This set up would also improve the results with the WLS fibre only experiment.

The second experiment conducted with the bar was to place the laser at the edge of the bar and scan across its width. The edge of the bar is it's thinnest point, the data point will traverse the bar through its thickest point in its center to the other end of the bar's width. It is expected that the charge should decline towards the edges where the material has less thickness. The

thicker areas of the bar allows more light to be captured and therefore should yield greater charge in the ADC board.

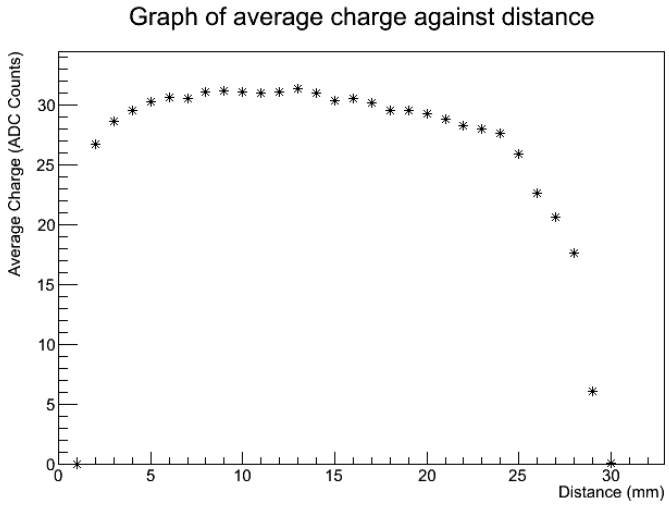

Figure 6.14: Plot of average charge against position across the width.

Figure 6.14 is the plot of the charge over the width of the bar. As expected the charge decreases as it nears either edge of the bar. It should be noted that the bar is approx 33 mm in width where around 1 mm of the thickness is the protective coating. The data was taken by placing the laser at the edge of the bar so the laser is illuminating the scintillating plastic rather than the protective coating. The data was taken over a 30 mm length to reduce effects that may occur from the protective coating. The is a slight drop in charge as the laser passes over the center point of the bar, after 15 mm, in comparison to the first half. One would expect this to be more symmetric due to the bar's cross section shape. The fibre within the bar does not totally fill the hole in which it resides and there is also glue that fills the gap and holds it in place. There is no guarantee that the fibre is exactly in the center and could be closer to one side than the other. This could be the reason for the slight drop, further investigation will be needed if this effect is deemed to be detrimental to the overall experiment.

Figure 6.14 shows that charge decreases only in a region of a few millimetres from either edge of the bar with uniform response from the rest of

the bar. This is to be expected because the amount of material the laser interacts with is considerably less than towards the center. The bars in a plane are built in a tessellated fashion meaning the edge on a bar will align with the center of the next bar in the plane. This indicates that there will be good efficiency across the whole plane.

6.4.5 Radioactive Source Experiments

The last of the planned experiments was to conduct the same charge investigation replacing the LED and Laser sources with a radioactive isotope. The β source was held in a lead lined container with a collimator to ensure the interaction is well localised in the bar. The source was initially placed close to one of the PMTs and was then moved incrementally along the bar's length. Figure 6.15 plots the output of one of the PMTs only. A PMT was placed at both ends of the bar with a view to using coincidences to eliminate dark noise. Due to time constraints the analysis to remove the dark noise has not been undertaken. The resultant plots are compared to what has been seen with the LED and laser experiments.

Using the radioactive source to excite the bar induces true scintillation which is closer to the situation in MICE. The uncertainties associated with these experiments have been determined in the same manner as those that used the LED and lasers to excite the bar.

Figure 6.15 shows the recorded charge for each position along the bar. The 40 cm point has been discarded as an anomaly. In this case the source started at the end of the bar furthest away from the PMT whose output is being plotted. For charged particles the light collection is uniform along the bar. This plot includes the dark noise seen by the PMT. Dark noise is caused by the thermionic emission from the photo cathode. Background noise from cosmic rays are also included within this plot. Cosmic ray rates are too small to cause a problem. Noise can be rejected by looking for coincidences between the two PMTs at either end of the bar. The noise affects every point on the bar and since the bar's response is reasonably uniform it will effect every point equally.

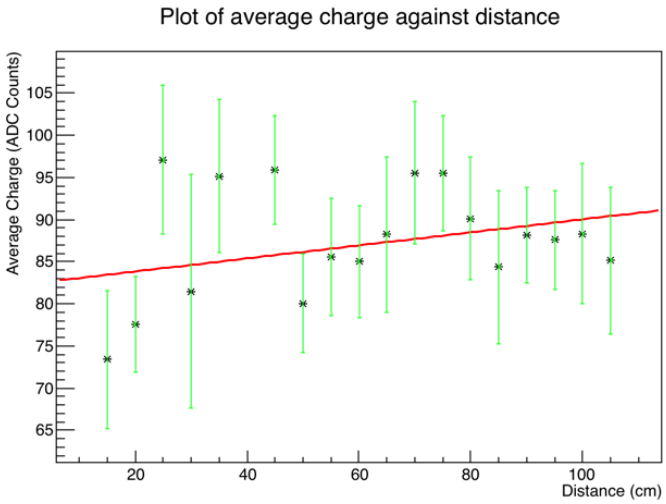

Figure 6.15: Plot of average charge against position along bar's length.

The difference between the amount of charge collected via the source and the other methods that have been described is considerable. Charged particles produce a much larger amount of light. The data shows much more fluctuation than that seen with the laser. Photons from lasers deposit fixed amounts of energy whereas energy deposition from charged particles can vary from event to event.

Figure 6.16 shows the charge collected as the source is moved across the width of the bar. For this experiment a micrometer was adapted to move the source across the width of the bar with high precision. The source was initially placed at the edge of the bar and moved in 1 mm increments across the bar. This plot shows uniform response across the bar. It should also be noted that the first and last two mm of the bar have no data, this is because these positions contain only the protective plastic coating. Figure 6.14 depicts the results taken with a laser across the bar's width. Combining the results measured using a charged particle across the bar's length and width demonstrates the bar produces the same response almost independent of position. This implies the digitisation model, for the EMR, used within MAUS is just a suitable constant, and no position dependant corrections are needed during analysis of EMR data.

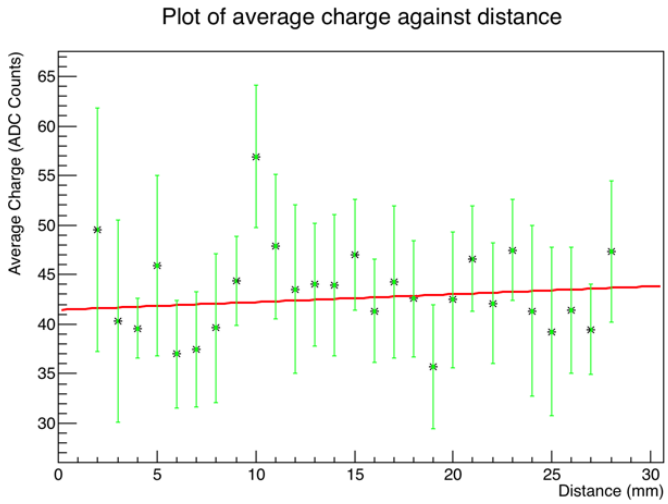

Figure 6.16: Plot of average charge against position across the bar's width.

6.5 Response Time Experiments

A number of different methods were used to excite the bar and a WLS fibre on its own. Firstly, an LED was used to excite a complete bar and a WLS fibre on its own. The LED was then replaced with a laser where a blue laser was used to excite the WLS fibre and a white laser to excite the scintillating bar. When the PMT recorded a signal the PicoHarp then stopped the timer, recording the time it took for light to enter the bar and travel to the PMT. The LED's position along the bar was moved incrementally away from the PMT and the results used to determine the bar's response time.

6.5.1 Uncertainties

The uncertainties used for the timing experiments used the same measurement techniques for the distance of the interaction point along the bar as that used in the charge experiments. Therefore the same value for these uncertainties will be used.

The PicoHarp records the time taken for a signal to be seen in the PMT after the the source has illuminated the bar or fibre. A number of sample times are recorded per position and the average is displayed. The associated

error is $\frac{RMS}{\sqrt{N}}$.

6.5.2 LED Experiments

The LED is initially placed at a distance of 8 cm from the PMT. An 8 cm distance is chosen because at this position there is enough space to push the LED and its casing flush with the underside of the bar. The shoulders and shelf that support the bar are between this position and the PMT, therefore the LED cannot be located any closer. The furthest position of the LED is at 98 cm from the PMT. This was chosen because it is 90 cm from the initial location. The LED is driven via a waveform generator that produces two signals, one signal drives the LED and the other serves as a trigger for the timing device. The trigger acts as the start signal for the timing device and the stop time signal is provided by the PMT when it records light. This means that the time for the light to travel through the bar to the PMT is measured. Data is taken over a ten second period for each position.

One can calculate the time light will take to travel a 90 cm distance through plastic. The base medium of the scintillating bar is Polystyrene and the refractive index for this is 1.59. This value was taken from the Particle Data Group [18]. The WLS fibre BCF-92 produced by Saint-Gobain Crystals is also provided with a refractive index of 1.6 as the core material for the fibre is also Polystyrene. If it is assumed that the combined refractive index for the composite bar is 1.6 then the speed of light in the bar can be determined. Completing the calculation, $v = c/n$, yields a speed of $1.875 \times 10^8 ms^{-1}$. Both the WLS and the bar are polystyrene so it is safe to assume this is the velocity through all the media. However, the diameter of the hole where the WLS is housed is larger than the diameter of the WLS. The remaining volume is filled with glue; this volume can be considered a very thin slice of glue due to the space that has been allowed for it. Considering the area occupied by the glue being less than a mm it can be considered to have a negligible effect. Using this information the time to travel 90 cm along the bar can be determined. This calculation yields a time of 4.8 ns.

Figure 6.17 displays the mean recorded time for each position along the

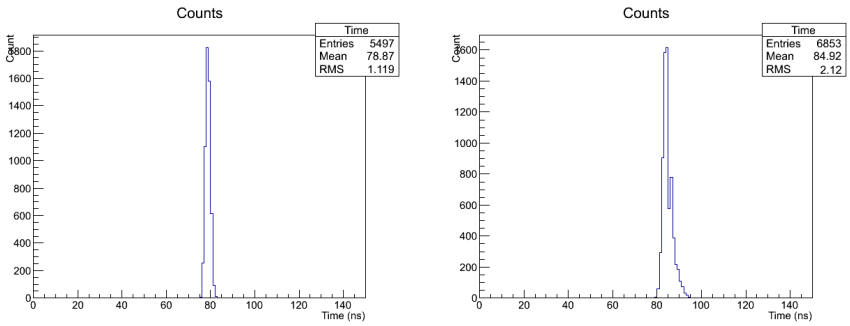

Figure 6.17: Left: Time Response at 8 cm. Right: Time Response at 98 cm.

bar. The response time seen at the 98 cm position has a greater width than at 8 cm. At 98 cm the light can take multiple paths before reaching the detector causing the spread in the width.

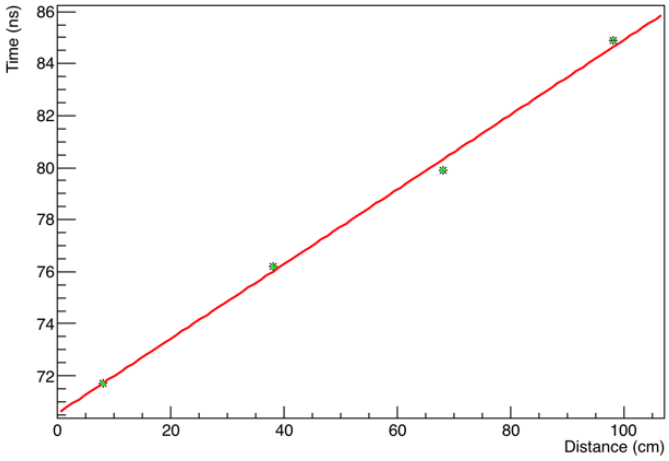

Figure 6.18: Plot of average response time against position.

Figure 6.18 shows the data produced using the LED and the fibre. The recorded timings are well correlated and this shows that the bar is working well in transporting the light to the PMT. The fibre was designed to shift blue light to green; using a blue LED allows the light to be shifted easily because it is captured well by the fibre due to its design; this gives good results in terms of recorded times.

6.5.3 Laser Experiments

The laser experiments use the same set up as that of the LED experiments. Two different lasers were used. One laser, which emits blue light, is used to illuminate the wavelength shifting fibre. As the WLS has been manufactured to shift blue light to green this was perfect for achieving accurate results. The second laser emitted white light and is used to illuminate the full EMR bar. This does not cause true scintillation but gives a good level of control over the position where the light enters the bar. The light is then captured by the bar and makes its way into the WLS fibre to be transported to the PMT. By conducting the experiments in this fashion the effects of the WLS can be isolated and can be compared to the performance of the overall bar.

Sanity Check

Before the experiments were conducted a sanity check was carried out. This experiment directed the laser directly into the PMT and moved the PMT in 10 cm intervals similar to the WLS and full bar experiment. This provided data in order to calculate a time for the light to travel through air. Figure 6.19 shows the data taken from the sanity check.

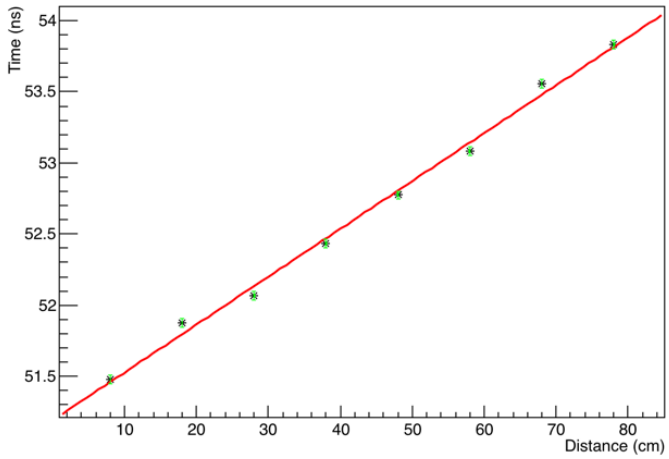

Figure 6.19: Plot of average response time against position in air.

To find a value of the time it has taken for the light to travel an expanse

of 10 cm the difference between each data point is averaged. Light travels at $3 \times 10^8 ms^{-1}$ which means the data recorded should yield an average of 0.3 ns for 10 cm. This is what is seen in the data, secondly it is expected that light should take 2.33 ns to travel across a 70 cm distance. If the time recorded at the 78 cm position has the 8 cm recorded time subtracted; the recorded travelling time yield is 2.35 ns. The recorded time to traverse the 70 cm gap differs from the calculated time by 0.02 ns. This experiment can also be used to calculate a value for the speed of light. The values for distance at the times 51.5 ns and 53.8 ns are 8 cm and 78 cm respectively. The means that light has taken 2.3 ns to travel across the 70 cm and this yields a speed of 3.04×10^8 ms. The speed of light is 2.99×10^8 ms. Both calculated and recorded results are close and this does not raise concerns as to the performance of the equipment.

Wavelength Shifting Fibre: Blue Laser

The blue laser was pulsed at 5 kHz at an intensity that was captured by the WLS fibre. The initial position of the laser was 10 cm from the PMT. It was then moved in 10 cm intervals along the WLS fibre. The time was recorded for each position and the results can be seen in Figure 6.20.

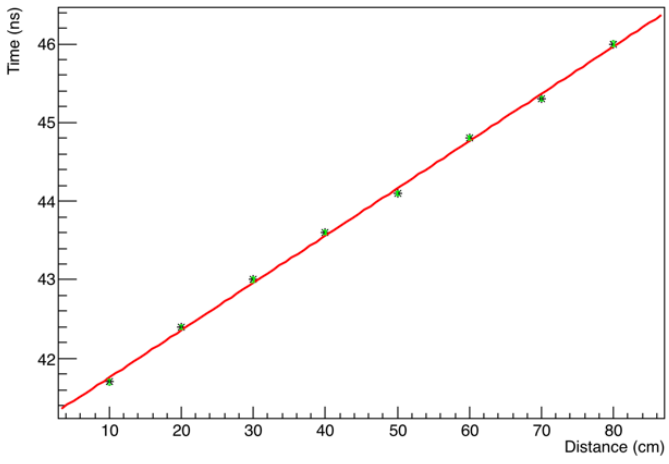

Figure 6.20: Plot of average response time against position along WLS.

Figure 6.20 shows a strong correlation of the data points. The average time it takes the light to traverse the 10 cm gap taken from the difference between each data point is 0.6 ns. By subtracting the time recorded at the 10 cm position from that recorded at 80 cm provides the time to travel 70 cm. This calculation eliminates the time it takes for the electrical signals to travel along the cabling. This gives a 4.3 ns difference and represents the time taken to travel 70 cm along the WLS fibre. We can repeat the calculations for 70 cm to determine the theoretical travelling time. This calculation yields a value of 3.7 ns for a distance of 70 cm. This value represents the time it would take for the light to travel directly along the fibre in a straight line. In practice this is not the case. The light enters the fibre at right angles. The laser will create isotropic scintillating light along its path. If light meets the fibre with anything less than the critical angle it will escape. Light within the fibre that is travelling along a path that has an angle that is greater than the critical angle will be internally reflected. It will move along the fibre via these reflections.

Figure 6.21: Diagram illustrating the bouncing of light within the WLS fibre.

The extra distance travelled by the light bounce within the fibre can be calculated. The red line in Figure 6.21 shows the path of light as it travels along the length of the bar. The angle 'a' is the angle of total internal reflection; this is 68.6° [55]. The internal angle is therefore 21.4°. Length B and C can then be calculated. These are 0.00255 cm and 0.00274 cm respectively where 0.0025 cm is the length travelled by light which is travelling in a straight line and 0.00274 cm is the distance travelled by light which is bouncing between the edges of the fibre. The total length of the distance of interest, 70 cm, if this is divided by Length B the total number of bounces

can be calculated. If this is then multiplied by Length C the total length of distanced travelled by the bouncing light can be determined. This distance is 75.76 cm, repeating the calculation for the time it takes light to travel this distance within the WLS fibre gives a new value of 4.1 ns. The time recorded across 70 cm is 4.3 ns; this value is closer to the new theoretical calculation that includes the extended distance that accounts for the light bouncing within the fibre. The fibre does include cladding that protects the fibre, this has been included within the thickness.

Full Bar: White Laser

As with the WLS experiment a white laser is pulsed at 5 kHz at an intensity that the bar could capture, that produced a reasonable pulse within the PMT. The laser is initially placed in a position of 10 cm from the PMT and then moved in 10 cm intervals away from the PMT. Unlike the experiments that were carried out on the WLS fibre the bar will have its characteristics investigated in two ways. Firstly, as described, the laser is moved along the length of the bar and data points will be taken every 10 cm. This will investigate the effects the hit will have along the length of the bar. The second experiment will investigate the effect of a hit crossing the bar at different points across its width. For the width experiment the laser begins in a position that is at the very edge of the bar. This position is at the thinnest point of the triangular cross-section of the bar. The laser is then moved a millimetre at a time across the bar's width until a millimetre after the center point, this is where the bar is thickest.

Figure 6.22 shows the response of the full bar, this shows that the time increases with distance. The fibre saw that the average time for light to travel along a 10 cm distance within it was 0.6 ns, the full bar delays this travel by a fraction. Light travels along a 10 cm distance within the bar at an average of 0.7 ns. The full bar contains extra materials for the light to travel through, firstly there is a layer of glue around the fibre and the fibre itself for the light to traverse. These could increase the time it takes for the light to be captured by the fibre.

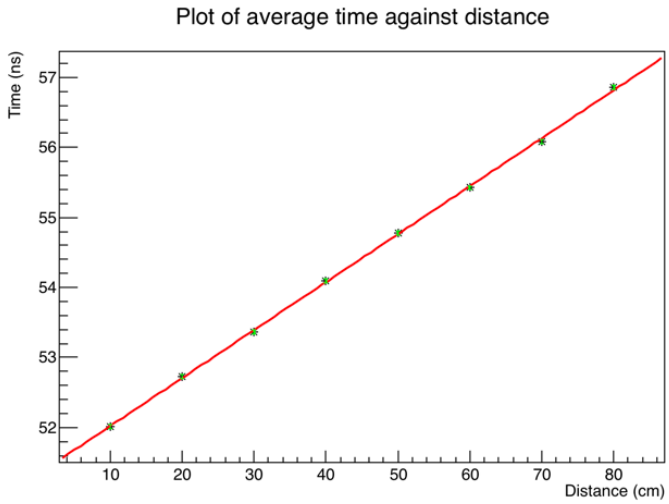

Figure 6.22: Average time against position along bars length.

During this experiment the Full Width Half Maximum (FWHM) values for each of the timing peaks is recorded. This value gives an indication of the spread of recorded times for each peak. A smaller FWHM value shows that the different recorded times that make up the peak fall within a small time window. A larger value will indicate that the times are more diverse. Plotting the FWHM values will show how each data point varies with distance, this can be seen in Figure 6.23.

The FWHM plot shows a general trend of increasing peak timing spread with distance. This is expected, the most direct path to the detector represents the minimum distance for the light to travel. Not all light at the source will take this path but may take longer paths to the detector. The light that takes a longer path to the detector will take slightly more time than light taking a direct path. As distance increases the light has more distance to travel on the various paths to the PMT and so the time variation is more pronounced. The light travelling along the path with the greater distance will be more attenuated. As the distance from the light source to the PMT increases, the loss of light from the longer path becomes more pronounced and the high time tail will decrease. This will reduce the RMS but for the distances seen here the time tail seen by light travelling along greater paths

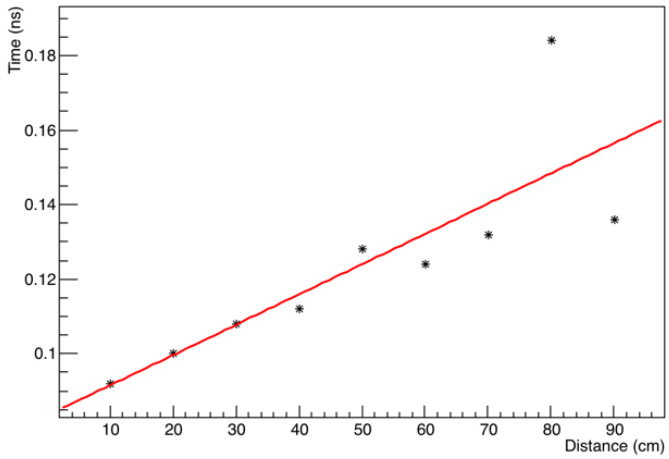

Figure 6.23: Full width half maximum values against position along bars length.

is still captured increasing the RMS in this case.

The second experiment records the effect traversing the light across the bar's width has upon the timing.

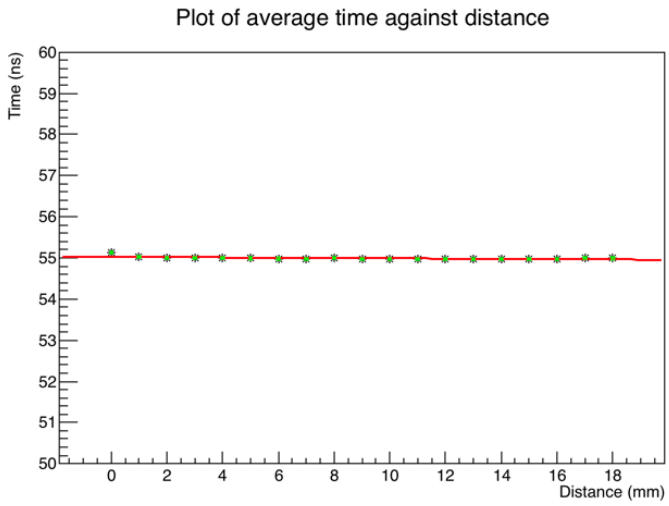

Figure 6.24: Average time against position across the bar. This experiment was across half the width of the bar, the full width of the bar is 32 mm.

This experiment began by placing the laser at one edge of the bar and

moving it a millimetre at a time until just after the center point of the bar. Figure 6.24 shows the results of this experiment. It is apparent that the time for light to travel to the PMT decreases as the laser moves towards the center of the bar. This is due to the placement of the fibre within the bar. The fibre is housed in the center of the bar and is the main form of transport for the light. Light captured at the bar's extremities has a greater distance to travel before it is captured by the WLS fibre and therefore takes a greater time to do so.

6.6 Systematic Tests

Repeatability of the experiments conducted is important to ensure that the results are not affected by variations in the environment of the test bed. The following tests were carried out to understand if there are any effects.

6.6.1 Prolonged Running

The first test involves running the experiment in a controlled manner for a prolonged period of time. This is to check that the system is stable and that environmental effects do not alter the results. The concern that was raised was due to the location of the experiment. The dark box, in which the experiment sits, is located in small clean room within a larger room with large windows. It is known that the temperature within the clean room can become high during the day. The test aims to investigate whether this has an effect upon the equipment. The experiment uses an LED that was surrounded by a light tight cover, Figure 6.25, pressed against the bar of one of the scintillators.

The LED is driven at a frequency of 1 kHz. The voltage is to 3.3 V where the baseline is at 0 V and the signal peaks at -3.3 V. The voltage is set this value because it is the lowest voltage needed to light up the scintillator and thus see a signal in the PMT. The LED is driven by a wave form generator and the sync output signal is used as the external trigger for the fADC. The PMT is plugged into Channel 0 and it was configured accordingly. Testing

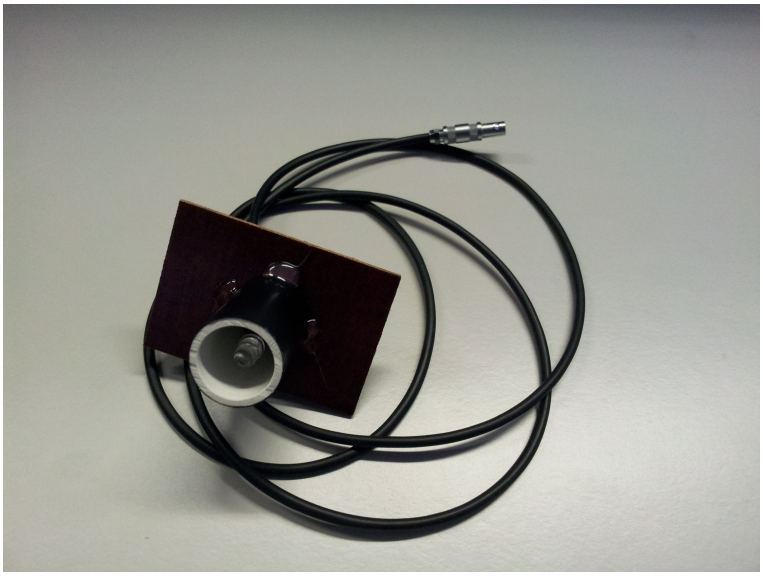

Figure 6.25: LED with light tight cover.

lasted for 5555 runs which equates to roughly 18.5 hours of data taking where the equipment continued to record data. The prolonged test proved that the system is stable for extended periods which are much longer than required to take detailed results.

6.6.2 System Restart Test

Another potential source of uncertainty is the effect of a system restart. A known source of errors is the calibration of the DC offset voltage, if the fADC board is restarted a new calibration is needed because the offset value will have changed. For this test the entire system is shut down for 48 hours then restarted. A calibration test and data run were carried out after the system restart. The set up used for the prolonged test was used for this test to ensure consistency.

Figure 6.26 shows that the calibration reduced the pedestal noise down to a minimum. The waveform of the signal taken from the data run can be seen in Figure 6.27 and when compared with 6.5 one can see that there is very little difference in the shape of the curves of the signals. Although there

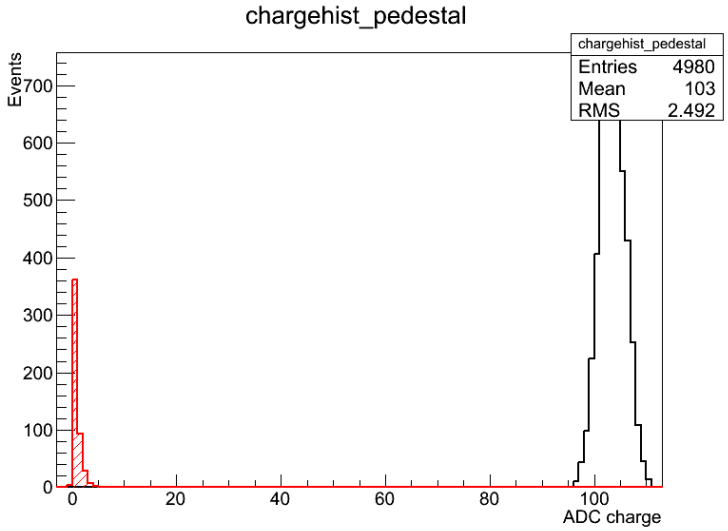

Figure 6.26: Charge histogram for the system restart test.

is a difference in the baseline, acquisition window and amplitude these are not to be compared as these will vary from experiment to experiment. What is under comparison is the shape of the signal curve itself. A smooth curve of constant shape is required because this is what the integration window will cover for analysis. There is an effect on the tail of Figure 6.27 but the reason for this is unknown, the integration window selected for analysis will include as little of the tail fluctuations as possible. As with the previous experiment this test investigates whether the equipment could have an effect upon the data being plotted. In both cases the shapes of the signal curves and the calibration demonstrates reproducibility after a restart.

The tests that were carried out show that outside variables such as temperature and restarting the equipment did not have an effect on data quality. Calibration of the board, however, does need to be done every time it is restarted as the internal current changes.

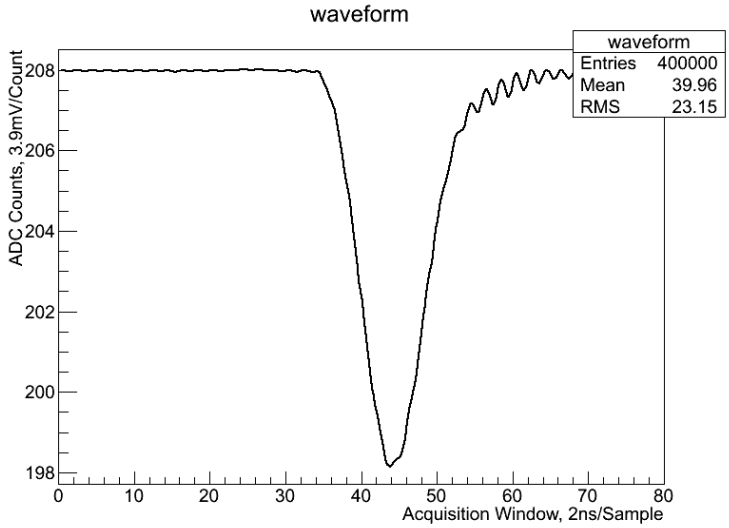

Figure 6.27: Signal waveform for the system restart test.

6.7 Plane Efficiency Experiments

The detector is designed to identify each particle by capturing the light produced in the scintillating bars. It is therefore paramount that the detector planes capture as much light as possible. In order to determine the best operational set up for each detector plane, measurements were made on two different PMTs for a range of different voltages. The PMT that provides better results for the various voltages can be selected for data taking.

Each PMT is connected to a single plane in turn; a run of roughly 5000 cosmic events are then taken. This is repeated for five different voltages to determine the optimum voltage for the PMT. Two small scintillators are located, above and below the plane, in line with one another. A cosmic ray that goes through these scintillators at the same time triggers the data taking. Figure 6.28 illustrates the experimental set up. The entire set up is positioned in a dark box made of thick black material.

When a data recording is triggered the fADC board digitises the signal it receives from the PMT. In this instance every scintillating bar is connected to the PMT. The signal seen in the PMT represents the total light produced in the plane at the time of interaction. The average raw signal that was

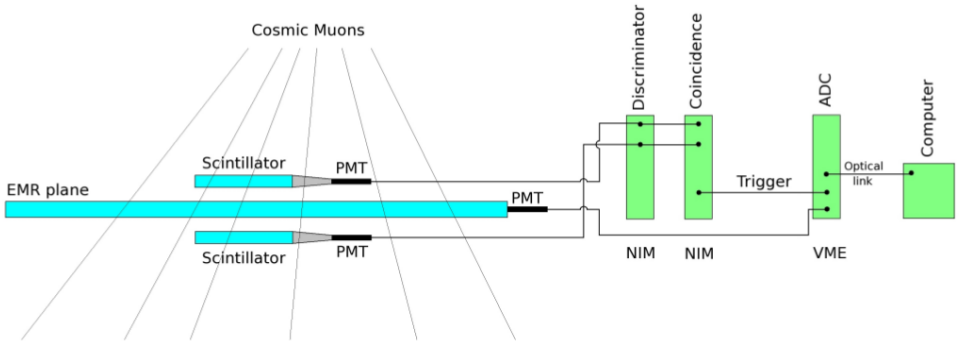

Figure 6.28: Schematic of plane efficiency experiment.

produced by the interaction can be seen in Figure 6.29.

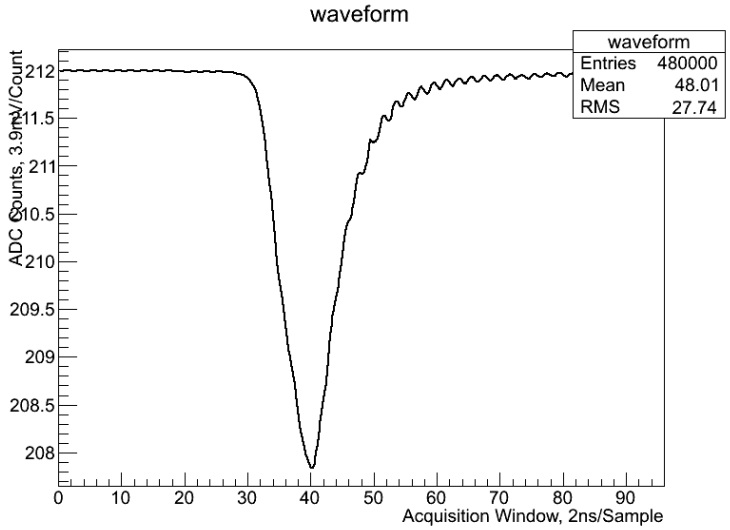

Figure 6.29: Accumulated waveform of signal taken by the Hamamatsu PMT at 1500 volts.

This signal is then integrated over the two windows to determine the charge pedestal and the charge of the signal. The result of this integration can be seen in Figure 6.30 where the red curve is the pedestal signal and the black the cosmic event signal.

The average charge for this voltage can now be used and compared with

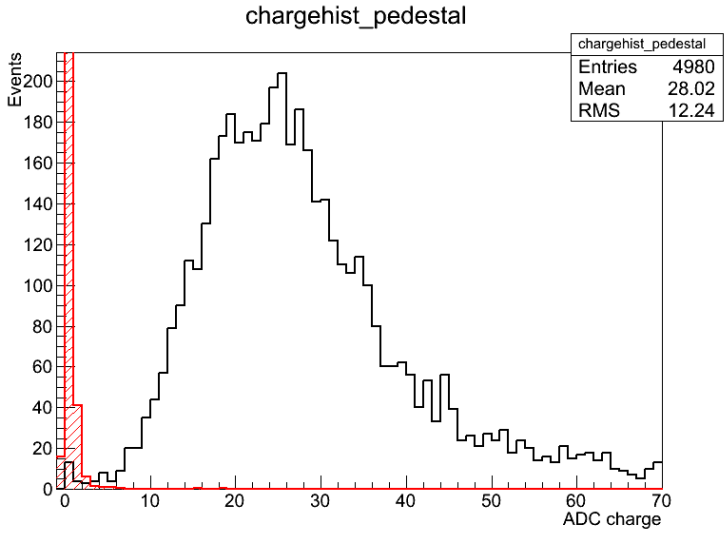

Figure 6.30: Charge histogram of signal taken by the Hamamatsu PMT at 1500 volts.

the same voltage data of the Philips PMT. If these average charges are plotted against one another a comparison between the performance of each PMT can be seen.

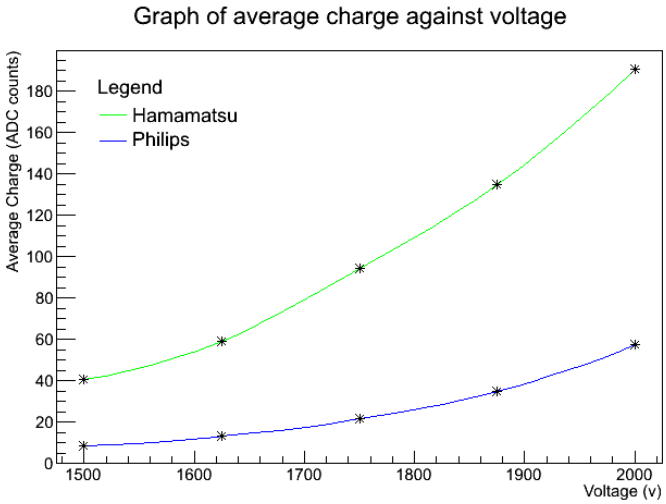

Figure 6.31: Average charge at each voltage for each PMT.

Figure 6.31 shows the average charge recorded at each voltage for each of the two PMTs under examination. It is clear that the Hamamatsu produces more charge than the Philips. This, however does not indicate a greater efficiency than the Philips. This means that for each interaction more charge is recorded but there may also be a higher pedestal charge as well. To calculate the efficiency the integrated charge from the point where the pedestal charge crosses the signal charge to infinity is divided by the integrated charge of the entire signal. Equation 6.1 shows this calculation where; E is the efficiency and Q is the charge.

$$E = \frac{\int_x^\infty Q}{\int_0^\infty Q} \tag{6.1}$$

If the first 10 ADC counts are rejected as noise from the pedestal. The charge integration will then begin at 10 counts, after the pedestal/signal intersection, the efficiency for each voltage and PMT can be calculated and compared.

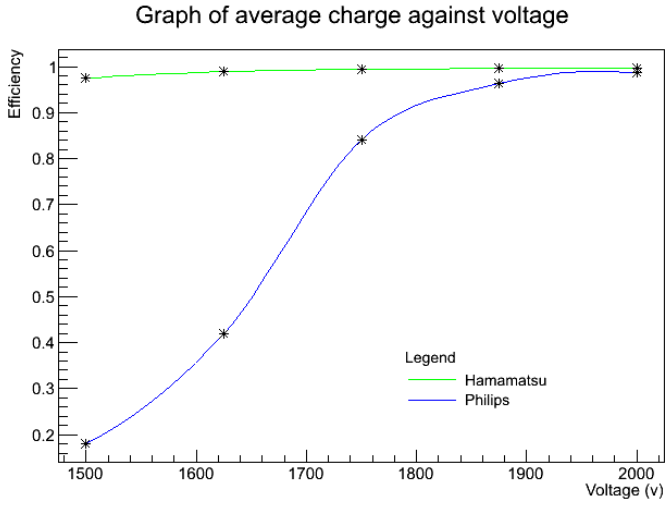

Figure 6.32: Plane efficiency for each voltage and PMT.

It can be seen from Figure 6.32 that the Hamamatsu PMT delivers the best efficiencies for the entire range of voltages. This suggests that this PMT

would be better suited for use as the plane's PMT to be used with the EMR. This will ensure that the maximum amount of light is seen in the detecting equipment which will improve data quality.

6.8 Conclusion

The investigations in this chapter sought to determine a relationship between the position of a hit upon the bar and the amount of light that this hit generated. The charge across the bar's width was seen to be flat with a drop off towards the edges. The edge of the bar will overlap with a neighbouring bar and thus the efficiency of each plane will be high. The aim is to be certain of when an interaction with the bar has occurred. The results support that an interaction at any position along the width will be recorded.

When light is injected directly into the fibre an exponential fall of light collected at the PMT is seen. The exponential fall off is less steep when the light is injected into the complete assembled bar, consisting of the bar and fibre. When charged particles are used to excite the bar the light collected depends little on the position of the hit. The uniform response of the bar to the position of the hit means that the digitisation code for the EMR can be made using a suitable constant with no position dependant corrections.

The measurements taken during this study show that the bar behaves in a manner that is as expected. A plane's response is uniform and no position dependant analysis is needed.

Chapter 7

Conclusion

The neutrino factory is currently being designed to produce a controlled beam of neutrinos. It will allow the production of a beam of greater intensity and purity than any other source. In order to build the neutrino factory a number of technologies must be developed and refined to suit the requirements of the NF. Ionisation Cooling is a major feature of the NF and as of yet the engineering feasibility of the concept has not been demonstrated. MICE aims to build a single cooling channel section that will cool a beam by 10%. The neutrinos will be created through the decay of pions into muons and then muons into neutrinos. Due to the lack of interactions of neutrinos and their neutral charge, cooling the neutrinos directly is impossible. Therefore, cooling must take place before neutrinos are created. Cooling will be carried out upon the muons before they decay into neutrinos. It is after the cooling stage that the muons will be captured and stored in storage rings where they will be allowed to decay and directed towards detectors.

To support the studies being carried out by MICE a software package has been developed that is capable of Monte Carlo simulation and real data analysis. This thesis has described how the representation of the physical geometry within the software package has been updated through importing CAD models. The models are versioned and controlled by the software group. This system decouples the users from the developers allowing greater control and flexibility over the geometry. The use of CAD models means that the

geometry can be changed rapidly and accurately which suits the needs of this ever changing experiment.

MICE has a number of different detectors that have been designed to either identify particles or track them. Particle identification is important to the cooling measurement because it ensures that only muons that have not decayed in the channel are included in the measurement of the cooling efficiency. The Electron Muon Ranger is a PID detector that will act as a beam stop and its purpose is to distinguish between electrons and muons. It does this through a number of layered scintillating bars. The behaviour of the two species within the detector differs allowing them to be identified with ease. Combined with other PID detectors the EMR will allow accurate identification of particles throughout the experiment. In order to simulate the performance of the EMR the efficiency of the bars and light collecting equipment needs to be measured so accurate models of the behaviour can be formed. This thesis studied the light capture of the scintillating bars of the detector and different points along the bars. The experiments used a number of different sources to illuminate the bars and the results can be used to model the bars within MICE's software package.

The work seen in this thesis lays the foundations for future studies. The CAD handling system can be optimised further and studies into the best combination of detail and simulation speed will need to be carried out in order to determine an optimum. The SLitrani simulation will also need to be developed further to incorporate different particles, for this to happen GEANT4 simulations will need to be conducted to determine the energy deposition of muons against distance penetrated within plastic. The energy vs distance information can then be input directly into the SLitrani experiment and the difference between electrons and muons can then be studied. The experiments conducted on the scintillating bars have shown that hits that vary across the width of the bar show negligible differences in terms of light generation. Further studies can be carried out on the experiments that vary the length of the bar, particularly studies that will change the PMTs that are being used to capture the light. The EMR bars have the potential to be a useful technology in a number of engineering areas outside of phys-

ics. A suitable model will enable reliable designs to be developed for these applications.

Bibliography

[1] E. Fermi. Versuch einer theorie der beta-strahlen. *Zeitschrift für Physik*, 88:161–177, 1934.

[2] F. L. Wilson. Fermi's theory of beta decay. *American Journal of Physics*, 36, Number 12:1150–1160, 1968.

[3] Y. Ashie et al. Evidence for an oscillatory signature in atmospheric neutrino oscillation. *Phys. Rev. Lett.*, 93:101801, 2004.

[4] J. Hewett et al. Fundamental physics at the intensity frontier. *arXiv:1205.2671 [hep-ex] ANL-HEP-TR-12-25, SLAC-R-991, FERMILAB-CONF-12-879-PPD.*

[5] F. P. An et al (The Daya Bay Collaboration). Observation of electron-antineutrino disappearance at Daya Bay. *Phys. Rev. Lett.*, 108:171803, 2012.

[6] R. D. McKeown. The Daya Bay reactor neutrino experiment. *American Institute of Physics*, 978-0-7354-0723-7/09, 2009.

[7] C. Cowen. F. Reines. Detection of the free neutrino. *Phys. Rev.*, 90, 492; 92, 830, 1953.

[8] C. Cowen et al. Detection of the free neutrino: a confirmation. *Science*, 124(3212):103–104, 1956.

[9] G. Danby et al. Observation of high-energy neutrino reactions and the existence of two kinds of neutrinos. *Phys. Rev. Lett.*, 9:36–44, 1962.

[10] M. L. Perl et al. Evidence for anomalous lepton production in $e^+ - e^-$ annihilation. *Phys. Rev. Lett.*, 35:1489–1492, 1975.

[11] M. L. Perl. The discovery of the tau lepton. *SLAC-PUB-5937*, 1992.

[12] K. Kodama et al. Observation of tau neutrino interactions. *Physics Letter B*, 504:218, 2000.

[13] Q. R. Ahmad et al. Measurement of the rate of $\nu_e + d \rightarrow p + p + e^-$ interactions produced by ^8B solar nuetrinos at the Sudbury Neutrino Observatory. *Phys. Rev. Lett.*, 84:071301, 2001.

[14] J. Bachall. How many sigmas is the solar neutrino effect. *Phys. Rev.*, C65 (1):015802, 2002.

[15] K. Hirata et al. Observation of a small atmospheric ν_μ/ν_e ratio in kamiokande. *Physics Letters B, Volume 280, Issues 12*, pages 146–152, 1992.

[16] Y. Fukuda et al. Evidence for oscillation of atmospheric neutrinos. *Phys. Rev. Lett. 81*, page 1562, 1998.

[17] N. Jelley et al. The Sudbury Neutrino Observatory. *Annu. Rev. Nucl. Part. Sci.*, 59:431, 2009.

[18] K. A. Olive et al. Review of particle physics. *Chin. Phys. C*, 38:090001, 2014.

[19] S. Sakata Z. Maki, M. Nakagawa. Remarks on the unified model of elementary particles. *Prog. Theor. Phys.*, 28 (5): 870-880., 1962.

[20] Z.Z Xing H. Fritzsch. Lepton mass hierarchy and neutrino oscillations. *Phys. Lett. B.*, 372:265–270, 1996.

[21] The Daya Bay Collaboration. Improved measurement of electron antineutrino disappearance at Daya Bay. *Chin.Phys.*, C37:011001, 2013.

[22] M. S. Zisman. Accelerators for future neutrino facilities: strengths and challenges. *Journal of Physics: Conference Series*, 408:012002, 2013.

[23] M. Benedikt et al. Baseline design for a beta-beam Neutrino facility. *Proceedings of EPAC04*, page 542, 2004.

[24] C. Prior et al. The international design study for a Neutrino Factory. *Proceedings of EPAC08*, page 2773, 2008.

[25] The IDS-NF Collaboration. International design study for the Neutrino Factory: Interim Design Report. *arXiv:1112.2853v1*, 2011.

[26] J. R. J. Bennett et al. Studies of a target system for a 4-MW, 24-GeV proton beam. *Tech. Rep. CERN-INTC-2004-016*, 2004.

[27] I. Efthymiopoulos et al. The merit(ntof-11) high intensity liquid mercury target experiment at the cern ps. *Proceedings of EPAC08*, page 262, 2008.

[28] I. Ambats et al. The MINOS detectors technical design report. *NUMI-L-337, FERMILAB-DESIGN-1998-02*, 1998.

[29] A. Bross et al. Toroidal magnetized iron neutrino detector for a Neutrino Factory. *Phys. Rev. ST Accel. Beams*, 16:081002, 2013.

[30] S. Geer. Muon colliders and neutrino factories. *Annual Review of Nuclear and Particle Science*, 59(1):347–365, 2009.

[31] Fermilab. Mu+mu- collider - a feasibility study. *BNL-52503, Fermi Lab-Conf. 96/092, LBNL*, 1996.

[32] J. B. Rosenzweig. *Fundamentals of Beam Physics*. Oxford University Press, 2003.

[33] J. Marriner. Stochastic cooling overview. *Nucl.Instrum.Meth.*, A532:11–18, 2004.

[34] G. I. Budker. An effective method of damping particle oscillations in proton and anti-proton storage rings. *Soviet Atomic Energy*, 22(5):438–440, 1967.

[35] G. I. Budker and A. N. Skrinskii. An effective method of damping particle oscillations in proton and antiproton storafe rings. *Nuclear Physics Institute, Siberian Division, USSR Academy of Sciences, Novosibirsk Usp. Fiz. Nauk*, 124:562–595, 1978.

[36] The IDS-NF Collaboration. Interim design report. *arXiv:1112.2853v1*, 2011.

[37] MICE Collaboration. The MICE muon beam on ISIS and the beamline instrumentation of the Muon Ionization Cooling Experiment. *arXiv:1203.4089v2*, 2012.

[38] C. N. Booth et al. The design, construction and performance of the MICE target. *JINST*, 8:P03006, 2013.

[39] M. Rayner and M. Bonesini. The MICE PID detector system. In *IPAC '10*, page 1164, 2010.

[40] M. Ellis et al. The design, construction and performance of the MICE scintillating fibre trackers. *Nuclear Instruments and Methods in Physics Research Section A: Accelerators, Spectrometers, Detectors and Associated Equipment*, 659(1):136 – 153, 2011.

[41] A. Blondel R. Asfandiyarov, L. Haegel. Geant4 simulation of the EMR detector response study. *MICE-NOTE-DET-388*, 2012.

[42] R. Asfandiyarov. *Totally Active Scintillator Tracker-Calorimeter for the Muon Ionization Cooling Experiment*. PhD thesis, Université de Genève, 2014.

[43] R. Asfandiyarov. Personal communication, 2012.

[44] S. Q. Yang et al. Progress on the focus coils for the mice channel. *Particle Accelerator Conference Proceedings*, page 3417, 2005.

[45] CERN. GEANT4. `http://geant4.cern.ch/`, Accessed 2012.

[46] The MICE Collaboration. G4MICE. http://www.mice.iit.edu/software/, Accessed 2012.

[47] The MICE Collaboration. MICE Analysis User Software. http://micewww.pp.rl.ac.uk/projects/maus, Accessed 2012.

[48] CERN. Geometry Description Markup Language. http://gdml.web.cern.ch/GDML/, Accessed 2012.

[49] CERN. eXtensible Stylesheet Markup Language. http://www.w3.org/TR/xslt, Accessed 2012.

[50] A. Wilson and The MICE Software Group. Configuration database. http://micewww.pp.rl.ac.uk/projects/configdb, Accessed 2012.

[51] The MICE Software Group. MAUS user guide. http://micewww.pp.rl.ac.uk/maus/MAUS_latest_version/maus_user_guide/index.html, Accessed 2012.

[52] M. Littlefield. MAUS geometry handling system. 2011.

[53] F-X. Gentit. SLitrani photon simulation program. http://gentitfx.fr/SLitrani/, Accessed 2012.

[54] Fluorescence Spectroflourometer. Flourolog -3. http://www.horiba.com/uk/scientific/products/fluorescence-spectroscopy/steady-state/fluorolog/fluorolog-r-our-modular-spectrofluorometer-522/, Accessed 2012.

[55] Saint-Gobain. Saint-Gobain crystals fibre brochure. http://www.crystals.saint-gobain.com/uploadedFiles/SG-Crystals/Documents/SGC%20Fibers%20Brochure.pdf, Accessed 2015.

[56] O. Pierson. Personal communication, Feb 2013.

[57] The MINERvA Collaboration. The MINERvA technical design report. *http://minerva-docdb.fnal.gov/cgi-bin/ListBy?alldocs=1*, Accessed 2006.

[58] The MINOS Callaboration. The magnetized steel and scintillator calorimeters of the MINOS experiment. *Nucl.Instrum.Meth.*, A596:190–228, 2008.

[59] A. Pla-Dalmau and others (MINERνA Collaboration). Extruded plastic scintillator for MINERνA. In *FERMILAB-CONF-05-506-E*, 2005.

[60] S. C. Curran. *Luminescence and the Scintillation Counter.* Butterworths, 1953.

[61] Anorad. Anorad motion deck. `http://www.rockwellautomation.com/anorad/overview.page`, Accessed 2012.

[62] Lego. Lego Mindstorms. `http://shop.lego.com/en-GB/MINDSTORMS-ByTheme?CMP=KAC-GOOGEU\&HQS=lego+mindstorms`, Accessed 2012.

[63] CAEN. Caen v1731. `http://www.caen.it/csite/CaenProd.jsp?parent=11\&idmod=571`, Accessed 2012.

[64] Pico-Quant. Pico harp 300. `http://www.picoquant.com/products/picoharp300/picoharp300.htm`, Accessed 2012.